The Company of Biologists

RESEARCH ARTICLE

Deep learning is widely applicable to phenotyping embryonic development and disease

Thomas Naert[1], Özgün Çiçek[2], Paulina Ogar[1], Max Bürgi[1], Nikko-Ideen Shaidani[3], Michael M. Kaminski[4,5], Yuxiao Xu[6], Kelli Grand[1], Marko Vujanovic[1], Daniel Prata[1], Friedhelm Hildebrandt[7], Thomas Brox[2], Olaf Ronneberger[2,8,9], Fabian F. Voigt[10], Fritjof Helmchen[10], Johannes Loffing[1], Marko E. Horb[3], Helen Rankin Willsey[6] and Soeren S. Lienkamp[1,*]

ABSTRACT

Genome editing simplifies the generation of new animal models for congenital disorders. However, the detailed and unbiased phenotypic assessment of altered embryonic development remains a challenge. Here, we explore how deep learning (U-Net) can automate segmentation tasks in various imaging modalities, and we quantify phenotypes of altered renal, neural and craniofacial development in *Xenopus* embryos in comparison with normal variability. We demonstrate the utility of this approach in embryos with polycystic kidneys (*pkd1* and *pkd2*) and craniofacial dysmorphia (*six1*). We highlight how *in toto* light-sheet microscopy facilitates accurate reconstruction of brain and craniofacial structures within *X. tropicalis* embryos upon *dyrk1a* and *six1* loss of function or treatment with retinoic acid inhibitors. These tools increase the sensitivity and throughput of evaluating developmental malformations caused by chemical or genetic disruption. Furthermore, we provide a library of pre-trained networks and detailed instructions for applying deep learning to the reader's own datasets. We demonstrate the versatility, precision and scalability of deep neural network phenotyping on embryonic disease models. By combining light-sheet microscopy and deep learning, we provide a framework for higher-throughput characterization of embryonic model organisms.

This article has an associated 'The people behind the papers' interview.

[1]Institute of Anatomy, University of Zurich, Zurich 8057, Switzerland; Swiss National Centre of Competence in Research (NCCR) Kidney Control of Homeostasis (Kidney.CH), Zurich 8057, Switzerland. [2]Department of Computer Science, Albert-Ludwigs-University, Freiburg 79100, Germany. [3]National Xenopus Resource and Eugene Bell Center for Regenerative Biology and Tissue Engineering, Marine Biological Laboratory, Woods Hole, MA 02543, USA. [4]Berlin Institute for Medical Systems Biology, Max Delbrück Center for Molecular Medicine in the Helmholtz Association, Berlin 10115, Germany. [5]Department of Nephrology and Medical Intensive Care, Charité Universitätsmedizin Berlin, Berlin 10117, Germany. [6]Department of Psychiatry and Behavioral Sciences, UCSF Weill Institute for Neurosciences, University of California, San Francisco, CA 94158, USA. [7]Department of Pediatrics, Boston Children's Hospital, Harvard Medical School, Boston, MA 02115, USA. [8]BIOSS Centre for Biological Signalling Studies, Albert-Ludwigs-University, Freiburg, Germany. [9]DeepMind, London WC2H 8AG , UK. [10]Laboratory of Neural Circuit Dynamics, Brain Research Institute, University of Zurich, Zurich 8057, Switzerland; Neuroscience Center Zurich, Zurich 8057, Switzerland.

*Author for correspondence (soeren.lienkamp@uzh.ch)

T.N., 0000-0003-3543-2519; M.M.K., 0000-0003-0429-7027; H.R.W., 0000-0001-8404-3291; S.S.L., 0000-0003-2963-6865

INTRODUCTION

Congenital inherited diseases pose a tremendous burden on society (Boyle et al., 2018). Many individuals suffering from genetic disorders are in need of novel therapeutic prospects or could benefit from more accurate genetic diagnoses (Wallingford, 2019). Renewed efforts to uncover the molecular mechanisms that underlie congenital inherited diseases are fueled by the ability to quickly generate and characterize new animal models of human genetic conditions (Naert and Vleminckx, 2018c).

Recent advances, such as CRISPR/Cas9 allow for high-throughput interrogation of gene functions in early embryonic development (Jinek et al., 2012; Nakayama et al., 2013). As a diploid aquatic model organism, *X. tropicalis* can easily be genetically manipulated (Naert et al., 2020b). Devoid of genome duplications, orthologs of human disease genes can be unambiguously identified and phenotypes directly observed in the large number of extra-uterine developing embryos (Hellsten et al., 2010). *Xenopus* is therefore increasingly employed to model congenital diseases and pediatric cancer (Hoff et al., 2013; Lienkamp et al., 2012; Naert et al., 2016, 2020a; Nasr et al., 2019; Szenker-Ravi et al., 2018; Willsey et al., 2020, 2021).

Many congenital diseases are syndromal and affect multiple organ systems. Thus, phenotyping of relevant model organisms needs to take a holistic approach that can uncover abnormalities fast and comprehensively. This can be achieved, for example, by advanced state-of-the-art light-sheet microscopy, such as the mesoSPIM initiative (http://mesospim.org/) (Voigt et al., 2019), which allows *in toto* imaging of entire animals (Liu and Keller, 2016). Recent advances in imaging technology make it possible to acquire images at enormous detail, speed and scale. These multidimensional datasets are challenging to interpret and extract quantitative measures from. As such, the bottleneck for higher-throughput modeling of human congenital disease has gradually shifted from the genetic manipulations towards the accurate qualitative descriptions and quantitative assessments of phenotypic consequences.

Simultaneously, deep learning is revolutionizing the computer vision field, fueled by major leaps in hardware (LeCun et al., 2015). This allows for cost-efficient computation of loss function via backpropagation for image recognition tasks (Raina et al., 2009; Rumelhart et al., 1986). In recent years, deep convolutional neural networks (CNNs) have improved to now readily surpass human performance for visual recognition tasks in terms of accuracy and speed (Campanella et al., 2019). Categorization by a human expert can be a potential source of bias, and the scale of manual labor required can become excessive. Thus, automated analysis pipelines can overcome such constraints, and add objectivity, reproducibility

DEVELOPMENT

1

and scalability to biomedical analysis (Villoutreix, 2021). The use of CNNs or deep learning has repeatedly outperformed other machine-learning algorithms for a wide range of tasks (Emmert-Streib et al., 2020). However, misconceptions about technical hurdles, the anticipated amount of training data and applicable datasets impede the wider adoption of CNNs in biomedical analysis. Until recently, training deep-learning networks required field-specific computer science knowledge, but recent efforts have opened up deep learning to wet-lab biologists. Now, training and use of a CNN of the U-Net architecture can be achieved using a Fiji plug-in (Falk et al., 2019) or cloud computing initiatives, such as ZeroCostDL4Mic (von Chamier et al., 2021), which provide graphical user interfaces.

Although deep-learning approaches crucially depend on high-quality training data, the amount of annotated 'ground truth' data required is often heavily overestimated by non-users. In fact, many U-Net implementations feature data augmentation that allows model training with small amounts of training data (Ronneberger et al., 2015). Finally, U-Net CNNs can be trained on a desktop computer with a consumer-grade graphics processing unit (GPU) in a matter of hours. This makes the computational load feasible for most life science labs.

Lately, deep learning is gaining traction in biomedical sciences for both segmentation and classification tasks of large image datasets. Often, it is employed to recognize highly repetitive features, such as individual cells or nuclei in fluorescence microscopy images (Schmidt et al., 2018; Stringer et al., 2021). However, CNNs have also been applied to more complex tasks, such as reconstruction of the entire mouse brain vasculature (Kirst et al., 2020; Todorov et al., 2020), *in vivo* quantification of cancer metastasis and *in toto* reconstruction of intact human organs (Pan et al., 2019; Zhao et al., 2020). In embryology, deep learning has been used for *Drosophila* animal pose estimation, to map synaptic brain connections (Buhmann et al., 2021; Graving et al., 2019; Günel et al., 2019), in *C. elegans* phenotyping (Hakim et al., 2018; Saberi-Bosari et al., 2020) and in analysis of zebrafish beating hearts or vessels (Akerberg et al., 2019; Kugler et al., 2020 preprint; Wen et al., 2021; Zhang et al., 2021), among other applications. Nevertheless, deep learning remains under-used in developmental biology (Villoutreix, 2021). It is likely that deep learning, and artificial intelligence in general, will be transformative to image analysis approaches in developmental biology.

Here, we have used deep learning for automated analysis of a large variety of multidimensional datasets. We trained and deployed over 15 U-Net models to analyze renal (hypoplastic and cystic), craniofacial (branchio-oto-renal syndrome) and neural (autism spectrum disorder) phenotypes in *Xenopus tropicalis*. For example, we generated novel *Xenopus* models for autosomal dominant polycystic kidney disease (ADPKD). We show automated analysis of a range of imaging modalities, including bright-field, fluorescence, focal laser scanning and light-sheet microscopy, which allowed *in toto* phenotyping of genome-edited *X. tropicalis* embryos. We provide detailed information on how to successfully train, validate and deploy neural networks with minimal annotated training data, and showcase both segmentation and classification of complex features in convoluted datasets. Taken together, we show that deep-learning approaches can be harnessed to accelerate and automate accurate quantitative phenotyping of embryonic disease models.

RESULTS
Deep-learning-based analysis and manual annotations agree in identifying renal dysplasia induced by *TBX18* variants
Heterozygous mutations in *TBX18* can cause congenital anomalies of the kidney and urinary tract (CAKUT) (Vivante et al., 2015). To

investigate the functional consequences of *TBX18* variants, we established an overexpression assay in *Xenopus*. Unilateral mRNA injections at the four-cell stage were targeted to the blastomere that gives rise to the prospective embryonic kidney (pronephros), and thus restricted any phenotypic alteration to only one side of the animal (Fig. 1A). After expression of control mRNA (RFP), wild-type *TBX18* and six variants, pronephros morphology was assessed in 521 samples (Fig. 1B,C). This large sample size provided us with the opportunity to cross-validate manual versus automated measurement of pronephric dimensions.

We trained a frequently used CNN (U-Net) to specifically segment the convoluted tubular part of the pronephros (TubuleNet - n_{train}=295 - Intersection Over Union (IOU): 0.78) (Fig. 1D) (Ronneberger et al., 2015). U-Net is a well established semantic segmentation CNN that assigns each pixel of an input image a corresponding class label (Falk et al., 2019). TubuleNet segmentations of the validation dataset (n_{val}=105) were accurate across the phenotypic spectrum, ranging from mildly smaller to severely hypoplastic kidneys (Fig. 1E). Segmentations of unseen images correlated well with expert annotations (n_{test}=521) for dorso-ventral extension (height; r=0.93, P<0.0001), anterior-posterior extension (width; r=0.88, P<0.0001), bounding box area (r=0.88, P<0.0001) and tubule length (r=0.79, P<0.0001) (Fig. 1F). Thus, deep learning was highly effective in segmenting a single, distinct morphological structure, such as a specific part of the pronephric tubule.

Next, we investigated whether TubuleNet segmentations or manual annotations could affect the statistical comparison between different experimental groups. TubuleNet segmentations closely mimicked expert human annotations (Fig. 1G, Fig. S1A-C). First, the mean of the pronephros area size in each injection group correlated well between TubuleNet and ground truths (n=18, r=0.99, P<0.0001) (Fig. S1D). Second, the difference in means between the left uninjected and right injected pronephros for each setup are also correlated (r=0.94, P<0.001) (Fig. S1E). Third, mean rank differences from Dunn's multiple comparisons between right kidney injected with RFP and right kidneys from all other setups correlate between TubuleNet and independent expert annotations (r=0.99, P<0.0001) (Fig. S1F).

For all *TBX18* variants analyzed, comparable statistical conclusions could be drawn based on U-Net segmentations and manual annotations. Specifically, we found that overexpression of wild-type protein strongly interfered with normal nephrogenesis (P<0.001, TubuleNet; P<0.0001, manual annotation). The truncating mutation G337V* and the missense mutation K163E did not interfere with pronephros morphogenesis (P=n.s.). In contrast, expressing the variants G290R, A164T, H524Y and P526S again interfered with renal development. In conclusion, both automated and manual analysis agreed in distinguishing pathological phenotypes after expression of *TBX18* variants identified in CAKUT patients. U-Net-based quantification is thus highly reliable in detecting pronephric hypoplasia and suitable for scalable quantitative analysis.

3D segmentation of light-sheet data facilitated by deep learning
The convoluted nature of the frequently overlapping elements of *Xenopus* pronephric tubules makes it impossible to accurately assess its full tissue volume by wide-field microscopy. To obtain a three dimensional view of the wild-type and pathologically altered *Xenopus* pronephros, we performed light-sheet microscopy on the mesoSPIM platform (Voigt et al., 2019), which is capable of producing volumetric images of cleared whole embryos with near-isotropic resolution within minutes. Anti-Atp1a1 and LE-Lectin
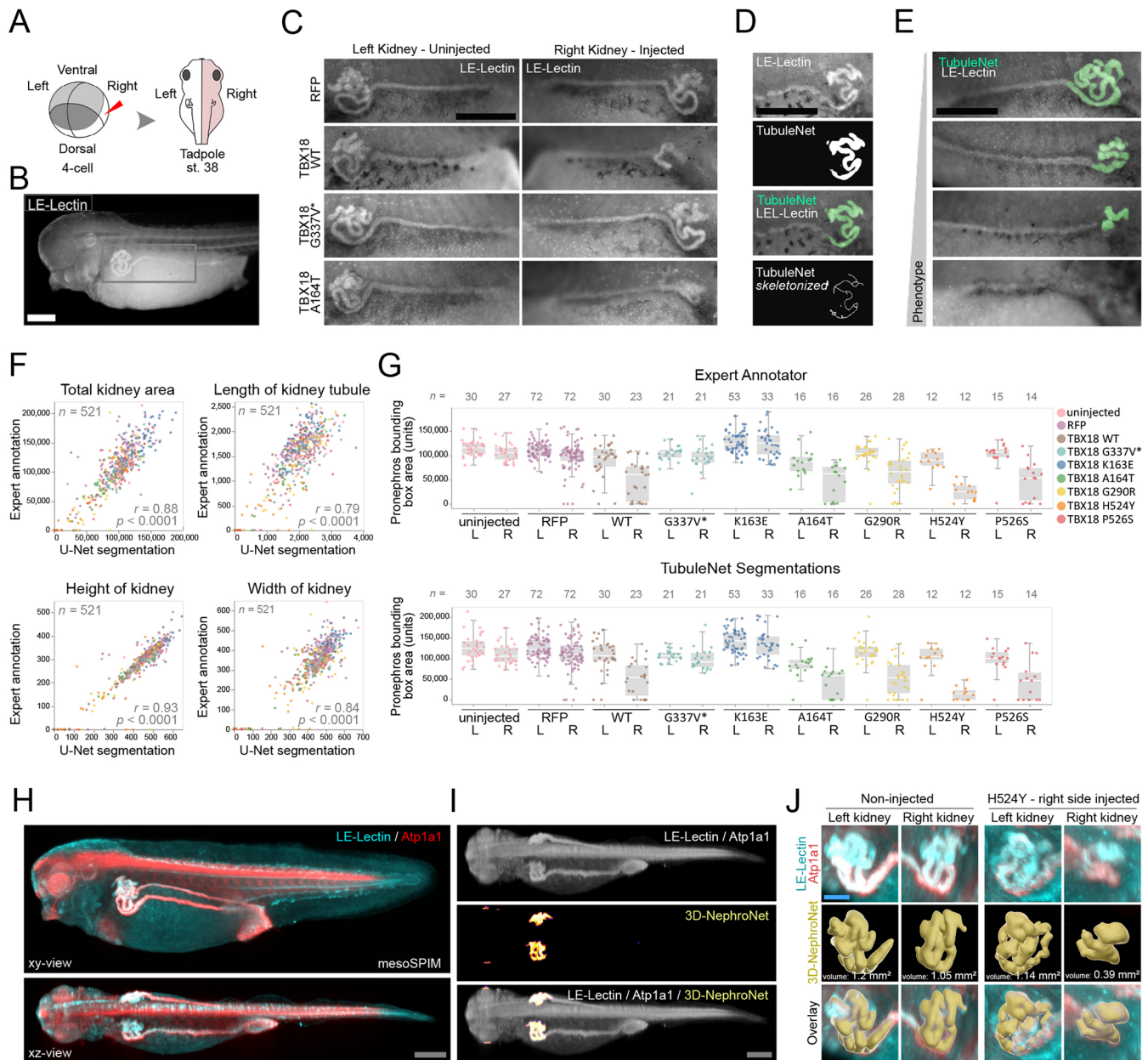
Fig. 1. Deep learning for 2D and 3D phenotyping of altered pronephros development in *Xenopus*. (A) Schematic of unilateral TBX18 expression by injection of mRNA at the four-cell stage in *X. laevis* embryos. Kidney development was assessed on both sides at NF stage 38. (B) Fluorescence microscopy image of an LE-Lectin stained embryo. The gray rectangle indicates the region shown at higher magnification in C. Scale bar: 500 μm. (C) Overexpression of RFP or truncated TBX18 (G337V*) did not affect right-sided kidney morphology when compared with left non-injected side. In contrast, overexpression of TBX18 wild-type and A164T resulted in unilateral kidney hypoplasia. Scale bar: 500 μm. (D) A neural network (TubuleNet) was trained to assess pronephros morphology. Top to bottom: input image of an LE-lectin stained pronephros, the output as a segmentation mask, overlay of input image and mask, and skeletonized mask for feature extraction. Scale bar: 500 μm. (E) TubuleNet accurately segmented renal tubules across a wide phenotypic range (normal, hypoplastic, absent). Scale bar: 500 μm. (F) TubuleNet segmentations closely correlated with expert human annotators on unseen data. *r*, Pearson's correlation coefficient. (G) Plot of pronephros bounding box area per expressed construct shows high agreement between expert annotator and TubuleNet segmentation. L, left (uninjected) side; R, right (injected) side. Boxes and whiskers indicate interquartile range and variability outside the upper and lower quartiles. (H) mesoSPIM light-sheet microscopy *in toto* imaging of a wild-type embryo stained for LE-Lectin (cyan) and Atp1a1 (red). Scale bar: 200 μm. (I) The two channels were merged as input images (top), accurate segmentation by 3D-NephroNet in the volume. Scale bar: 200 μm. (J) 3D segmentation for feature extraction and volumetric measurements. Unilateral expression of TBX18 H524Y resulted in a reduction of 66% in tubule volume on the injected side. Scale bar: 40 μm.

staining allowed us to identify the entire pronephros at optimized signal-to-noise ratios (Fig. 1H).

To segment the convoluted pronephric tubule, we employed deep learning. U-Net architectures that incorporate all spatial dimensions (3D-U-Net; Çiçek et al., 2016) can require pronounced downsampling of data to meet the considerable computational costs.

As we used a consumer GPU, we aimed to avoid the potential loss of resolution, and instead trained, validated and deployed a classical 2D U-Net architecture for segmentation of renal tubular tissue in a light-sheet recording (3D-NephroNet) (Fig. S2A). 3D-NephroNet successfully segmented the pronephros of unseen wild-type and unilaterally H524Y *TBX18* expressing embryos in 3D (Fig. 1I-J,

Fig. S2B). Feature extraction and volumetric measurements showed a 66% decrease in tubular tissue on the *TBX18* H524-injected side when compared with the uninjected side of the same individual. In conclusion, a 'standard' 2D-U-Net successfully segmented pronephric tissue in 3D mesoSPIM data without sacrificing resolution, enabling us to quantify organ volume and detect shape changes in normal and pathological states.

CRISPR knockout of *pkd1* causes cystic tubules in *X. tropicalis* embryos

Autosomal dominant polycystic kidney disease (ADPKD) is caused by mutations in *PKD1* or *PKD2*, and is the most common inherited kidney disorder that leads to end-stage renal disease at a prevalence of ~1:1000 (Bergmann et al., 2018). To model ADPKD in *Xenopus tropicalis*, we performed CRISPR/Cas9 mediated knockout of *pkd1*. We verified efficient gene editing for three distinct guides targeting *pkd1* (*pkd1* gRNA 1-3) by Sanger sequencing and trace deconvolution (Fig. S3A). For all three gRNAs, we independently observed dilated renal tubules or localized kidney cysts, which were absent in wild-type animals (Fig. 2A, Fig. S3B,C). Confocal microscopy was followed by deep-learning-based segmentation of cystic lumen (3D-CystNet), using a sparse annotation approach. Six out of 400 *z*-slices per stack (3%) were annotated to train a model to segment both a wild-type and a *pkd1* crispant ($n_{train}=12$ images) (Fig. S3D). This analysis revealed extensive cystic luminal expansions associated with a thinning of the epithelial lining in *pkd1* crispants, in line with the cystic phenotype in human patients and *Pkd1*-null mice (Fig. 2B) (Gilbert et al., 2013; Lu et al., 1997).

In toto mesoSPIM imaging of *pkd1* crispants was followed by segmentation using the previously trained 3D-NephroNet. This network performed surprisingly well on a wild-type animal, although this embryo was of a different developmental stage than the embryos used for training (Fig. 2C). Owing to the cystic characteristics of the *pkd1* crispant pronephros, a separate network was trained to accurately segment it (Fig. 2C).

The recording of entire specimens at isometric high resolutions, and segmentation of somites and intestine confirmed that no gross malformations were apparent apart from the embryonic kidney phenotype (Fig. S4). Consistent with observations in human polycystic kidneys (Baert, 1978), cystic dilations originated from all segments (proximal, intermediate and distal) of the renal tubule, further strengthening the validity of this novel amphibian model for ADPKD.

Setting up a deep-learning network is robust, requires minimal amounts of training data and can readily be adapted to other environments

Next, we established a new pipeline to automate analysis of both smaller or cystically enlarged kidneys (2D-NephroNet). We injected *pkd1* gRNAs in a ventral-vegetal blastomere of eight-cell *X. tropicalis* embryos using tyrosinase gRNAs as injection controls. For segmentation, we did not rely on TubuleNet, which was specifically trained to detect individual tubules only in wild-type and hypoplastic kidneys, but built a network from scratch and compared a number of training parameters in the process.

Because the stochastic gradient descent loss function optimizer (we used Adam; (Kingma and Ba, 2014) is inherently driven by random fluctuations, we were first interested to see how much the performance would vary in repeatedly trained networks. We noticed that training is very reproducible in technical repeats using identical training data sets and hyperparameters (IOU variance: 0.15, $n=12$) (Fig. S5A,B). We conclude that re-running identical training is

unlikely to result in higher network performance. Second, we evaluated the minimal amount of training data required for a network to perform robustly and found that U-Nets can be accurately trained with as little as five pictures for each condition (normal, cystic and hypoplastic; $n_{train}=15$) (Fig. S5A,B). In fact, models trained for longer with more training data (30,000 iterations, $n_{train}=105$) did not outperform shorter training with less training data (8400 iterations, $n_{train}=15$) (Fig. S5C,D), which we demonstrated by deploying the 2D-NephroNet on unseen data and correlating to ground truths from two independent experts (Fig. S5E).

Third, we tested how easily a pre-trained network could be employed in a different environment. Therefore, we simulated a scenario where a 2D-NephroNet had to be adapted to a different imaging setup. To do so, we performed a data-split. Only images from crispants injected with gRNA 1 were used for training and validating the 2D-NephroNet. To generate an independent image dataset, we used two independent gRNAs (*pkd1* gRNA 2 and *pkd1* gRNA 3) to generate unilateral crispants and acquired images with a stereomicroscope from another manufacturer at a different magnification. Using a transfer learning approach, we fine-tuned the pre-trained 2D-NephroNet on the novel dataset ($n_{train}=30$; $n_{val}=30$). We reached satisfactory accuracy as the initial IOU increased from 0.47 to 0.87 and the F1 (segmentation) score increased from 0.23 to 0.85 within 1000 iterations (computing time was 7 min) (Fig. S6A). This fine-tuned 2D-NephroNet correlated well with an independent expert on test data ($n_{test}=120$; $r=0.96$; $P<0.001$) (Fig. S6B). As such, adapting a pre-trained model to different imaging setups is readily feasible.

Linking segmentation and classification networks to quantify cystogenesis

We deployed this fine-tuned 2D-NephroNet for automated and unbiased quantification of pronephric size. However, we failed to detect a significant difference in segmented pronephros area between *tyrosinase* and *pkd1* crispants, despite an obviously cystic phenotype of many *pkd1* crispant embryos (Fig. 2D,E). To enable automated detection of cystic versus normal kidneys, we took advantage of the classification feature of U-Net. We used isolated kidney areas generated by the 2D-NephroNet segmentation masks as input for a secondary network (2D-CystNet) that assigned a classification of either 'normal' or 'cystic' (Fig. S6C). Classification occurred on a pixel-by-pixel level and a softmax output was provided as a confidence measure of the network (Fig. 2D). Therefore, the network was able to calculate the proportion of the cystic kidney area (Fig. 2E) (Fig. S6D).

Linking 2D-NephroNet and 2D-CystNet in an image-processing pipeline allowed us to evaluate the cystic phenotype of *pkd1* crispants in a fully automated manner. We used this pipeline to map the onset of cystogenesis during development and found that both guide RNAs (2 and 3) elicited a significant increase in cystogenesis over controls, detectable at all stages investigated (Fig. 2E). Higher resolution light-sheet mesoSPIM imaging revealed tubular cysts interspersed with undilated epithelia (Fig. 3A, Fig. S7), reflecting the mosaic nature of CRISPR/Cas9 genome editing. Using DiameterNet (IOU: 0.87), we quantified the tubule diameter along the nephron (Fig. 3A, Fig. S8). Interestingly, cystogenesis has early functional consequences, as bilaterally gene-edited embryos developed generalized edema (Fig. S9), suggesting defective fluid regulation.

Next, we targeted *pkd2* by CRISPR/Cas9-mediated mosaic inactivation in *X. laevis*, resulting in pronephric cysts with variable penetrance for two distinct gRNAs (Fig. S10), similar to the
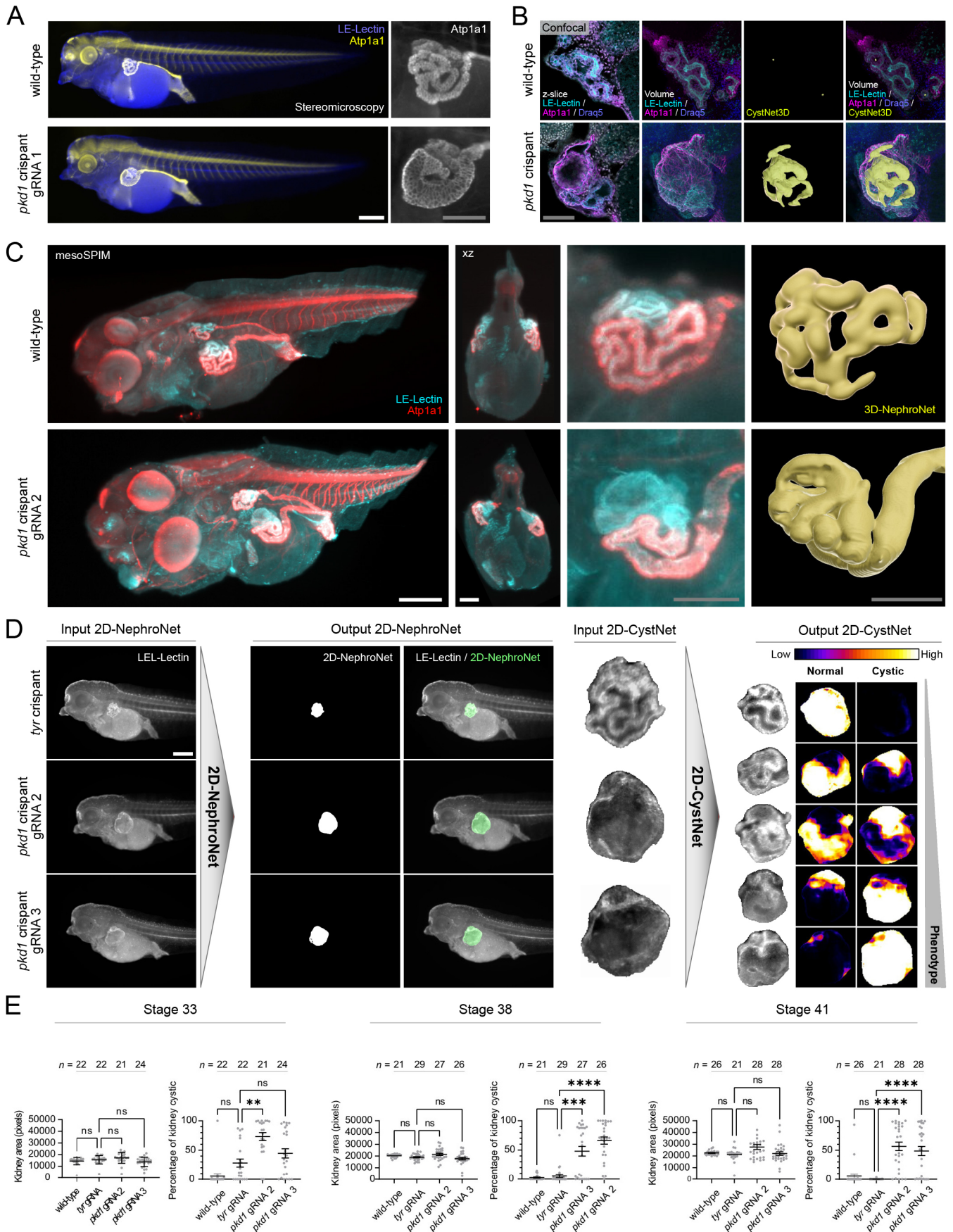
Fig. 2. See next page for legend.

Fig. 2. Deep-learning analysis of a *pkd1* crispant model for autosomal dominant polycystic kidney disease (ADPKD). (A) Immunofluorescence microscopy showed pronounced tubular cystogenesis upon mosaic inactivation of *pkd1* in *X. tropicalis*. (B) Confocal laser scanning microscopy (CLSM) revealed epithelial thinning and luminal expansion in *pkd1* crispants. CystNet3D was used to segment cysts in CLSM stacks (yellow). (C) mesoSPIM light-sheet microscopy *in toto* imaging of a wild-type embryo and a *pkd1* crispant stained for LE-Lectin and Atp1a1. The near-isotropic mesoSPIM recordings were optically resliced on the *xz*-plane. 3D-NephroNet segmentations of pronephric tubules in mesoSPIM recordings. (D) Image processing pipeline for automated quantification of pronephros area and assessment of cystic index. Pronephric area was measured by 2D-NephroNet in input images. Segmentation masks were used to extract the pronephros, then processed by 2D-CystNet. 2D-CystNet outputs two softmax channels, each of which corresponded to either 'normal' or 'cystic' morphology. (E) Fully automated measurements of kidney tubule area and percentage of cystic area across three developmental stages of *X. tropicalis*. Area measurements of pronephric tubules were not significantly different when comparing *tyrosinase* (*tyr*) control crispants with *pkd1* crispants. In contrast, measuring the percentage of cystic areas detected a significant difference between *tyr* and *pkd1* crispants. (Kruskal–Wallis with Dunnett's multiple comparison: ns, not significant, **P<0.01, ***P<0.001, ****P<0.0001). Data are mean±s.e.m. Scale bars: 100 μm (white); 50 μm (gray).

phenotype of *pkd1* crispants. Finally, we extended our U-Net phenotyping to a stable *pkd2* knockout line in *X. laevis* (Fig. 3B,C). Transfer learning to fine-tune 2D-NephroNet (IOU: 0.86) and 2D-CystNet (IOU: 0.86) to this dataset revealed a significant increase in gross pronephros volume and cystic index in *pkd2*$^{-/-}$ animals (Fig. 3E, Fig. S11). In contrast to the mosaic phenotype in crispants, the complete pronephric tubule was severely dilated in *pkd2*$^{-/-}$ embryos. In addition, an EmbryoNet (IOU: 0.98) was trained to isolate animals from the background allowing feature extraction revealing that *pkd2*$^{-/-}$ embryos were smaller, shorter and exhibited extensive dorsal curvature, when compared with heterozygotes or wild types (Fig. 3D,E, Fig. S12).

In conclusion, mutations of *pkd1* and *pkd2* elicited cystic malformations in developing renal tubules. The early onset of cystogenesis suggests a possible disconnect to defective ciliary flow sensing (Nauli et al., 2003). In addition, the fully automated quantification of cysts in *Xenopus* embryos is independent of developmental stage, target gene and species, and is thus a screenable assay.

Deep-learning analysis of embryonic neural disease models

DYRK1A variants lead to a distinct congenital syndrome that commonly includes autism spectrum disorder, and Dyrk1a was shown to regulate cell-cycle progression during neurogenesis in *X. tropicalis* (Dang et al., 2018; Satterstrom et al., 2020; Willsey et al., 2020). The phenotype previously observed in *dyrk1a* knockdown and knockout embryos was most prominent in the telencephalon (forebrain). We explored whether deep learning could similarly assist in the assessment of neural phenotypes and segment morphologically distinct brain regions. We trained TelenNet (IOU: 0.90) to segment the telencephalon on *Xenopus dyrk1a* morphants stained for β-tubulin (Fig. S13A) and deployed this model to quantify the telencephalon area on *dyrk1a* unilaterally injected crispants (Fig. 4A).

Test data were annotated by two experts independently to analyze how TelenNet correlated to each annotator. There was no significant difference between measurements of telencephalon areas based on ground truth annotations from annotator one, who had labeled the training data, on ground truth annotations from annotator 2 and on TelenNet segmentations (*P*=ns) (Fig. 4B,C). As an extension to TelenNet, we trained a U-Net to detect four distinct brain regions of

X. tropicalis in the same images (BrainNet - IOU: 0.88) (S13B). This multi-class segmentation was able to distinguish each region with high accuracy (Fig. 4D), suggesting that U-Net-based analysis is more generally applicable to analysis of region-specific phenotypes.

Next, we aimed to quantify proliferation rates in forebrains of DMSO and Harmine-treated embryos. Harmine is a pharmacological inhibitor of DYRK1A (Göckler et al., 2009) and has been shown to stall neural cell cycle progression at both S and M phases in *Xenopus* (Willsey et al., 2020). We used a transfer learning approach to retrain TelenNet to accurately segment the telencephalon stained by a different antibody (PCNA, S phase marker) (Fig. S13C). We then used the resulting mask to automatically quantify proliferating neuron progenitor cells detected by phospho-histone H3 (pHH3, M phase marker) staining specifically in the embryonic forebrain using ProliNet (Fig. 4E,F) (Fig. S13D). The number of proliferative cells in M phase was significantly increased in harmine-treated forebrains (Fig. 4G). This highlighted the utility of chained networks in evaluating the effect of chemical compounds *in vivo* in a morphologically distinct anatomical region without observer bias.

Conserved patterning events during neurogenesis create crests and valleys that characterize distinct anatomical regions of the tetrapod brain (Exner and Willsey, 2021). These intricate structures can only be fully appreciated in their three-dimensional form. We trained 3D-BrainNet (IOU: 0.87) to three dimensionally reconstruct a *dyrk1a* morphant brain (Fig. 3H,I; Fig. S13E). All characteristic brain structures, e.g. the hindbrain rhombomeres, became visible. This visualization revealed the reduced telencephalon size on the injected side, while other regions appeared symmetrical.

Deep-learning analysis of craniofacial anomalies

Aberrations in craniofacial development during gestation are a common cause of congenital birth defects and *Xenopus* has been widely used to model disrupted craniofacial development (Dubey and Saint-Jeannet, 2017). Traditionally, orofacial phenotypes are assayed using whole-mount Alcian Blue staining, which reveals the cartilaginous elements. To automate assessment of craniofacial structures from Alcian Blue stained *X. tropicalis* embryos, we trained a multiclass AlcianNet (IOU: 0.75) (Fig. S14A). This network was able to distinguish, correctly segment and classify six distinct structures of the craniofacial cartilages (Fig. 5A).

The *Xenopus* embryonic craniofacial cartilage is a highly intricate three-dimensional structure and altered development is ideally assessed in 3D. For this, we subjected Col2a1 immunostained and cleared embryos to mesoSPIM light-sheet microscopy (Fig. 5B) and trained a U-Net (CranioNet - IOU: 0.80) to segment the craniofacial structures. We trained CranioNet on three sparsely annotated recordings (10% of ~500 slices, *n*=49 per volume) of wild-type embryos and used one sparsely annotated recording (10% of 500 slices, *n*=51) for validation (Fig. S15A). We used this model to reconstruct the craniofacial structures in an unseen recording (Fig. 5B, Movie 1).

Next, we employed an established inhibitor of retinoic acid signaling BMS-453 (Kennedy and Dickinson, 2012) and trained a multiclass FaceNet to explore whether deep-learning approaches could pick up changes in face morphometry by segmenting the eyes, mouth and complete orofacial area (Fig. S14B). In line with previous studies, we demonstrate a clear dose-response effect of BMS-453 affecting orofacial area, face width, distance between the eyes and eye size, but not face height (Fig. S14C). This analysis revealed that the most-sensitive parameter was distance between the eyes, which
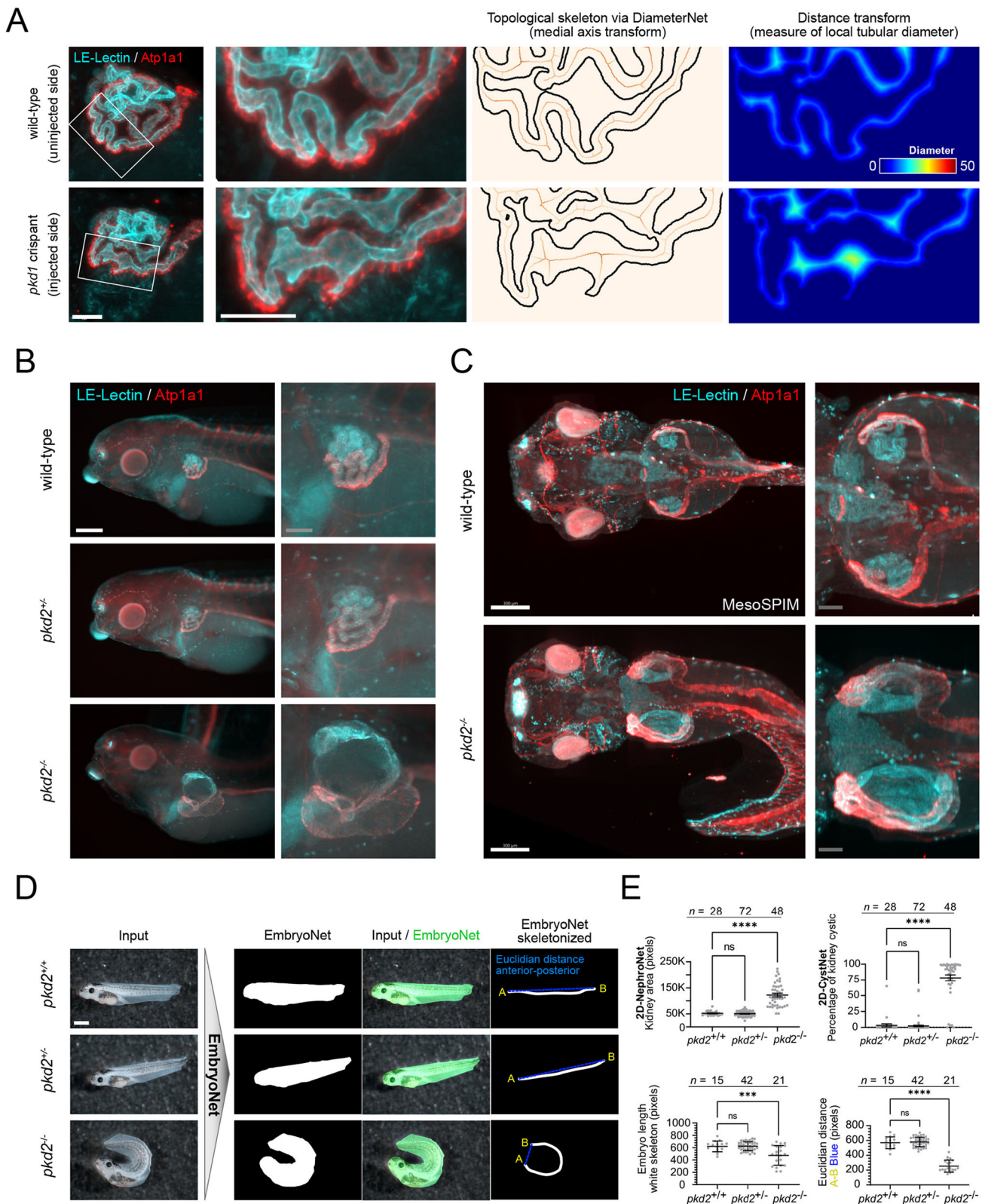
Fig. 3. Localized renal cysts in *pkd1* crispants and phenotypic characterization of a *pkd2* knockout line. (A) High-resolution mesoSPIM imaging was used to generate a topological skeleton via DiameterNet and a distance transformation was used as a measure of local tubular diameter. Scale bars: 50 μm. (B) Immunofluorescence microscopy showed pronounced tubular dilation in *pkd2* knockout *X. laevis*. Scale bars: 300 μm (white); 100 μm (gray). (C) mesoSPIM light-sheet microscopy *in toto* imaging of *pkd2*^{+/+} and *pkd2*^{−/−} embryos (dorsal view). Scale bars: 300 μm (white); 100 μm (gray). (D) Bright-field images of *pkd2*^{+/+}, *pkd2*^{+/−} and *pkd2*^{−/−} animals. Scale bar: 1 mm. (E) Fully automated measurements of kidney tubule area and percentage of cystic area using 2D-NephroNet and 2D-CystNet (Kruskal–Wallis with Dunn's multiple comparison: ns, not significant, ****$P<0.0001$). Fully automated measurements of embryo length (Longest Shortest path skeletonized EmbryoNet, white, ***$P<0.001$) and a measure of embryo curliness (Euclidian distance between A and B, blue, ****$P<0.0001$). Data are mean±s.e.m.
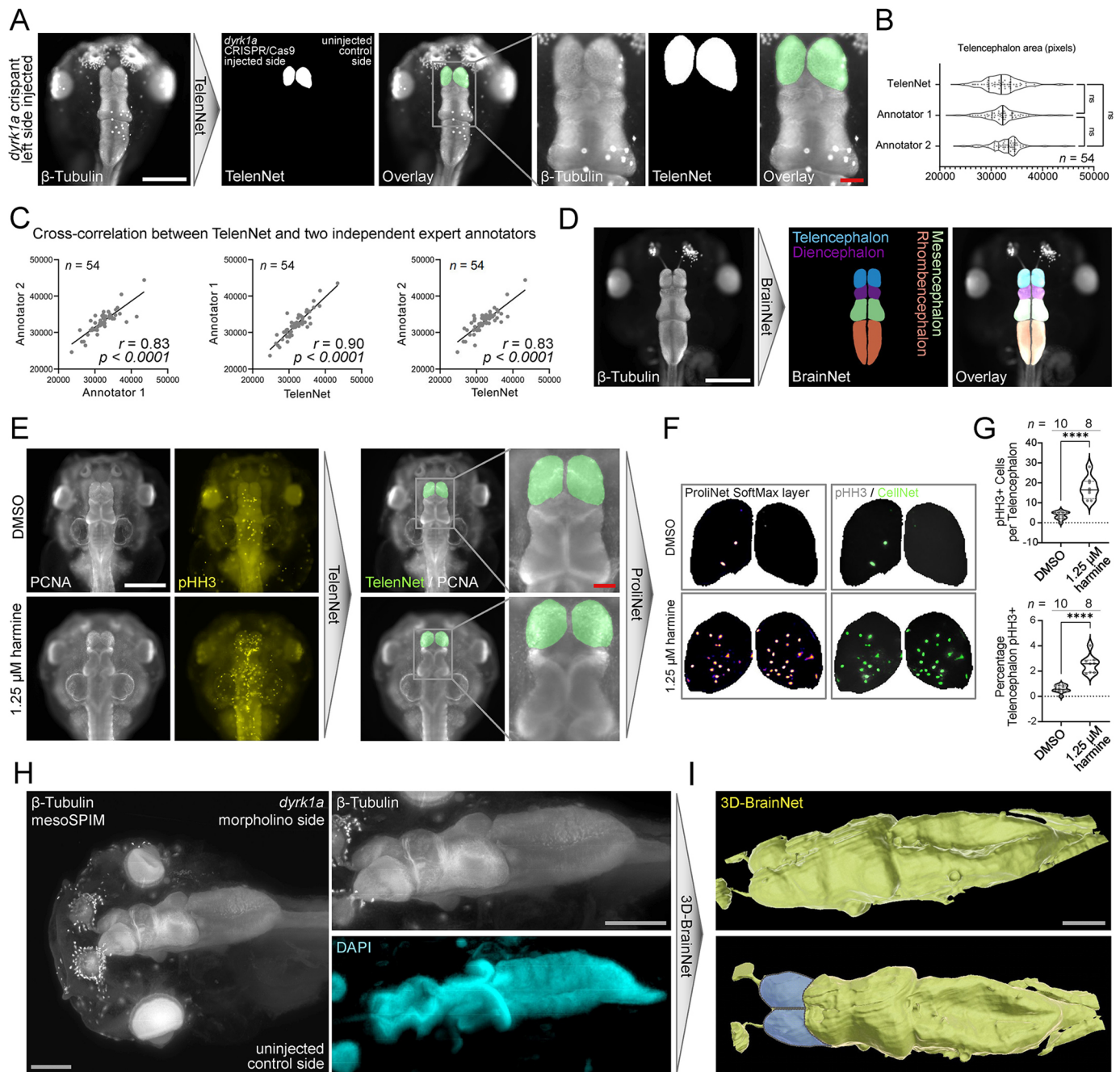
Fig. 4. Deep-learning analysis of neural phenotypes in a *dyrk1a*-depleted embryos. (A) TelenNet for automated segmentation of the telencephalon (forebrain) from whole-mount β-tubulin immunofluorescence stainings imaged by wide-field microscopy of *dyrk1a* CRISPR/Cas9-edited embryos. TelenNet independently segmented the telencephalon on either side of the midline. (B) Telencephalon area as determined by manual assessment of two independent expert human annotators and TelenNet. As TelenNet was trained by annotator 1, automated measurements were similar to those of annotator 1 (ANOVA, ns; Kruskal-Wallis, ns). (C) Cross-correlation between TelenNet and each independent annotator. (D) BrainNet achieved multiclass segmentation of various brain regions (telencephalon, diencephalon, mesencephalon and rhombencephalon) bilaterally. (E-G) Chained image processing pipeline for cell counting in the telencephalon. (E) TelenNet was fine-tuned to recognize telencephalons in PCNA-stained embryos and the resulting masks were used to isolate the left and right telencephalons from the pHH3-channel. (F) A cell-counting model (ProliNet) identified pHH3$^+$ cells. (G) The number of proliferating (pHH3$^+$) cells in the telencephalon of harmine-treated embryos (unpaired *t*-test: ****$P<0.0001$) and the percentage of telencephalon area covered by pHH3$^+$ cells (unpaired *t*-test: ****$P<0.0001$) were significantly increased. (H) mesoSPIM light-sheet *in toto* imaging of a *dyrk1a* unilateral (right) morphant stained for β-tubulin and counterstained with DAPI. (I) A sparse annotation approach was used to segment the *Xenopus* brain using 3D-BrainNet. The telencephalon is pseudo-colored in blue. Scale bars: 500 μm (white); 100 μm (gray).

already showed a significant decrease at the lowest (1 μM) dose, while face width decreased only from the 5 μM dose upwards.

Next, we 3D-reconstructed the craniofacial abnormalities of embryos treated with different concentrations of BMS-453 and

stained for Col2a1. For this, we fine-tuned CranioNet to the BMS-453 treated samples by exposing the CNN to normal and altered *Xenopus* embryonic craniofacial cartilage in sparsely annotated recordings (2.5% of slices, $n=100$). Of note, adding another sample
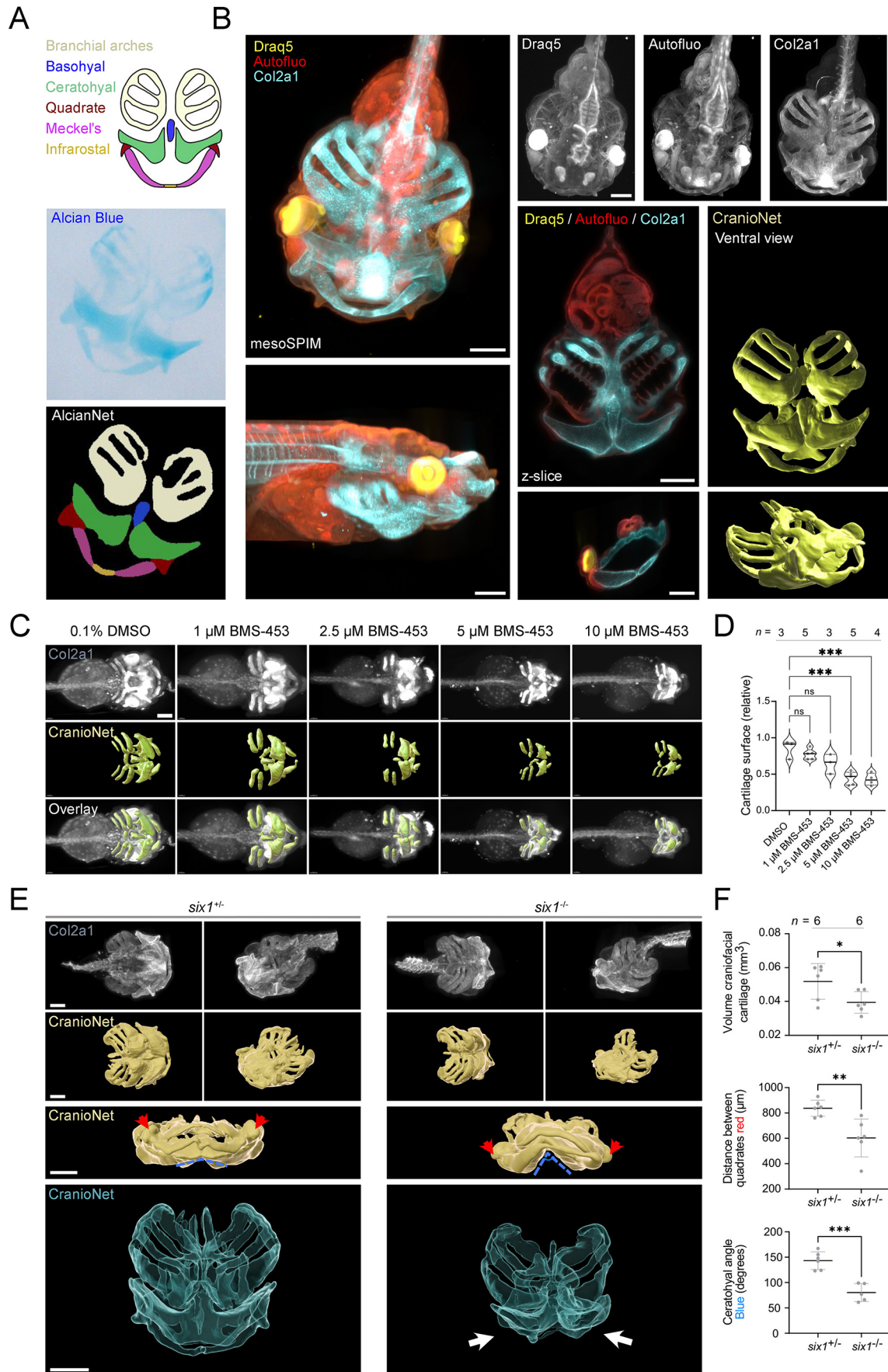
Fig. 5. See next page for legend.

Fig. 5. Volumetric analysis of craniofacial abnormalities induced by retinoic acid inhibition and in *six1⁻/⁻ X. tropicalis* embryos. (A) Schematic of the *Xenopus* craniofacial cartilages. AlcianNet achieved multiclass segmentation of craniofacial elements from Alcian Blue stained *X. tropicalis* embryos. (B) mesoSPIM light-sheet *in toto* imaging of a wild-type embryo stained for Col2a1. CranioNet based 3D-segmentation of craniofacial cartilages (yellow). Autofluorescence (Autofluo, red) recorded at 488 nm excitation. (C) Three-dimensional quantitative phenotyping of *X. tropicalis* revealed a dose-dependent response to the retinoic acid inhibitor BMS-453. (D) Quantification of the normalized cartilage surface revealed a BMS-453 dose-response curve (ANOVA, *P*<0.0001; Holm–Šidák multiple comparison, ***P*<0.001). (E) Morphological differences between *six1* heterozygous and homozygous knockout embryos. The arrows indicate the collapsed dysmorphic Meckel's and ceratohyal cartilages in *six1* knockouts. (F) Quantification revealed lower gross cartilage volume of *six1* knockouts, a decreased distance between quadrates (red arrows) and an increase in the ceratohyal angle (dashed blue line) (unpaired *t*-test: **P*<0.05, ***P*<0.01, ****P*<0.001). Data are mean±s.d. Scale bars: 200 μm.

for each experimental condition (doubling training data, *n*=200), did not substantially improve network training kinetics (Fig. S15B,C). We next deployed this model across recordings of DMSO and BMS-453-treated embryos (*n*=20), revealing a qualitative and quantitative dose-response of BMS-453 on the surface area of three-dimensional reconstructions (Fig. 5C,D). In conclusion, analysis of facial morphometry and 3D volumetric cartilage reconstructions revealed details of retinoic acid-dependent changes in craniofacial cartilage development.

In humans, mutations in *SIX1* are associated with Branchio-oto-renal syndrome (BOR), which is characterized by ear, kidney and branchial arch anomalies (Ruf et al., 2003; Sanggaard et al., 2007). We investigated whether CranioNet could similarly be deployed for in-depth investigation of the craniofacial phenotypes occurring in a *six1* genetic *X. tropicalis* knockout line (Coppenrath et al., 2021). For this Col2a1-stained *six1⁺/⁻* and *six1⁻/⁻* embryos across were subjected to mesoSPIM light-sheet microscopy and base CranioNet was finetuned to this specific experiment (IOU: 0.75) (Fig. 5E) (Fig. S15D). 3D reconstructions revealed that in *six1⁻/⁻* embryos the gross craniofacial cartilage was significantly decreased when compared with *six1⁺/⁻* embryos (Movie 2). Furthermore, these reconstructions allowed us to measure interquadratal distance (dashed red) and the ceratohyal angle (dashed blue), revealing significant differences comparing genotypes (Fig. 5F). Taken together, automated 2D/3D analysis of detailed face morphology and craniofacial elements in *X. tropicalis* using U-Net deep learning uncovered intricate structural details.

Applying U-Net deep learning towards various image modalities

Given the wide range of applications that U-Net proved useful for, we asked what additional imaging modalities it could be applied to. Colorimetric *in situ* hybridization (ISH) detects spatially localized gene expression. Building on images of a previously conducted ISH screen (Kaminski et al., 2016), we aimed to correlate expression patterns of 59 genes. EmbryoNet-ISH (IOU: 0.97) was trained on ISH-stained embryos from eight different stages (stages 10, 15, 25, 28, 33, 35, 38 and 40) (Fig. S16A). Deploying EmbryoNet-ISH on unseen test data showed near-perfect correlation (*r*=0.99, *P*<0.0001) to an expert human annotator, across all stages (Fig. S16B). Next, we deployed EmbryoNet-ISH on unseen data from stages it was not trained on (stages 22 and 26) to mask, crop and register embryos (Fig. 6A). Unsupervised clustering of images revealed a number of co-expression groups, such as Hox genes, genes expressed in the neural crest or pronephric markers. (Fig. 6B).

Overlaying dissimilar expression patterns resulted in a digital multi-channel representation to directly compare *in situ* signals on a digital 'average' embryo (Fig. 6C).

Previously, we have used U-Net mainly on one channel fluorescence images. Next, we combined whole-mount hybridization chain reaction fluorescent ISH (HCR v3.0) against *hnf1b* (proximal tubule and pancreas) together with immunostainings for Atp1a1 (renal tubules and neural tissue), LE-lectin (renal tubule) and nuclear stain (DAPI) (Fig. 6D) (Choi et al., 2018). After mesoSPIM imaging, we used the recordings of all four channels to train several U-Nets on sparse annotations to reconstruct multiple anatomical structures (VoluNets: eye, brain, peripheral surface, intestine, oral cavity, pancreas and kidney) within the same sample (Fig. 6D,E) (Movie 3) (Figs S17A-D and S18). This also allowed us to precisely localize the strongest expression of *hnf1b* to the proximal segments of the pronephros (PT2/3), sparing the nephrostomata. Because U-Net-based segmentation relies on morphologically recognizable features, reconstruction of structures that were not specifically labelled (i.e. eyes, oral cavity and intestine) was possible.

Finally, the mammalian kidney consists of thousands of intertwined nephrons, each partitioned into functionally specialized segments. We were interested in gaining structural insights into the distal convoluted tubule (DCT), because this segment can expand in size in response to potassium load (Loffing et al., 2004). Kidneys from a DCT-specific reporter mouse model (Slc12a3/NCC-cre-ERT2^Tg/+^:TdTomato-flox^Tg/+^) were CLARITY-cleared and imaged on the mesoSPIM platform, revealing DCT architecture in 3D (Fig. 6F) (Schnoz et al., 2021). Separation and reconstruction of individual DCTs using traditional approaches is challenging because signals of separate DCTs touch one another and are highly intertwined. We trained DCT-Net to distinguish DCT as separate entities, even when in close proximity (Fig. 6F) (Fig. S17E). DCT-Net allowed large scale reconstruction of individual DCTs across a mouse kidney, permitting automated feature extraction such as volumetric measurements (average DCT volume: 530785 ±185043 μm³). In conclusion, applying U-Net based visual processing tasks is not limited by image modality and is adaptable to the challenges of individual requirements.

DISCUSSION

Here, we illustrate that using computer vision for automated analysis and quantification of datasets in developmental biology is powerful, versatile, reliable and easy to implement. Focusing on models of human congenital diseases, we applied existing off-the-shelf deep-learning tools to a broad range of real-world applications. In that process, we trained over 15 deep-learning networks to perform varied tasks. From quantifying the proportion of cystic tubules in the embryonic kidney of three novel ADPKD models, to counting proliferating cells specifically in the telencephalon of an autism model, to identifying specific defects of craniofacial malformations in a model of *SIX1*-associated branchiootic syndrome.

Settings for successful implementation

Deep-learning models that try to generalize as broadly as possible, e.g. cell segmentation across different cell types, still encounter commonly perceived road-blocks, such as requiring large amounts of high-quality datasets and long training times (Stringer et al., 2021). For most image analysis tasks we encountered, these roadblocks do not apply, because imaging conditions can be sufficiently standardized within an experimental setup. Instead of focusing our efforts on a single biological question, and solving this in depth by novel deep-learning network development and
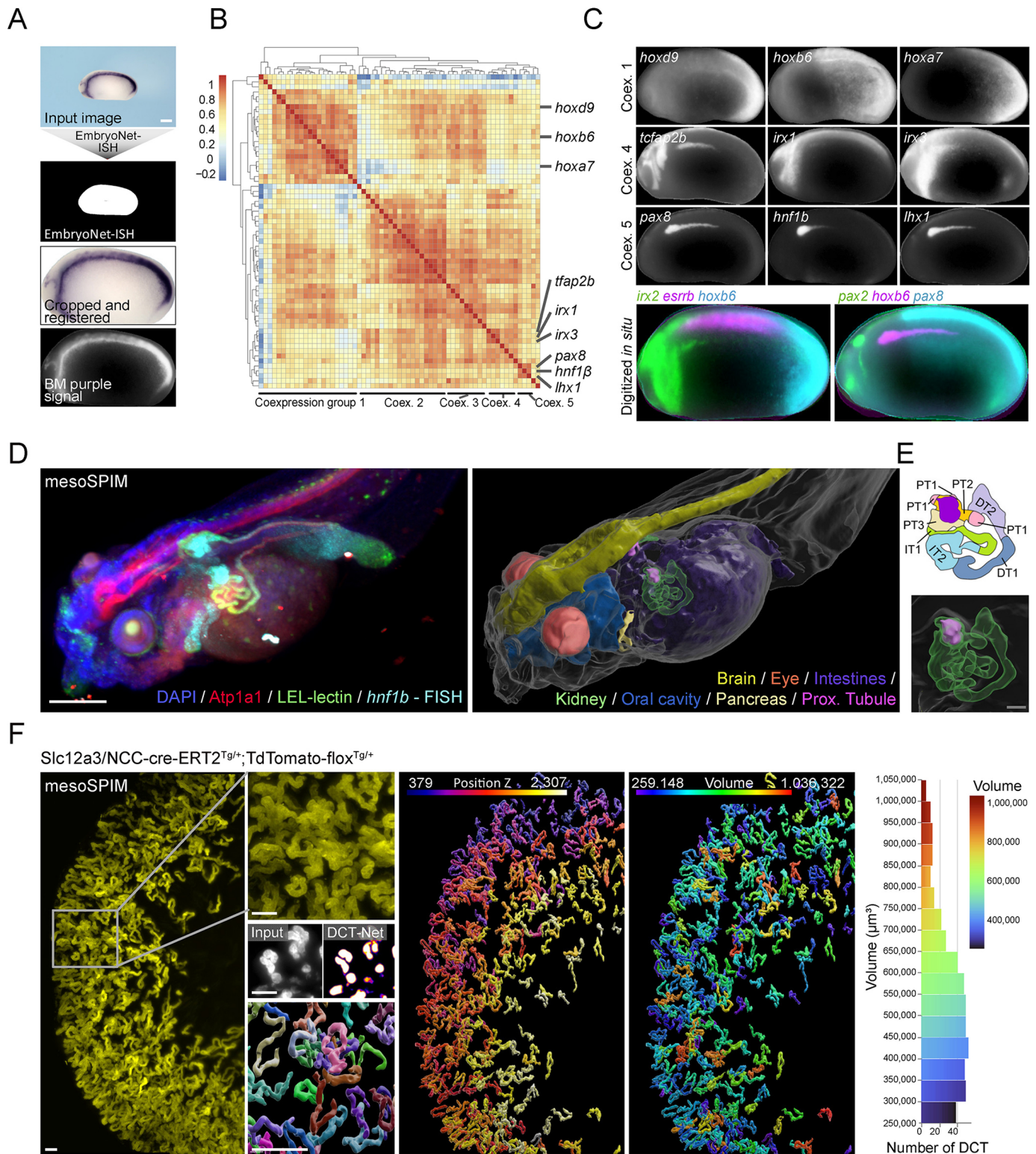
Fig. 6. Deep learning is applicable to various imaging modalities. (A) EmbryoNet-ISH accurately segmented colorimetric whole-mount *in situ* hybridization (WISH) stained embryos. (B) Segmentation masks were used to extract, crop and register the *in situ* signal of stage 26 *X. laevis* embryos. Unsupervised clustering (*n*=63) identified distinct co-expression groups. (C) Example images confirmed similar expression patterns within co-expression groups; divergent expression patterns are visualized in multichannel images. (D) mesoSPIM recording of a stage 45 embryo stained for *hnf1β* using hybridization chain reaction FISH (HCR v3.0), LE-lectin and anti-Atp1a1. DAPI was used as a counterstain. Various morphological structures were segmented in 3D using U-Net models, revealing *hnf1β* to most strongly expressed in the proximal tubular segments PT2/3 (purple label) and pancreas. (E) Schematic and enlarged view of the pronephros segmentation. (F) mesoSPIM recording of the adult kidney of an induced Slc12a3/NCC-cre-ERT2[Tg/+]:TdTomato-flox[Tg/+] reporter mouse to visualize the distal convoluted tubules (DCT). DCT-Net segmented single DCTs and maintained separation of DCTs in close proximity. DCT-Net 3D-segmentations highlighted the spatial distribution of DCT in the renal cortex and permitted feature extraction such as volume measurements. Scale bars: 200 µm (white); 40 µm (gray).

optimization, we applied out-of-the-box U-Net-based analysis on a plethora of real world use cases and image modalities. This provided valuable experience and practical insights into how and where to implement deep-learning tools. First, implementing a powerful deep-learning network into an analysis workflow is now surprisingly easy and fast. The U-Net Fiji plug-in was developed to be macro language compatible and can be deployed on consumer-grade GPUs (Falk et al., 2019; Gómez-de-Mariscal et al., 2021). In addition, free cloud based training and prediction tools are available to the research community (von Chamier et al., 2021). These now allow for cost-efficient training and deployment. Second, we were repeatedly surprised by the minimal amount of annotated data needed to train a U-Net. We encountered multiple instances (2D-NephroNet, CranioNet) where adding additional training data did not improve network performance. Thus, training on a very small number (i.e. ten images) of representative samples can be sufficient. The training parameters are provided in Table S2, which can serve as a reference for new implementations. Third, we observed that trained models generalized well across different experiments. For example, TelenNet was trained on a very prominent morpholino phenotype, and was still able to accurately quantify rather subtle differences in brain sizes in CRISPR/Cas9-targeted embryos. Finally, as networks often train better if they integrate contextual information, we scaled the input image to fit the maximum tile size within the vRAM of a consumer-grade GPU. This was particularly useful when labeled structures only appeared once per image. We thus avoided distortions at tile edges.

Neural networks perform best when they are trained on data that fully represent the characteristics of the test data. Specifically, training on both normal and phenotypically abnormal embryos is needed to achieve a highly accurate performance. One inherent limitation is that neural networks cannot recognize unseen pathological states or can be misled by variations they were not trained on, and ideally the training images need to be representative of test data. However, a fully trained network can be fine-tuned to recognize a new phenotypic variation or dataset with differing characteristics by spiking in, at most, a couple of images of the new experiment (Figs S6A and S13C). We provide instructional videos on implementation, training, fine-tuning and all pre-trained weight files online (https://lienkamplab.org/deep-learning-models/). These can serve as anchor points to adapt the models to a similar problem, but on slightly different images, such as different developmental stages, microscope setups or antibody staining.

Most U-Net deep-learning implementations perform data augmentations, such as rotation, stretching or other distortions on the training data to increase performance across natural biological variability (Falk et al., 2019; von Chamier et al., 2021). For example, networks trained to segment embryos of one clutch (EmbryoNets) performed reasonably well on different clutches, but best when images of different clutches are present in the training data (Fig. S19).

During this study, we did not notice any limits on what particular structures were more or less suitable for automated segmentation by deep learning. Most, if not all humanly identifiable morphological features could be trained for, independent of their intensity pattern or frequency of occurrence.

The U-Net plug-in generated both a binary segmentation mask and a softmax heatmap as output. In some cases, we noticed that, despite relatively low metrics being reached during training, the raw softmax output layer often contained all the information necessary for useful segmentation. Although whether softmax layers are really

a proxy for network certainty is debated, in practice we saw that thresholding the softmax probability distribution often removed false-positive firing regions and generated precise segmentations. We also often applied largest blob filters, either in 2D or 3D, to remove smaller false-positive segmentations. Using the Fiji macro language, networks can be tied into more complex, customizable pipelines with sequential analysis steps. By chaining multiple segmentation (TelenNet+ProliNet) or segmentation and classification tasks (NephroNet+CystNet), U-Net predictions can be performed at scale.

Deep learning unlocks the power of light-sheet microscopy

Deep learning facilitates analysis on datasets of sizes and complexity that would be prohibitive to process manually. One such case is automated analysis of light-sheet microscopy data, which is known to cause a data deluge (Reynaud et al., 2015). Indeed, our mesoSPIM imaging setup generated over 100 gigabytes of data per hour or around 15,000 single images. The amount of data prohibits manual extraction of meaningful data. Here, we applied deep-learning approaches for 3D *in toto* phenotyping of *Xenopus tropicalis* and demonstrated how integrating U-Net approaches allowed the quantitation and unbiased, fully automated assessment of phenotypes. Training U-Net models on sparsely annotated single embryos in datasets generalized well towards other embryos within the same experiment.

In summary, we extensively explored the utility of U-Net based CNN implementations for a number of biological questions. Indeed, CNNs have become so advanced that most menial image analysis tasks that wet-lab researchers commonly encounter can be considered simple from a computer vision perspective. In our experience, deep learning enabled analyses that are impossible or unrealistically labor intensive. This presents unprecedented possibilities for developmental biology and beyond.

Models of human congenital disorders are evaluated by deep-learning analysis

More specifically, embracing deep learning can have profound advantages for the field of embryonic disease modeling. As CRISPR/Cas9 now allows for high-throughput investigation of gene function in early development (Kroll et al., 2021; Naert et al., 2020b), phenotyping, rather than generating the models, presents a challenge. We demonstrate examples of how U-Net deep learning can be harnessed for automated analysis of CAKUT, polycystic kidney disease, autism spectrum disorder, microphthalmia and craniofacial dysmorphia models in *Xenopus*.

CRISPR/Cas9-mediated gene editing of *pkd1* and *pkd2* resulted in penetrant cystogenesis in early *Xenopus* tadpoles. Although increased proliferation and intraluminal pressure build up contribute to cyst growth, the cyst initiating event is still elusive. As renal tubulogenesis can be readily observed *in vivo* in *Xenopus* (Lienkamp et al., 2012), these models may reveal what cellular mechanisms result in cystogenesis. For this, the mosaic occurrence of gene-editing events is beneficial as it mimics the pathological findings in ADPKD, where cysts are scattered throughout the kidney and arise from tubule cells with a rare biallelic loss of *PKD1* or *PKD2*. *pkd2*$^{-/-}$ embryos of the novel *pkd2* knockout line described here also have massive and highly penetrant tubular dilation. In contrast to the crispants, this occurs throughout the pronephric tubule, providing a model with less inherent variability but more distant from the clinical situation. Of note, *Xenopus pkd2*$^{-/-}$ embryos have a 'curly-up' phenotype, in direct agreement with zebrafish mutants (Schottenfeld et al., 2007).

The sequential U-Net pipeline we used to recognize the kidney and deduce a cystic index opens the door to wider screening efforts exploiting these novel ADPKD models. Although mouse and zebrafish models of ADPKD exist, they each have certain drawbacks that *Xenopus* models could complement well (Metzner et al., 2020, 5). For example, duplicated *pkd1* genes in zebrafish act partially redundant (Mangos et al., 2010), whereas conditional mouse alleles show a strong early phenotype, but are not ideal for screening purposes (Menezes and Germino, 2013). Our analysis pipeline will empower high-throughput chemical or genetic screens to identify potential modifiers of cystogenesis. Indeed, *X. tropicalis* is increasingly being used for higher-throughput identification and validation of candidate disease-causing genes across different organ systems (Deniz et al., 2019; Willsey et al., 2021). Previous *in vivo* chemical or genetic screens readily uncovered malformations obvious enough to be detected by eye (Goda et al., 2006; Kälin et al., 2009; Tomlinson et al., 2009). Monitoring phenotypes using deep learning may improve the sensitivity of genetic and chemical screens towards subtle alterations while tremendously reducing labor costs.

In addition, we used CranioNet to three dimensionally reconstruct the craniofacial cartilage of a recently established *six1* *Xenopus* knockout line (Coppenrath et al., 2021). These investigations allowed us to accurately pinpoint abnormalities of the anterior craniofacial elements, specifically the Meckel's and ceratohyal cartilage. The ability to generate high-resolution 3D reconstructions of this model will facilitate further studies into genetic or chemical modifiers of *six1*-related branchio-oto-renal syndrome (Tavares et al., 2021).

The deep-learning field is rapidly generating novel concepts, and it optimizes design principles and keeps outperforming previous iterations. In this scope, we believe integration of novel concepts, such as Bayesian uncertainty and bona-fide 3D network architectures, will soon be available and will continue to improve automated data analysis in developmental biology. In summary, we deliberately tested 'out of the box' deep-learning tools tailored to a non-computer scientist audience and found them to be highly useful, versatile and easy to deploy. It will be fascinating to see how their application to understanding of human inherited diseases will further mechanistic insights and therapeutic development.

MATERIALS AND METHODS
Xenopus experiments
All experiments involving animals were conducted in accordance with local legal and institutional guidelines, and approved by the governing authorities (Regierungspräsidium Freiburg, Veterinäramt Zürich, UCSF IACUC). *Xenopus laevis* were purchased from Nasco, *Xenopus tropicalis* were purchased from the European Xenopus Resource Centre. Ovulation was induced by injection of β-hCG and embryos were *in vitro* fertilized or obtained by natural matings. Staging was carried out according to Faber and Nieuwkoop (2020). *Xenopus laevis* embryos were cultured in Ficoll (GE Healthcare) for 24 h after injection and subsequently in 0.3×Marc's Modified Ringer's [MMR, HEPES (free acid) 5 mM, EDTA 0.1 mM, NaCl 100 mM, KCl 2 mM, MgCl$_2$ 1 mM and CaCl$_2$ 2 mM]. Human Tbx18 (BC132715) cDNA was cloned into VF10 expression vectors and mutations were introduced by site-directed mutagenesis PCR (Hoff et al., 2013). Plasmids were linearized using SalI and mRNA was *in vitro* transcribed using the T7 mMESSAGE mMACHINE kit (Ambion). For targeting of the pronephros, 100-300 ng mRNA was injected into *Xenopus* ventrolateral vegetal blastomeres at the four- to eight-cell stage.

Guide RNAs for crispant experiments were designed, generated and delivered as previously described (Oligos: Table S1A) (Naert and Vleminckx, 2018a; Naert et al., 2020b). *X. laevis tyr* gRNAs were used as previously described (Wang et al., 2015). Assessment of gene-editing

efficiencies was performed by Sanger analysis and trace deconvolution analysis as previously described (primers are listed in Table S1C) (Brinkman et al., 2014; Naert and Vleminckx, 2018b). *X. tropicalis* embryos were injected with precomplexed gRNA/Cas9 RNPs (PNA bio, CP01) at the concentrations and in the blastomeres, as shown in Table S1B. *Dyrk1a* morphants and crispants are generated as described previously (Willsey et al., 2020). The *six1* stable knockout line has been previously described (Coppenrath et al., 2021).

For chemical inhibition, BMS-453 (Tocris, 3409) was dissolved in DMSO at a 10 mM stock solution. Tadpoles at stages 24 to 30 were treated with BMS-453 when RARγ is expressed in the facial prominences during early orofacial development (Kennedy and Dickinson, 2012, 2014). Stock solution was diluted in 0.1×MMR and embryos were treated at following concentrations: 10 μM, 5 μM, 2.5 μM, 1 μM and 0.1% DMSO control. Harmine treatment was performed as previously described (Willsey et al., 2020). Embryos were treated with 0.003% 1-phenyl-2-thiourea (PTU) after hatching to inhibit pigment formation.

Generation and husbandry of pkd2 knockout line
pkd2 is a single copy gene in *X. laevis*. We designed one sgRNA (T1) to the first coding exon of *Xenopus laevis pkd2* and one sgRNA (T2) to the fourth coding exon using CRISPRScan (https://www.crisprscan.org/) (Moreno-Mateos et al., 2015): T1, GGCGTGGGAGCTGGGCGCAA; T2: GGGACATGTGGTACAATAAT. T1 is located 441 bp into exon 1, while T2 target is 34 bp into exon 4 and targets the Polycystin cation channel region. Guide RNAs were synthesized by *in vitro* transcription of the sgRNA PCR template using the SP6 MEGAscript kit (Ambion, AM1330). We injected T1 and T2 separately to test for efficacy of each sgRNA independently. F0 founders were generated by injecting one-cell *X. laevis* J strain embryos (RRID: NXR 0024) with both T1 and T2 sgRNAs; 750 pg of each sgRNA and 1500 pg Cas9 were injected at 10 nl per embryo. Animals were housed in recirculating aquatic systems at the National *Xenopus* Resource (NXR) (RRID:SCR_013731); husbandry methods and parameters can be found elsewhere (McNamara et al., 2018; Shaidani et al., 2020, 2021a,b). Fifteen F0 founders survived through metamorphosis; however, one was lost to bloating and apparent polycystic kidneys. These founders were then outcrossed to wild type to generate F1 offspring and screened for germline mutations. Embryos were collected and genomic DNA was isolated using Sigma-Aldrich GenElute Mammalian Genomic DNA Miniprep Kit (G1N350-1KT). This product was then amplified by PCR (forward primer, 5′-AATTTGCTATAGTGCTCTGCGGGG-3′; reverse primer, 5′-GGAACAGCGTATGTACCTGATGCG-3′), purified using NucleoSpin PCR Clean-up procedure (Macherey-Nagel 740609.250) and mutations were confirmed by sequencing. DNA was obtained from adult frogs via biopsy punch (VWR 21909-140) of the hindlimb webbing. Only one (male two) produced offspring with germline mutations; seven individuals did not produce offspring; four females showed no germline transmission. Initial genotyping of male two F1 embryos contained a −16 bp mutation at the T1 target site and a −20 bp mutation at the T2 target site. We genotyped the 27 siblings that survived to adulthood and identified four individuals with a T1−16 bp mutation and a T2−20 bp mutation, three with a T1−9 bp mutation and a T2−20 bp mutation, five with a T2−3 bp mutation, three with a T2−20 bp mutation, three with a T2−11 bp mutation, one with a T2−11 bp mutation, one with a different T2−20 bp mutation, and seven with no mutations. The initial −16 bp deletion produces a frameshift at amino acid 152, resulting in a stop codon at amino acid 169. This yields the downstream T2 mutation inconsequential. The T1−16 T2−20/+ (*Xla.pkd2^{em1Horb}*, RRID: NXR_2010) and the T1−9 T2−20/+ (*Xla.pkd2^{em2Horb}*, RRID: NXR_2146) *pkd2* mutants are available from the NXR (https://www.mbl.edu/xenopus). To generate additional T1−16 bp T2−20 bp/+ *pkd2* mutants, F1 individuals were outcrossed to wild type. F2 pairs were naturally mated for this study. F3 *pkd2* mutant embryos were anesthetized with 0.1% MS-222 (tricaine methanesulfonate) (Syndel Laboratories) at stage 42, fixed in MEMFA (10 ml 10×MEMFA salts, 10 ml 37% formaldehyde and 80 ml NF H$_2$0) and stored in 100% ethanol at −20°C. Genomic DNA was then isolated from tail clips collected from fixed tadpoles. Individual genotype was assessed using short amplicon primers and visualizing gel electrophoresis band separation on a 2.5%

agarose gel using two sets of primers: T1 forward primer, 5′-GGTTATCAT-CACCACGGCC-3′; T1 reverse primer, 5′-CGGAGCAGCAAAGT-TACTGC-3′; T2 forward primer, 5′-CTGTAGTTTATGGAAGGTCCC-3′; T2 reverse primer, 5′-CCAGCTCAGAGTTAAGAATGG-3′.

Whole-mount Alcian Blue and immunostaining

For Alcian Blue staining solution, 0.01 mg of Alcian Blue (A3157, Sigma) was dissolved in 400 µl ultrapure water added dropwise until solvated. Next, 20 ml of 80% ethanol/20% glacial acetic acid was added dropwise; this precluded formation of Alcian Blue precipitates. Embryos were fixed for 4 nights in 100% ethanol. Next, Alcian Blue staining was performed by using the following treatments: 80% ethanol/20% glacial acetic acid (20 min), Alcian Blue staining solution (6 h at room temperature), 80% ethanol/20% glacial acetic acid (overnight), 100% methanol (3 times for 10 min each), 10% H_2O_2/23% H_2O/66% methanol (until bleached), 50% methanol/50% 1×PBS (30 min), 25% methanol/75% 1×PBS (30 min), 100% PBS (30 min), 1% KOH in 1×PBS (until cleared or for 2 h at room temperature), rinsed in saturated sodium tetraborate and stored in 1×PBS. Whole-mount immunofluorescence was adapted as previously described (Willsey et al., 2018). Embryos were fixed in 4% paraformaldehyde for 40 min at room temperature or in 1×MEMFA overnight at 4°C. Embryos were fully dehydrated to 100% methanol overnight at −20°C. Bleaching was performed under strong light in 10% H_2O_2/23% H_2O/66% methanol, to reduce the formation of air bubbles, until depigmented (from hours up to 2 days). Embryos were rehydrated and permeabilized in 1×PBS with 0.1% Triton X-100 (PBT). Embryos were blocked for 1-2 h in 10% CAS-Block (Life Technologies) and incubated in primary antibody diluted in 100% CAS-Block overnight. The following primary antibodies were used: β-Tubulin (1:100, DSHB, clone E7), PCNA (1:50, Life Technologies, clone PC10), phospho-histone H3 (1:100, Ser10, Sigma, 06-570), LE-Lectin-DyLight488 (1:100, ThermoScientific, L32470), Atp1a1 (1:200, DSHB, A5) (Vize et al., 2009) and Col2a1 (1:200, DSHB, II-II6B3). For nuclear counterstaining, DAPI (20 µg/ml, ThermoFisher, D1306) or Draq5 (1:500, eBioScience, 65-0880-92) was added to the primary antibody mixture. Embryos were washed for 30 min with PBT, blocked again for 2 h and incubated with secondary antibodies [1:250, goat anti-mouse IgG (H+L) secondary antibody, DyLight 488 (35502, ThermoFisher Scientific), goat anti-mouse IgG (H+L) secondary antibody, DyLight 550 (84540, ThermoFisher Scientific), goat anti-mouse IgG (H+L) secondary antibody, DyLight 633 (35512, ThermoFisher Scientific), Alexa Fluor 555 goat anti-mouse IgG (minimal x-reactivity) antibody (405324, P4U/BioLegend UK), goat anti-rabbit IgG (H+L) cross-adsorbed secondary antibody, Alexa Fluor 633 (A-21070, ThermoFisher Scientific)] diluted in 100% CAS-Block overnight at room temperature. Embryos were washed for 1 h with PBT and then 1 h in PBS. For *Xenopus* mesoSPIM imaging, embryos are embedded in 2% low-melting agarose and dehydrated as follows: 75% methanol/25% 1×PBS (15 min), 50% methanol/50% 1×PBS (15 min), 25% methanol/75% 1×PBS (15 min), three times in 100% methanol (2×45 min, 1×45 min to overnight – longer is better). Clearing was performed in BABB (benzyl alcohol:benzyl benzoate 1:2) overnight.

Conventional and fluorescent *in situ* hybridization

Colorimetric *in situ* hybridization was performed as described previously (Hemmati-Brivanlou et al., 1990). The *in situ* images were produced as part of a previous screen for transcription factor expression patterns (Kaminski et al., 2016). U-Net output masks were used to crop a segmentation image, which was then scaled to an equal size. Correlation analysis and heat mapping was carried out in R-Studio 1.1.456.

Hybridization chain reaction (HCR v3.0)

HCR (v3.0) was adapted from manufacturer's suggestions for whole-mount zebrafish embryo and larvae staining to *Xenopus* embryos (Molecular Instruments) (Choi et al., 2016, 2018). PTU-treated embryos were fixed in 1×MEMFA for 30 min at room temperature and washed for 3×5 min with 1×PBS to stop the fixation. Embryos were dehydrated and permeabilized using a series of methanol washes with 100% methanol for 4×10 min and 100% for 1×50 min, and kept at −20°C overnight. Embryos were then

rehydrated with a series of graded 5 min washes with methanol/PBST (1×PBS, 0.1% Tween 20) as follows: 75% methanol/25% PBST, 50% methanol/50% PBST, 25% methanol/75% PBST and 5×100% PBST. Following Proteinase K treatment (30 µg/ml) for 20 min, embryos were briefly washed twice with PBST. Embryos were post-fixed for 20 min with 1×MEMFA and then washed for 5×5 min with PBST. Samples were pre-hybridized with Probe Hybridization Buffer (Molecular Instruments) at 37°C for 30 min. Probe solution was prepared by adding 2 µl of 1 µM stock (2 pmol) of the HCR Probe Set (*X. tropicalis*-hnf1b-B1, Molecular Instruments) to 500 µl of Probe Hybridization Buffer. After removal of pre-hybridization solution, embryos were incubated for 16 h at 37°C. Excess probe removal was performed at 37°C, by washing 4×15 min with pre-heated Probe Wash Buffer (Molecular Instruments). Samples were then washed in 5×sodium chloride sodium citrate (SSC) with 0.1% Tween 20 (5×SSCT) twice for 5 min at room temperature. Embryos were pre-amplified with Amplification Buffer (Molecular Instruments) for 30 min at room temperature (equilibrated to room temperature before use). HCR amplifier hairpins h1 and h2 (B1-h1 Alexa Fluor 647 and B1-h2 Alexa Fluor 647, Molecular Instruments) were prepared separately by heating 10 µl of 3 µM stock (30 pmol) at 95°C for 90 s before snap cooling to room temperature for 30 min in the dark. Hairpin solution was prepared by adding snap-cooled h1 and h2 hairpins to 500 µl of Amplification Buffer at room temperature. After removing pre-amplification solution, samples were incubated in hairpin solution for 16 h in the dark, at room temperature. Excess hairpins were removed by washing for 2×5 min, 2×30 min and 1×5 min with 5×SSCT at room temperature.

Mouse kidneys and CLARITY clearing

Slc12a3/NCC-cre-ERT2$^{Tg/+}$;TdTomato-flox$^{Tg/+}$ male mouse was induced with tamoxifen at an age of 5 months (Schnoz et al., 2021). Tamoxifen (Sigma-Aldrich, T5648) was dissolved in ethanol:sunflower oil (1:10). A dose of 2 mg per day was administered to the mice via gastric gavage on 5 subsequent days, 68 days prior to the euthanization. The kidneys of this isoflurane-anesthetized mouse were fixed by retrograde aortic perfusion using 4% PFA in 1×PBS and were then kept in 4% PFA at 4°C for 24 h. Kidneys were bisected longitudinally using a razor blade. Tissue clearing was performed following a modified protocol (Tomer et al., 2014), which proposes a simplified version of the original CLARITY method (Chung et al., 2013), omitting the need for lipid removal by electrophoretic instrumentation. Kidney halves were immersed in hydrogel monomer solution (4% acrylamide and 0.25% VA-044 in 1×PBS) to create an oxygen-free environment and were put on a rocker at 4°C for 48 h. Samples were then placed at 37°C for 3 h to promote polymerization of the hydrogel. After polymerization, samples were put into a clearing solution (200 mM SDS and 200 mM boric acid in H_2O) at 37°C. Every few days, samples were put into fresh clearing solution, until satisfactory transparency was achieved after 20 days. Kidney halves were washed several times with 1×PBST (Triton X-100 and 0.01% sodium azide in PBS) and stored at room temperature. Samples were stabilized in a block of low melting point agarose (1.5% in PBS) and immersed in a solution of 88% Histodenz (Sigma D2158) in PBS adjusted to a refractive index of 1.457 by refractometry, for 3 days on a rocker (Yang et al., 2014). The block of agarose containing the sample was transferred into a quartz cuvette and completely immersed in a refractive index matching solution.

Microscopy and imaging

In toto X. tropicalis embryos and mouse kidneys were imaged using selective plane illumination microscopy (mesoSPIM) (Voigt et al., 2019). For all mesoSPIM recordings, fluorophores were excited with the appropriate laser lines and a quadband emission filter (ZET405/488/561/640, AHF) was employed. Embryos were imaged at either a voxel size of 1×1×1 µm³ or 2×2×2 µm³ (X×Y×Z) using a MVPLAPO1X objective (Olympus).

For high-resolution mesoSPIM imaging, a MVPLAPO2XC objective (Olympus) was used in combination with a dipping cap (Lavision Biotec 205915). The front cover glass of the dipping cap was removed and replaced with a 40×40×40 mm cuvette (Portmann Instruments). This allowed use of the dipping cap while retaining the horizontal detection axis of the

mesoSPIM. For imaging, the cuvette was filled with BABB and the sample clamped in a 3D-printed holder.

Acquisition time using these respective voxel sizes was 7-8 min and 3-4 min per channel, yielding datasets of 7-8 and 3-4 GB in size. Under $2\times2\times2$ μm^3 imaging conditions, three separate embryos fit into one field of view, allowing imaging of three embryos at once to increase imaging throughput. Mouse kidneys were imaged using the tdTomato signal at a voxel size of $1.6\times1.6\times2$ μm^3. Confocal laser scanning microscopy (CLSM) of cleared *pkd1* and wild-type embryos was performed with an SP8 inverse microscope (Leica). Widefield microscopy of *X. tropicalis* brains was performed with a Zeiss AxioZoom V16 widefield stereoscope with or without apotome. All other bright-field and fluorescence stereomicroscopy was performed with a SteREO Discovery.V8 (Zeiss) or MZ10 F (Leica).

Deep learning

All models were trained from scratch unless stated otherwise. This section is summarized in Table S2. Unless explicitly stated otherwise, all images larger than 740,000 pixels were downscaled by a factor required to fit as one tile into the available vRAM memory of a Nvidia GeForce GTX 1080Ti GPU (11 Gb). All ground truth labels used for training and validation were generated by manual annotations on the datasets by one annotator. For cross-correlation and further model validation, expert annotators (defined as post-graduates with >1 year of experience in kidney and/or brain research) were blinded from each other's results until the task was completed.

Tubule-Net was trained in the command line on a 2D U-Net with four down/up samplings, where each resolutional level was replaced with dense blocks (Huang et al., 2017; Ronneberger et al., 2015). In all cases, data augmentation used was deformation using elastic grid spacing of 120 and a magnitude of 10 in the smooth elastic deformation augmentation step. Cropping of (460,460) in (*x,y*) and random rotations in range [0360] was applied. Original images were downsampled by 2 using nearest-neighbor interpolation to avoid non-integer classes. Data were densely annotated and separated into 295 training, 105 validation and 802 testing splits. Training and validation sets were annotated to obtain a good model and then the testing split was used to deploy the model and compute statistics of the kidneys. On the validation set, we achieved 0.78 IoU at 1,320,000 iterations.

All other networks were trained on a classical 2D U-Net architecture using the model architecture of 2D-CellNet and the U-Net Fiji plug-in (Falk et al., 2019). IOU and F1 values reported are as calculated by the U-Net Fiji plug-in.

3D-NeproNet was trained using 150 training and 75 validation images, obtained by taking each 40th section from nine (*n*train=6; *n*val=3) *in toto* mesoSPIM recordings, for 30,000 iterations at learning rate 1E-4 (30,000/1E-4) and 4000 iterations at 5E-5 (4000/5E-5) reaching an IOU of 0.58. 3D-CystNet was trained using 12 training and 10 validation images, obtained by taking each 20th section from confocal imaging stacks, maintaining class balance across a cystic (*n*=1) and a normal (*n*=1) pronephros recording. We trained for 4000/1E-4, 300/5E-5 reaching an IOU of 0.68 across classes.

EmbryoNet (associated with Fig. S4) was trained using one training and one validation image for 1000/1E-4, 500/5E-5 and 200/2E-5, reaching an IOU of 0.87. OrganNet (associated with Fig. S4) was trained using 11 training and four validation images for 1000/1E-4 and 500/5E-5 reaching an IOU of 0.68.

2D-NephroNet was trained on 15, 45, 75 or 105 training images using 18 validation images. Here, class balance between hypoplastic (33%), normal (33%) and cystic (33%) kidneys was maintained in all training datasets. For comparison in training characteristics under differential training dataset sizes, we trained for 20,000/1E-4. For the 2D-NephroNet model 1, we trained for 20,000/1E-4, 5000/5E-5 and 5000/2E-5 using 105 training images reaching IOU 0.80. For 2D-NephroNet model 2, we trained for 4.000/1E-4, 4000/5E-5 and 400/1E-5 using 15 training images reaching IOU 0.76. For fine-tuning 2D-NephroNet to *pkd1* experimental data, we used 30 training images and 30 validation images stratified across the experimental setups and stages. We trained for 1000/1E-4 reaching an IOU of 0.87. For classifying kidneys into 'cystic' or 'normal', we initially fine-tuned 2D-NephroNet model 1 to this dataset (as a different imaging setup was used) for 1000/1E-4 using 30 training images and 30 validation images: we first class balanced evenly across five injection setups (*n*=5) and then

class balanced evenly across three developmental stages (stages 33, 38 and 41). We reached an IOU of 0.88. This 2D-NephroNet was deployed and the segmentation masks were used to isolate kidneys, in order to form a training and validation dataset for 2D-CystNet. We trained using 30 training images and 12 validation images, and class balanced evenly across normal and cystic kidneys (*n* each=5) for three developmental stages (*n* each=3). For training, the entire pronephric structure was labeled as cystic or as normal, as applicable. We trained for 7500/1E-4, 500/5E-5 and 100/1E-5, reaching an IOU of 0.93. For assessing the *pkd2* line, pretrained 2D-NephroNet and 2D-CystNet weights were fine-tuned. 2D-NephroNet was fine-tuned using 30 training images and eight validation images, and trained for 1500/1E-4, 800/5E-5 and 100/2E-5, reaching an IOU of 0.86. 2D-CystNet was fine-tuned using 10 training images and four validation images, class balanced evenly across normal and cystic kidneys (*n* each=5), and trained for 200/1E-4, 100/2E-5 and 100/1E-5, reaching an IOU of 0.87. Upon deployment to test data, a Fiji macro was employed for sequential deployment of 2D-NephroNet and 2D-CystNet for automated measurements of both kidney size and cystic index. Segmentations were obtained by applying a threshold of 0.5 to the softmax layer of both the cystic and normal class softmax output layer. The percentage of cystic kidney was calculated as follows: cystic area/(cystic area+normal area)×100. 3D-NephroNet-PKD1 was trained using 35 training and six validation images for 4000/1E-4 and 1000/1E-5, reaching an IOU of 0.82. DiameterNet was trained using six training and three validation images for 1000/1E-4 and 500/5E-5, reaching an IOU of 0.87.

For TelenNet on β-tubulin stained embryos, we trained using 20 training images and eight validation images (from *dyrk1a* morphants) for 1000/1E-4 and 1000/5E-5, reaching an IOU of 0.9. On test, we deployed TelenNet to *dyrk1a* crispants. For transfer learning of TelenNet to PCNA-stained embryos, we used eight training images and four validation images for 2000/1E-4 and 200/3E-5, reaching an IOU of 0.8. For 2D-BrainNet, we used 10 training images and two validation images for 6000/1E-4, 2000/5E-5 and 1000/1E-5, reaching an IOU of 0.88 average across classes (four distinct brain regions). To train ProliNet, TelenNet was deployed and the segmentation masks were used to isolate single telencephalons in order to form a training and validation dataset. We trained ProliNet using 13 training images and eight validation images for 500/1E-4, reaching an IOU of 0.52. To count the number of pHH3-positive cells in single telencephalons, a Fiji macro was employed for sequential deployment of TelenNet and ProliNet to test data. For 3D-BrainNet, we sparsely annotated a mesoSPIM recording labeling 10% of the data evenly spread across depth to generate training data and labeled 1.8% of the recording for validation. We trained for 1000/1E-4, reaching an IOU of 0.87.

AlcianNet was trained using seven training images and two validation images for 2000/1E-4, 2000/6E-5 and 1000/3E-5, reaching an IOU of 0.75 average across classes (six distinct craniofacial cartilage elements). FaceNet was trained using 10 training images and four validation images for 1000/1E-4, reaching an IOU of 0.64 average across classes (three orofacial regions). Cranio-Net was trained using 147 training and 51 validation images, obtained by taking each 10th section from *in toto* mesoSPIM recordings (three distinct embryo recordings for training, one distinct embryo recording for validation). We trained for 30,000/1E-4, 20,000/5E-5 and 5000/1E-5, reaching an IOU of 0.8. For fine-tuning CranioNet to BMS-453-treated embryos, we trained on 100 images from five mesoSPIM recordings, obtained by taking each 40th section, from one embryo for each experimental condition (DMSO, 10 μM, 5 μM, 2.5 μM and 1 μM). For training with the double amount of training images (*n*=192), we added another embryo from each experimental condition to the training dataset using, again, each 40th section. For validation, we used images (*n*=45) from mesoSPIM recordings of another distinct five embryos, not included in training data, and annotated these every 80th section. We trained for 20,000/5E-5 and 1000/2E-5, reaching an IOU of 0.68 with either 100 or 192 training images used. For fine-tuning CranioNet *six1* embryos, we used three distinct mesoSPIM recordings for training (one wild type, one *six1*$^{+/-}$ and one *six1*$^{+/+}$, n_{train}=78) and three distinct mesoSPIM recordings for validation (evenly across three setups as in train, n_{val}=51). We trained for 20,000/1E-4 and 2000/2E-5, reaching an IOU of 0.75.

EmbryoNet-ISH was trained using 107 training images and nine validation images for 2500/1E-4 and 2500/5E-5 reaching an IOU of 0.97.

VoluNets (brain, surface, eye and *hnf1b* FISH signal) were used to reconstruct structures from a four channel embryo mesoSPIM recording. In order to avoid aberrant normalization occurring across several low intensity channels, images were converted to RGB for training, validation and test. VoluNets were trained using sparse annotation approaches (train=1.35% of the slices, val=1.22% of the slices) VoluNet-surface was trained for 1000/1E-4, 1000/5E-5, 500/3E-5 and 250/1E-5, reaching an IOU of 0.9. VoluNet-brain was trained for 5000/1E-4, 1000/5E-5 and 250/3E-5, reaching an IOU of 0.58. VoluNet-eye was trained for 3500/1E-4, 2500/5E-5 and 1000/2E-5, reaching an IOU of 0.64. VoluNet-*hnf1b* FISH was trained for 5000/1E-4, reaching an IOU of 0.29. VoluNet-intestines was trained for 5000/1E-4, 1000/5E-5 and 500/3E-5, reaching an IOU of 0.64. VoluNet-Pancreas was trained for 5000/5E-5 and 500/3E-5, reaching an IOU of 0.11 and an F1 segmentation of 0.75. For reconstruction of the pronephros in this animal, pre-trained 3D-NephroNet was successfully deployed without any fine-tuning required.

DCT-Net was trained on nine images (860×860×1 pixels), subtiled from the stitched image (3960×3955×1170 pixels) for 2000 iterations at 1E-4, 500 iterations at 5E-5 and 300 iterations at 3E-5, reaching IOU of 0.78. DCT-Net was deployed on sub-tiles using a 5×5 tiling approach (792×791×1170 pixels) and DCT segmentations were obtained by applying a threshold of 0.99 to the softmax layer, which maintained separation of objects in close proximity.

Three EmbryoNet models (EmbryoNet Model 1 through 3, associated with Fig. S19) were trained using one training and one validation image, from different clutches, for 1000/1E-4, reaching respective IOUs of 0.91, 0.93 and 0.91.

Upon deployment of models to mesoSPIM datasets, often we applied a small blob (4×4 pixels) in each *z*-slice that contained the median pixel intensity across the entire 3D recording prior to feeding into the network. This disfavored over-normalization of single *z*-slices, which could lead to false network firing. All visualization and volumetric measurements were performed in Imaris (Bitplane) or Fiji [with ClearVolume (Royer et al., 2015; Schindelin et al., 2012)]. If applicable, filters were applied to find the largest component(s) of the segmentation (to eliminate small noise). For length measurements, the biggest component was skeletonized and the pixels belonging to the skeleton were summed; to extract width and height, a bounding box was used. DiameterNet segmentations (related to Fig. S8) were processed in Python3 using the scikit-image medial axis skeletonization to obtain a topological skeleton and calculate the distance transform (van der Walt et al., 2014). For plotting the distance transform, the images were further treated as numpy arrays, pixel values converted to a list and all zero values (background) were removed before plotting each kidney sample as a binned histogram with a kernel density estimation plotted as a line.

Statistical analysis

Statistical analysis was carried out in GraphPad Prism. All correlations shown are Pearson. Testing for normality was performed and the appropriate test selected accordingly. Data was visualized using the Altair v4 package (VanderPlas et al., 2018), Altair-catplot (Justin Bois, https://github.com/justinbois/altair-catplot), the pheatmap package (R), Seaborn (Waskom, 2021) or GraphPad Prism. All statistical tests were performed as two-sided tests and choice of statistical test was justified. All data met the assumptions of the statistical tests employed. Sample size in the animal studies was not pre-determined and depended on the technical outcomes of the microinjection procedures, CRISPR/Cas9 editing efficiencies and embryo survival rates. Animals were not excluded from the study; no criteria were pre-established. Study design did not require any randomization or researcher blinding to the group allocation of animals included in the study, because automated analysis was performed.

Author contributions
Conceptualization: T.N., S.S.L.; Methodology: T.N., O.C.; Formal analysis: T.N.; Investigation: T.N., P.O., M.B., N.-I.S., M.M.K., Y.X., K.G., M.V., D.P., S.S.L.; Resources: F. Hildebrandt, T.B., O.R., F.F.V., F. Helmchen, J.L., H.R.W., M.E.H., S.S.L.; Writing - original draft: T.N.; Writing - review & editing: T.N., H.W., S.S.L.; Supervision: S.S.L.

Data availability
All pre-trained U-Net weight files and instructional videos on implementation, training and fine-tuning are available at https://lienkamplab.org/deep-learning-models/.

References
Akerberg, A. A., Burns, C. E., Burns, C. G. and Nguyen, C. (2019). Deep learning enables automated volumetric assessments of cardiac function in zebrafish. *Dis. Model Mech.* 12, dmm040188. doi:10.1242/dmm.040188

Baert, L. (1978). Hereditary polycystic kidney disease (adult form): a microdissection study of two cases at an early stage of the disease. *Kidney Int.* 13, 519-525. doi:10.1038/ki.1978.75

Bergmann, C., Guay-Woodford, L. M., Harris, P. C., Horie, S., Peters, D. J. M. and Torres, V. E. (2018). Polycystic kidney disease. *Nat. Rev. Dis. Primer.* 4, 50. doi:10.1038/s41572-018-0047-y

Boyle, B., Addor, M.-C., Arriola, L., Barisic, I., Bianchi, F., Csáky-Szunyogh, M., de Walle, H. E. K., Dias, C. M., Draper, E., Gatt, M. et al. (2018). Estimating global burden of disease due to congenital anomaly: an analysis of European data. *Arch. Dis. Child. Fetal Neonatal Ed.* 103, F22-F28. doi:10.1136/archdischild-2016-311845

Brinkman, E. K., Chen, T., Amendola, M. and van Steensel, B. (2014). Easy quantitative assessment of genome editing by sequence trace decomposition. *Nucleic Acids Res.* 42, e168. doi:10.1093/nar/gku936

Buhmann, J., Sheridan, A., Malin-Mayor, C., Schlegel, P., Gerhard, S., Kazimiers, T., Krause, R., Nguyen, T. M., Heinrich, L., Lee, W.-C. A. et al. (2021). Automatic detection of synaptic partners in a whole-brain Drosophila electron microscopy data set. *Nat. Methods* 18, 771-774. doi:10.1038/s41592-021-01183-7

Campanella, G., Hanna, M. G., Geneslaw, L., Miraflor, A., Werneck Krauss Silva, V., Busam, K. J., Brogi, E., Reuter, V. E., Klimstra, D. S. and Fuchs, T. J. (2019). Clinical-grade computational pathology using weakly supervised deep learning on whole slide images. *Nat. Med.* 25, 1301-1309. doi:10.1038/s41591-019-0508-1

Choi, H. M. T., Calvert, C. R., Husain, N., Huss, D., Barsi, J. C., Deverman, B. E., Hunter, R. C., Kato, M., Lee, S. M., Abelin, A. C. T. et al. (2016). Mapping a multiplexed zoo of mRNA expression. *Development* 143, 3632-3637. doi:10.1242/dev.140137

Choi, H. M. T., Schwarzkopf, M., Fornace, M. E., Acharya, A., Artavanis, G., Stegmaier, J., Cunha, A. and Pierce, N. A. (2018). Third-generation in situ hybridization chain reaction: multiplexed, quantitative, sensitive, versatile, robust. *Development* 145, dev165753. doi:10.1242/dev.165753

Chung, K., Wallace, J., Kim, S.-Y., Kalyanasundaram, S., Andalman, A. S., Davidson, T. J., Mirzabekov, J. J., Zalocusky, K. A., Mattis, J., Denisin, A. K. et al. (2013). Structural and molecular interrogation of intact biological systems. *Nature* 497, 332-337. doi:10.1038/nature12107

Çiçek, Ö., Abdulkadir, A., Lienkamp, S. S., Brox, T. and Ronneberger, O. (2016). 3D U-Net: learning dense volumetric segmentation from sparse annotation. In *Medical Image Computing and Computer-Assisted Intervention - MICCAI 2016* (ed. S. Ourselin, L. Joskowicz, M. R. Sabuncu, G. Unal and W. Wells), pp. 424-432. Springer.

Coppenrath, K., Tavares, A.L.P., Shaidani, N. I., Wlizla, M., Moody, S. A. and Horb, M. (2021). Generation of a new six1-null line in Xenopus tropicalis for study of development and congenital disease. *J. Genet. Dev.* (in press). doi:10.1002/DVG.23453

Dang, T., Duan, W. Y., Yu, B., Tong, D. L., Cheng, C., Zhang, Y. F., Wu, W., Ye, K., Zhang, W. X., Wu, M. et al. (2018). Autism-associated Dyrk1a truncation mutants

DEVELOPMENT

impair neuronal dendritic and spine growth and interfere with postnatal cortical development. *Mol. Psychiatry* 23, 747-758. doi:10.1038/mp.2016.253

Deniz, E., Jonas, S., Khokha, M. K. and Choma, M. A. (2019). Quantitative phenotyping of xenopus embryonic heart pathophysiology using hemoglobin contrast subtraction angiography to screen human cardiomyopathies. *Front. Physiol.* 10, 1197. doi:10.3389/fphys.2019.01197

Dubey, A. and Saint-Jeannet, J.-P. (2017). Modeling human craniofacial disorders in Xenopus. *Curr. Pathobiol. Rep.* 5, 79-92. doi:10.1007/s40139-017-0128-8

Emmert-Streib, F., Yang, Z., Feng, H., Tripathi, S. and Dehmer, M. (2020). An introductory review of deep learning for prediction models with big data. *Front. Artif. Intell.* 3, 4. doi:10.3389/frai.2020.00004

Exner, C. R. T. and Willsey, H. R. (2021). Xenopus leads the way: frogs as a pioneering model to understand the human brain. *Genesis* 59, e23405. doi:10.1002/dvg.23405

Faber, J. and Nieuwkoop, P. D. (2020). *Normal Table of Xenopus Laevis (Daudin): A Systematical & Chronological Survey of the Development from the Fertilized Egg till the End of Metamorphosis*. Garland Science.

Falk, T., Mai, D., Bensch, R., Çiçek, Ö., Abdulkadir, A., Marrakchi, Y., Böhm, A., Deubner, J., Jäckel, Z., Seiwald, K. et al. (2019). U-Net: deep learning for cell counting, detection, and morphometry. *Nat. Methods* 16, 67-70. doi:10.1038/s41592-018-0261-2

Gilbert, R. D., Sukhtankar, P., Lachlan, K. and Fowler, D. J. (2013). Bilineal inheritance of PKD1 abnormalities mimicking autosomal recessive polycystic disease. *Pediatr. Nephrol.* 28, 2217-2220. doi:10.1007/s00467-013-2484-x

Goda, T., Abu-Daya, A., Carruthers, S., Clark, M. D., Stemple, D. L. and Zimmerman, L. B. (2006). Genetic screens for mutations affecting development of xenopus tropicalis. *PLoS Genet.* 2, e91. doi:10.1371/journal.pgen.0020091

Gómez-de-Mariscal, E., García-López-de-Haro, C., Ouyang, W., Donati, L., Lundberg, E., Unser, M., Muñoz-Barrutia, A. and Sage, D. (2021). DeepImageJ: A user-friendly environment to run deep learning models in ImageJ. *Nat. Methods* 18, 1192-1195. doi:10.1038/s41592-021-01262-9

Graving, J. M., Chae, D., Naik, H., Li, L., Koger, B., Costelloe, B. R. and Couzin, I. D. (2019). DeepPoseKit, a software toolkit for fast and robust animal pose estimation using deep learning. *eLife* 8, e47994. doi:10.7554/eLife.47994

Günel, S., Rhodin, H., Morales, D., Campagnolo, J., Ramdya, P. and Fua, P. (2019). DeepFly3D, a deep learning-based approach for 3D limb and appendage tracking in tethered, adult *Drosophila*. *eLife* 8, e48571. doi:10.7554/eLife.48571

Hakim, A., Mor, Y., Toker, I. A., Levine, A., Neuhof, M., Markovitz, Y. and Rechavi, O. (2018). WorMachine: machine learning-based phenotypic analysis tool for worms. *BMC Biol.* 16, 8. doi:10.1186/s12915-017-0477-0

Hellsten, U., Harland, R. M., Gilchrist, M. J., Hendrix, D., Jurka, J., Kapitonov, V., Ovcharenko, I., Putnam, N. H., Shu, S., Taher, L. et al. (2010). The genome of the Western Clawed Frog Xenopus tropicalis. *Science* 328, 633-636. doi:10.1126/science.1183670

Hemmati-Brivanlou, A., Frank, D., Bolce, M. E., Brown, B. D., Sive, H. L. and Harland, R. M. (1990). Localization of specific mRNAs in Xenopus embryos by whole-mount in situ hybridization. *Development* 110, 325-330. doi:10.1242/dev.110.2.325

Hoff, S., Halbritter, J., Epting, D., Frank, V., Nguyen, T.-M. T., van Reeuwijk, J., Boehlke, C., Schell, C., Yasunaga, T., Helmstädter, M. et al. (2013). ANKS6 is a central component of a nephronophthisis module linking NEK8 to INVS and NPHP3. *Nat. Genet.* 45, 951-956. doi:10.1038/ng.2681

Huang, G., Liu, Z. and Weinberger, K. Q. (2017). Densely connected convolutional networks. *2017 IEEE Conference on Computer Vision and Pattern Recognition (CVPR)*, pp. 2261-2269.

Jinek, M., Chylinski, K., Fonfara, I., Hauer, M., Doudna, J. A. and Charpentier, E. (2012). A programmable dual-RNA–guided DNA endonuclease in adaptive bacterial immunity. *Science* 337, 816-821. doi:10.1126/science.1225829

Kälin, R. E., Bänziger-Tobler, N. E., Detmar, M. and Brändli, A. W. (2009). An in vivo chemical library screen in Xenopus tadpoles reveals novel pathways involved in angiogenesis and lymphangiogenesis. *Blood* 114, 1110-1122. doi:10.1182/blood-2009-03-211771

Kaminski, M. M., Tosic, J., Kresbach, C., Engel, H., Klockenbusch, J., Müller, A.-L., Pichler, R., Grahammer, F., Kretz, O., Huber, T. B. et al. (2016). Direct reprogramming of fibroblasts into renal tubular epithelial cells by defined transcription factors. *Nat. Cell Biol.* 18, 1269-1280. doi:10.1038/ncb3437

Kennedy, A. E. and Dickinson, A. J. G. (2012). Median facial clefts in Xenopus laevis: roles of retinoic acid signaling and homeobox genes. *Dev. Biol.* 365, 229-240. doi:10.1016/j.ydbio.2012.02.033

Kennedy, A. E. and Dickinson, A. J. (2014). Quantification of orofacial phenotypes in Xenopus. *J. Vis. Exp.* e52062. doi:10.3791/52062

Kingma, D. P. and Ba, J. (2014). Adam: a method for stochastic optimization. *ArXiv*, https://arxiv.org/abs/1412.6980.

Kirst, C., Skriabine, S., Vieites-Prado, A., Topilko, T., Bertin, P., Gerschenfeld, G., Verny, F., Topilko, P., Michalski, N., Tessier-Lavigne, M. et al. (2020). Mapping the fine-scale organization and plasticity of the brain vasculature. *Cell* 180, 780-795.e25. doi:10.1016/j.cell.2020.01.028

Kroll, F., Powell, G. T., Ghosh, M., Gestri, G., Antinucci, P., Hearn, T. J., Tunbak, H., Lim, S., Dennis, H. W., Fernandez, J. M. et al. (2021). A simple and effective F0 knockout method for rapid screening of behaviour and other complex phenotypes. *eLife* 10, e59683. doi:10.7554/eLife.59683

Kugler, E. C., Rampun, A., Chico, T. J. A. and Armitage, P. A. (2020). Segmentation of the zebrafish brain vasculature from light sheet fluorescence microscopy datasets. *bioRxiv* doi:10.1101/2020.07.21.213843

LeCun, Y., Bengio, Y. and Hinton, G. (2015). Deep learning. *Nature* 521, 436-444. doi:10.1038/nature14539

Lienkamp, S. S., Liu, K., Karner, C. M., Carroll, T. J., Ronneberger, O., Wallingford, J. B. and Walz, G. (2012). Vertebrate kidney tubules elongate using a planar cell polarity-dependent, rosette-based mechanism of convergent extension. *Nat. Genet.* 44, 1382-1387. doi:10.1038/ng.2452

Liu, Z. and Keller, P. J. (2016). Emerging imaging and genomic tools for developmental systems biology. *Dev. Cell* 36, 597-610. doi:10.1016/j.devcel.2016.02.016

Loffing, J., Vallon, V., Loffing-Cueni, D., Aregger, F., Richter, K., Pietri, L., Bloch-Faure, M., Hoenderop, J. G. J., Shull, G. E., Meneton, P. et al. (2004). Altered renal distal tubule structure and renal Na^+ and Ca^{2+} handling in a mouse model for Gitelman's syndrome. *J. Am. Soc. Nephrol.* 15, 2276-2288. doi:10.1097/01.ASN.0000138234.18569.63

Lu, W., Peissel, B., Babakhanlou, H., Pavlova, A., Geng, L., Fan, X., Larson, C., Brent, G. and Zhou, J. (1997). Perinatal lethality with kidney and pancreas defects in mice with a targetted Pkd1 mutation. *Nat. Genet.* 17, 179-181. doi:10.1038/ng1097-179

Mangos, S., Lam, P.-y., Zhao, A., Liu, Y., Mudumana, S., Vasilyev, A., Liu, A. and Drummond, I. A. (2010). The ADPKD genes pkd1a/b and pkd2 regulate extracellular matrix formation. *Dis. Model Mech.* 3, 354-365. doi:10.1242/dmm.003194

McNamara, S., Wlizla, M. and Horb, M. E. (2018). Husbandry, general care, and transportation of Xenopus laevis and Xenopus tropicalis. *Methods Mol. Biol.* 1865, 1-17. doi:10.1007/978-1-4939-8784-9_1

Menezes, L. F. and Germino, G. G. (2013). Murine models of polycystic kidney disease. *Drug Discov. Today Dis. Mech.* 10, e153-e158. doi:10.1016/j.ddmec.2013.10.002

Metzner, A., Griffiths, J. D., Streets, A. J., Markham, E., Philippou, T., Van Eeden, F. J. M. and Ong, A. C. M. (2020). A high throughput zebrafish chemical screen reveals ALK5 and non-canonical androgen signalling as modulators of the pkd2$^{-/-}$ phenotype. *Sci. Rep.* 10, 72. doi:10.1038/s41598-019-56995-7

Moreno-Mateos, M. A., Vejnar, C. E., Beaudoin, J.-D., Fernandez, J. P., Mis, E. K., Khokha, M. K. and Giraldez, A. J. (2015). CRISPRscan: designing highly efficient sgRNAs for CRISPR-Cas9 targeting in vivo. *Nat. Methods* 12, 982-988. doi:10.1038/nmeth.3543

Naert, T. and Vleminckx, K. (2018a). Methods for CRISPR/Cas9 Xenopus tropicalis tissue-specific multiplex genome engineering. *Methods Mol. Biol.* 1865, 33-54. doi:10.1007/978-1-4939-8784-9_3

Naert, T. and Vleminckx, K. (2018b). Genotyping of CRISPR/Cas9 genome edited xenopus tropicalis. *Methods Mol. Biol.* 1865, 67-82. doi:10.1007/978-1-4939-8784-9_5

Naert, T. and Vleminckx, K. (2018c). CRISPR/Cas9 disease models in zebrafish and Xenopus: the genetic renaissance of fish and frogs. *Drug Discov. Today Technol.* 28, 41-52. doi:10.1016/j.ddtec.2018.07.001

Naert, T., Colpaert, R., Van Nieuwenhuysen, T., Dimitrakopoulou, D., Leoen, J., Haustraete, J., Boel, A., Steyaert, W., Lepez, T., Deforce, D. et al. (2016). CRISPR/Cas9 mediated knockout of rb1 and rbl1 leads to rapid and penetrant retinoblastoma development in Xenopus tropicalis. *Sci. Rep.* 6, 35264. doi:10.1038/srep35264

Naert, T., Dimitrakopoulou, D., Tulkens, D., Demuynck, S., Carron, M., Noelanders, R., Eeckhout, L., Van Isterdael, G., Deforce, D., Vanhove, C. et al. (2020a). RBL1 (p107) functions as tumor suppressor in glioblastoma and small-cell pancreatic neuroendocrine carcinoma in Xenopus tropicalis. *Oncogene* 39, 2692-2706. doi:10.1038/s41388-020-1173-z

Naert, T., Tulkens, D., Edwards, N. A., Carron, M., Shaidani, N.-I., Wlizla, M., Boel, A., Demuynck, S., Horb, M. E., Coucke, P. et al. (2020b). Maximizing CRISPR/Cas9 phenotype penetrance applying predictive modeling of editing outcomes in Xenopus and zebrafish embryos. *Sci. Rep.* 10, 14662. doi:10.1038/s41598-020-71412-0

Nakayama, T., Fish, M. B., Fisher, M., Oomen Hajagos, J., Thomsen, G. H. and Grainger, R. M. (2013). Simple and efficient CRISPR/Cas9-mediated targeted mutagenesis in Xenopus tropicalis. *Genesis* 51, 835-843. doi:10.1002/dvg.22720

Nasr, T., Mancini, P., Rankin, S. A., Edwards, N. A., Agricola, Z. N., Kenny, A. P., Kinney, J. L., Daniels, K., Vardanyan, J., Han, L. et al. (2019). Endosome-mediated epithelial remodeling downstream of hedgehog-gli is required for tracheoesophageal separation. *Dev. Cell* 51, 665-674.e6. doi:10.1016/j.devcel.2019.11.003

Nauli, S. M., Alenghat, F. J., Luo, Y., Williams, E., Vassilev, P., Li, X., Elia, A. E. H., Lu, W., Brown, E. M., Quinn, S. J. et al. (2003). Polycystins 1 and 2

mediate mechanosensation in the primary cilium of kidney cells. *Nat. Genet.* **33**, 129-137. doi:10.1038/ng1076

Pan, C., Schoppe, O., Parra-Damas, A., Cai, R., Todorov, M. I., Gondi, G., von Neubeck, B., Böğürcü-Seidel, N., Seidel, S., Sleiman, K. et al. (2019). Deep learning reveals cancer metastasis and therapeutic antibody targeting in the entire body. *Cell* **179**, 1661-1676.e19. doi:10.1016/j.cell.2019.11.013

Raina, R., Madhavan, A. and Ng, A. Y. (2009). Large-scale deep unsupervised learning using graphics processors. In *Proceedings of the 26th Annual International Conference on Machine Learning*, pp. 873-880. New York, NY, USA: Association for Computing Machinery.

Reynaud, E. G., Peychl, J., Huisken, J. and Tomancak, P. (2015). Guide to light-sheet microscopy for adventurous biologists. *Nat. Methods* **12**, 30-34. doi:10.1038/nmeth.3222

Ronneberger, O., Fischer, P. and Brox, T. (2015). U-Net: convolutional networks for biomedical image segmentation. In *Medical Image Computing and Computer-Assisted Intervention – MICCAI 2015* (ed. N. Navab, J. Hornegger, W. M. Wells and A. F. Frangi), pp. 234-241. Cham: Springer International Publishing.

Royer, L. A., Weigert, M., Günther, U., Maghelli, N., Jug, F., Sbalzarini, I. F. and Myers, E. W. (2015). ClearVolume: open-source live 3D visualization for light-sheet microscopy. *Nat. Methods* **12**, 480-481. doi:10.1038/nmeth.3372

Ruf, R. G., Berkman, J., Wolf, M. T. F., Nurnberg, P., Gattas, M., Ruf, E.-M., Hyland, V., Kromberg, J., Glass, I., Macmillan, J. et al. (2003). A gene locus for branchio-otic syndrome maps to chromosome 14q21.3-q24.3. *J. Med. Genet* **40**, 515-519. doi:10.1136/jmg.40.7.515

Rumelhart, D. E., Hinton, G. E. and Williams, R. J. (1986). Learning representations by back-propagating errors. *Nature* **323**, 533-536. doi:10.1038/323533a0

Saberi-Bosari, S., Flores, K. B. and San-Miguel, A. (2020). Deep learning-enabled analysis reveals distinct neuronal phenotypes induced by aging and cold-shock. *BMC Biol.* **18**, 130. doi:10.1186/s12915-020-00861-w

Sanggaard, M., Rendtorff, N. D., Kjaer, K. W., Eiberg, H., Johnsen, T., Gimsing, S., Dyrmose, J., Nielsen, K. O., Lage, K. and Tranebjaerg, L. (2007). Branchio-oto-renal syndrome: detection of EYA1 and SIX1 mutations in five out of six Danish families by combining linkage. MLPA and sequencing analyses. *Eur. J. Hum. Genet.* **15**, 1121-1131. doi:10.1038/sj.ejhg.5201900

Satterstrom, F. K., Kosmicki, J. A., Wang, J., Breen, M. S., De Rubeis, S., An, J.-Y., Peng, M., Collins, R., Grove, J., Klei, L. et al. (2020). Large-scale exome sequencing study implicates both developmental and functional changes in the neurobiology of autism. *Cell* **180**, 568-584.e23. doi:10.1016/j.cell.2019.12.036

Schindelin, J., Arganda-Carreras, I., Frise, E., Kaynig, V., Longair, M., Pietzsch, T., Preibisch, S., Rueden, C., Saalfeld, S., Schmid, B. et al. (2012). Fiji: an open-source platform for biological-image analysis. *Nat. Methods* **9**, 676-682. doi:10.1038/nmeth.2019

Schmidt, U., Weigert, M., Broaddus, C. and Myers, G. (2018). Cell detection with star-convex polygons. In *Medical Image Computing and Computer Assisted Intervention - MICCAI 2018* (ed. A. F. Frangi, J. A. Schnabel, C. Davatzikos, C. Alberola-López and G. Fichtinger), pp. 265-273. Springer.

Schnoz, C., Moser, S., Kratschmar, D. V., Odermatt, A., Loffing-Cueni, D. and Loffing, J. (2021). Deletion of the transcription factor Prox-1 specifically in the renal distal convoluted tubule causes hypomagnesemia via reduced expression of TRPM6 and NCC. *Pflugers Arch.* **473**, 79-93. doi:10.1007/s00424-020-02491-1

Schottenfeld, J., Sullivan-Brown, J. and Burdine, R. D. (2007). Zebrafish curly up encodes a Pkd2 ortholog that restricts left-side-specific expression of southpaw. *Development* **134**, 1605-1615. doi:10.1242/dev.02827

Shaidani, N.-I., McNamara, S., Wlizla, M. and Horb, M. E. (2020). Animal maintenance systems: xenopus tropicalis. *Cold Spring Harb. Protoc.* **2020**, pdb.prot106146. doi:10.1101/pdb.prot106146

Shaidani, N.-I., McNamara, S., Wlizla, M. and Horb, M. E. (2021a). Obtaining Xenopus laevis embryos. *Cold Spring Harb. Protoc* **2021**, pdb.prot106211. doi:10.1101/pdb.prot106211

Shaidani, N.-I., McNamara, S., Wlizla, M. and Horb, M. E. (2021b). Obtaining Xenopus laevis eggs. *Cold Spring Harb. Protoc.* **2021**, pdb.prot106203. doi:10.1101/pdb.prot106203

Stringer, C., Wang, T., Michaelos, M. and Pachitariu, M. (2021). Cellpose: a generalist algorithm for cellular segmentation. *Nat. Methods* **18**, 100-106. doi:10.1038/s41592-020-01018-x

Szenker-Ravi, E., Altunoglu, U., Leushacke, M., Bosso-Lefèvre, C., Khatoo, M., Thi Tran, H., Naert, T., Noelanders, R., Hajamohideen, A., Beneteau, C. et al. (2018). RSPO2 inhibition of RNF43 and ZNRF3 governs limb development independently of LGR4/5/6. *Nature* **557**, 564-569. doi:10.1038/s41586-018-0118-y

Tavares, A. L. P., Jourdeuil, K., Neilson, K. M., Majumdar, H. D. and Moody, S. A. (2021). Sobp modulates the transcriptional activation of Six1 target genes and is required during craniofacial development. *Development* **148**, dev199684. doi:10.1242/dev.199684

Todorov, M. I., Paetzold, J. C., Schoppe, O., Tetteh, G., Shit, S., Efremov, V., Todorov-Völgyi, K., Düring, M., Dichgans, M., Piraud, M. et al. (2020). Machine learning analysis of whole mouse brain vasculature. *Nat. Methods* **17**, 442-449. doi:10.1038/s41592-020-0792-1

Tomer, R., Ye, L., Hsueh, B. and Deisseroth, K. (2014). Advanced CLARITY for rapid and high-resolution imaging of intact tissues. *Nat. Protoc.* **9**, 1682-1697. doi:10.1038/nprot.2014.123

Tomlinson, M. L., Rejzek, M., Fidock, M., Field, R. A. and Wheeler, G. N. (2009). Chemical genomics identifies compounds affecting Xenopus laevis pigment cell development. *Mol. Biosyst.* **5**, 376-384. doi:10.1039/b818695b

van der Walt, S., Schönberger, J. L., Nunez-Iglesias, J., Boulogne, F., Warner, J. D., Yager, N., Gouillart, E. and Yu, T. (2014). scikit-image: image processing in Python. *PeerJ* **2**, e453. doi:10.7717/peerj.453

VanderPlas, J., Granger, B., Heer, J., Moritz, D., Wongsuphasawat, K., Satyanarayan, A., Lees, E., Timofeev, I., Welsh, B. and Sievert, S. (2018). Altair: interactive statistical visualizations for python. *J. Open Source Softw.* **3**, 1057. doi:10.21105/joss.01057

Villoutreix, P. (2021). What machine learning can do for developmental biology. *Development* **148**, dev188474. doi:10.1242/dev.188474

Vivante, A., Kleppa, M.-J., Schulz, J., Kohl, S., Sharma, A., Chen, J., Shril, S., Hwang, D.-Y., Weiss, A.-C., Kaminski, M. M. et al. (2015). Mutations in TBX18 cause dominant urinary tract malformations via transcriptional dysregulation of ureter development. *Am. J. Hum. Genet.* **97**, 291-301. doi:10.1016/j.ajhg.2015.07.001

Vize, P. D., McCoy, K. E. and Zhou, X. (2009). Multichannel wholemount fluorescent and fluorescent/chromogenic in situ hybridization in Xenopus embryos. *Nat. Protoc.* **4**, 975-983. doi:10.1038/nprot.2009.69

Voigt, F. F., Kirschenbaum, D., Platonova, E., Pagès, S., Campbell, R. A. A., Kastli, R., Schaettin, M., Egolf, L., van der Bourg, A., Bethge, P. et al. (2019). The mesoSPIM initiative: open-source light-sheet microscopes for imaging cleared tissue. *Nat. Methods* **16**, 1105-1108. doi:10.1038/s41592-019-0554-0

von Chamier, L., Laine, R. F., Jukkala, J., Spahn, C., Krentzel, D., Nehme, E., Lerche, M., Hernández-Pérez, S., Mattila, P. K., Karinou, E. et al. (2021). Democratising deep learning for microscopy with ZeroCostDL4Mic. *Nat. Commun.* **12**, 2276. doi:10.1038/s41467-021-22518-0

Wallingford, J. B. (2019). We are all developmental biologists. *Dev. Cell* **50**, 132-137. doi:10.1016/j.devcel.2019.07.006

Wang, F., Shi, Z., Cui, Y., Guo, X., Shi, Y.-B. and Chen, Y. (2015). Targeted gene disruption in Xenopus laevis using CRISPR/Cas9. *Cell Biosci.* **5**, 15. doi:10.1186/s13578-015-0006-1

Waskom, M. (2021). seaborn: statistical data visualization. *J. Open Source Softw.* **6**, 3021. doi:10.21105/joss.03021

Wen, C., Miura, T., Voleti, V., Yamaguchi, K., Tsutsumi, M., Yamamoto, K., Otomo, K., Fujie, Y., Teramoto, T., Ishihara, T. et al. (2021). 3DeeCellTracker, a deep learning-based pipeline for segmenting and tracking cells in 3D time lapse images. *eLife* **10**, e59187. doi:10.7554/eLife.59187

Willsey, H. R., Walentek, P., Exner, C. R. T., Xu, Y., Lane, A. B., Harland, R. M., Heald, R. and Santama, N. (2018). Katanin-like protein Katnal2 is required for ciliogenesis and brain development in Xenopus embryos. *Dev. Biol.* **442**, 276-287. doi:10.1016/j.ydbio.2018.08.002

Willsey, H. R., Xu, Y., Everitt, A., Dea, J., Exner, C. R. T., Willsey, A. J., State, M. W. and Harland, R. M. (2020). The neurodevelopmental disorder risk gene DYRK1A is required for ciliogenesis and control of brain size in Xenopus embryos. *Development* **147**, dev189290. doi:10.1242/dev.189290

Willsey, H. R., Exner, C. R. T., Xu, Y., Everitt, A., Sun, N., Wang, B., Dea, J., Schmunk, G., Zaltsman, Y., Teerikorpi, N. et al. (2021). Parallel in vivo analysis of large-effect autism genes implicates cortical neurogenesis and estrogen in risk and resilience. *Neuron* **109**, 788-804.e8. doi:10.1016/j.neuron.2021.01.002

Yang, B., Treweek, J. B., Kulkarni, R. P., Deverman, B. E., Chen, C.-K., Lubeck, E., Shah, S., Cai, L. and Gradinaru, V. (2014). Single-cell phenotyping within transparent intact tissue through whole-body clearing. *Cell* **158**, 945-958. doi:10.1016/j.cell.2014.07.017

Zhang, B., Pas, K. E., Ijaseun, T., Cao, H., Fei, P. and Lee, J. (2021). Automatic segmentation and cardiac mechanics analysis of evolving zebrafish using deep learning. *Front. Cardiovasc. Med.* **8**, 675291. doi:10.3389/fcvm.2021.675291

Zhao, S., Todorov, M. I., Cai, R., Maskari, R. A., Steinke, H., Kemter, E., Mai, H., Rong, Z., Warmer, M., Stanic, K. et al. (2020). Cellular and molecular probing of intact human organs. *Cell* **180**, 796-812.e19. doi:10.1016/j.cell.2020.01.030
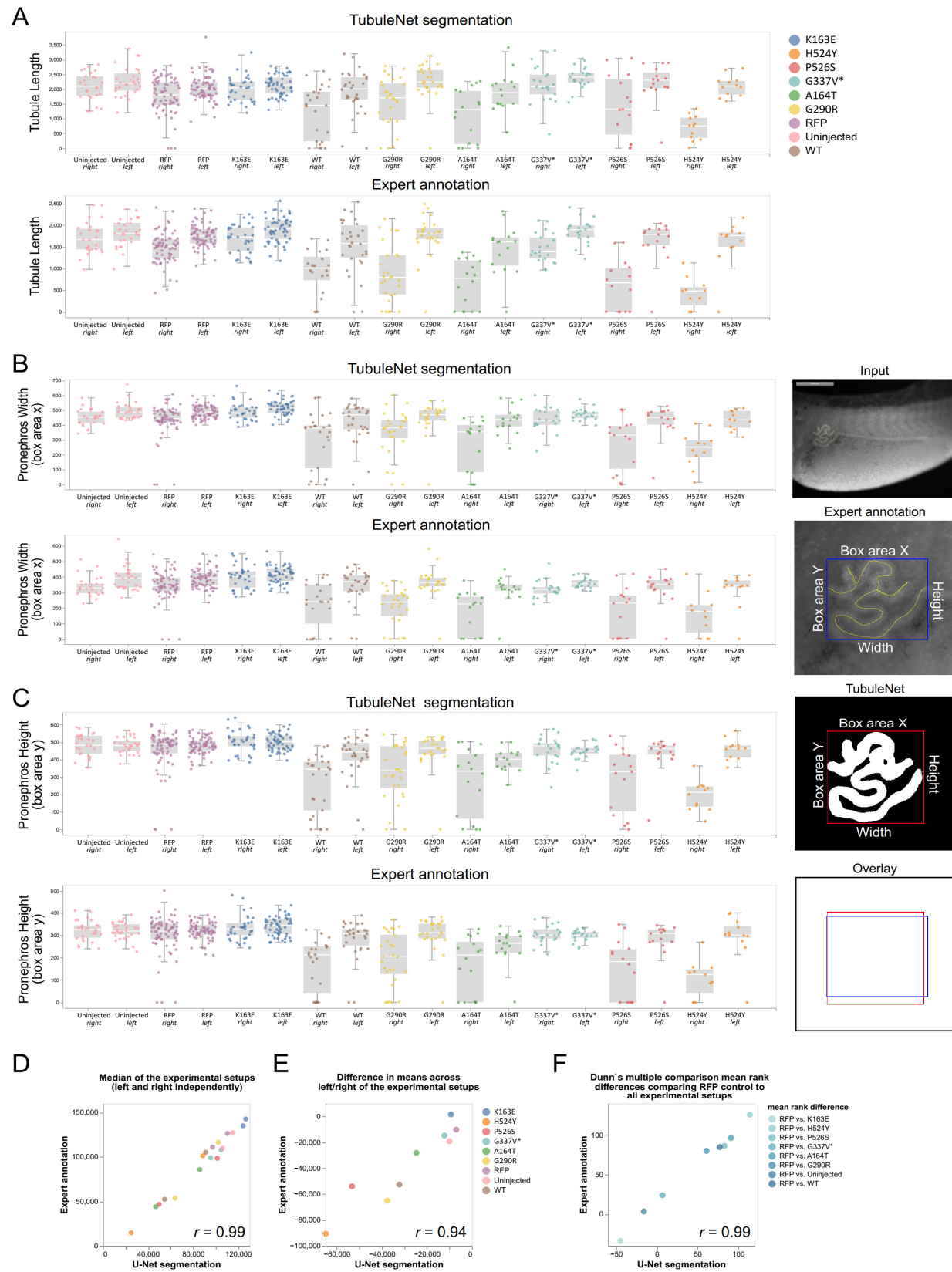
Fig. S1. TubuleNet segmentations closely copied expert human annotations. (A-C) TubuleNet and expert annotations for tubule length, pronephros width (bounding box area x) and pronephros height (box area y). Shown on the right is raw input data as used. Crop outs reflect the manual segmentation and TubuleNet segmentations. Deviations in pronephros height and width when directly comparing the measurements between manual segmentation and TubuleNet due to differential methodology of applying the bounding box are apparent. **(D)** Correlation of the median value of the pronephros area between TubuleNet and U-net segmentations across each setup (left and right pronephros separately) (n = 18) (pearson r = 0.99). **(E)** Correlation of the difference in means across the left/right pronephros across each setup (n = 9) (pearson r = 0.94). **(F)** For eight setups the Dunn's multiple comparison mean rank difference was calculated to an RFP injection control. This was performed for both TubuleNet measurements and expert annotations. Matched mean rank differences for identical comparisons were compared between TubuleNet and expert annotations revealing profound correlation (n = 9) (pearson r = 0.99).
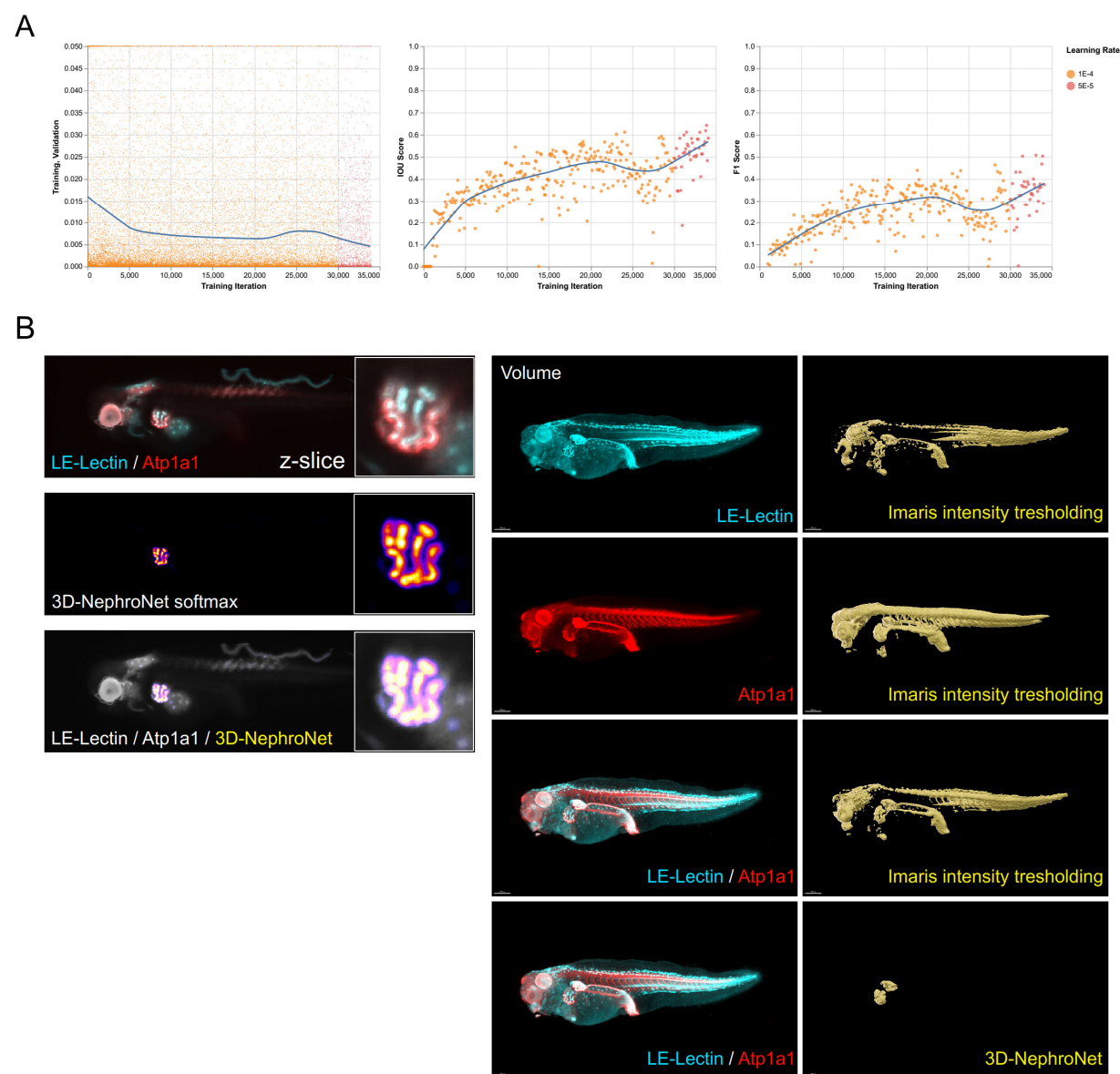
Fig. S2. 3D-NephroNet. (A) U-Net training logs. Blue lines (left to right) are locally estimated scatterplot smoothing (LOESS) of validation loss**. (B)** Comparison between Imaris intensity threshold segmentation (threshold level increased until full segmentation of the left kidney was achieved) and 3D-NephroNet. Threshold segmentation was performed on the single LEL-lectin channel, the single Atp1a1 channel and the LEL-lectin/ Atp1a1 composite. 3D-NephroNet was run on the LEL-lectin/Atp1a1 composite. A largest-two blob filter was applied on the 3D-NephroNet segmentation. This embryo is unseen test data.
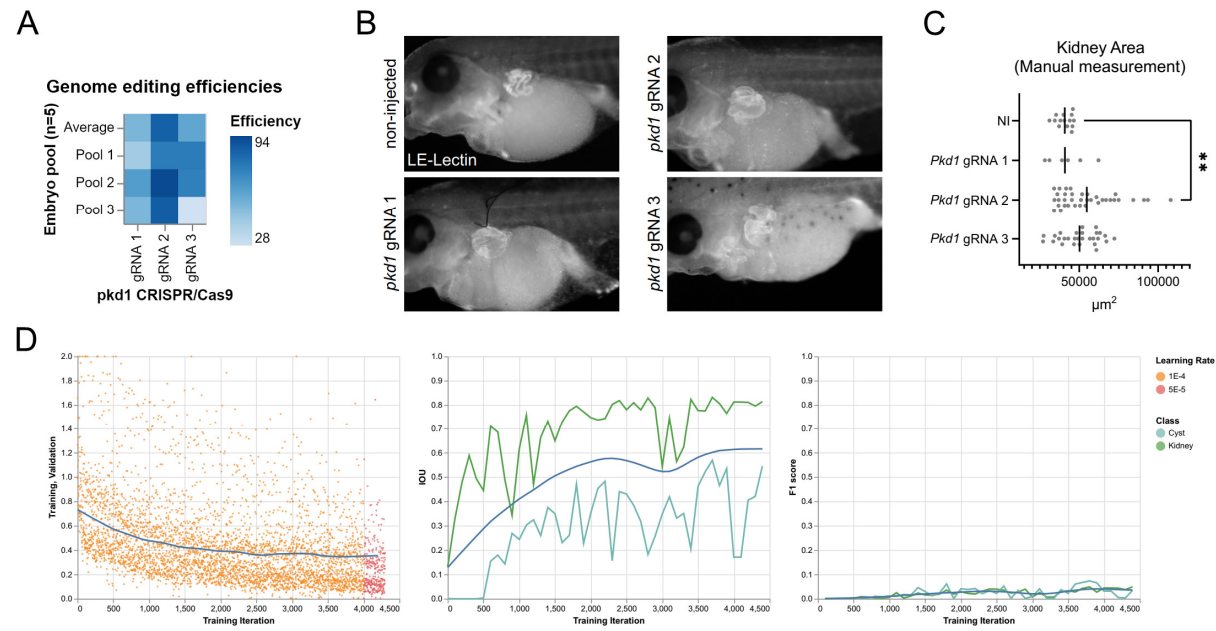
Fig. S3. Efficient genome editing of *pkd1* results in cystogenesis in *X. tropicalis* embryos. (A) Genome editing efficiencies for three distinct gRNAs targeting *pkd1* as quantified by Sanger sequencing and trace deconvolution approaches (3 pools of 5 embryos per gRNA, *N* = 15). **(B)** Development of cystic kidneys in *X. tropicalis* embryos after bilateral injection of *pkd1* gRNAs in two-cell embryos. **(C)** Kidney areas were manually measured revealing only for *pkd1* gRNA 2 a significant increase. (Kruskal-Wallis: *p*<0.05; Dunn's multiple comparisons: * *p*<0.05) **(D)** U-Net training logs for 3D-CystNet. Blue lines (left to right) are LOESS of validation loss, IOU across classes and F1 score across classes
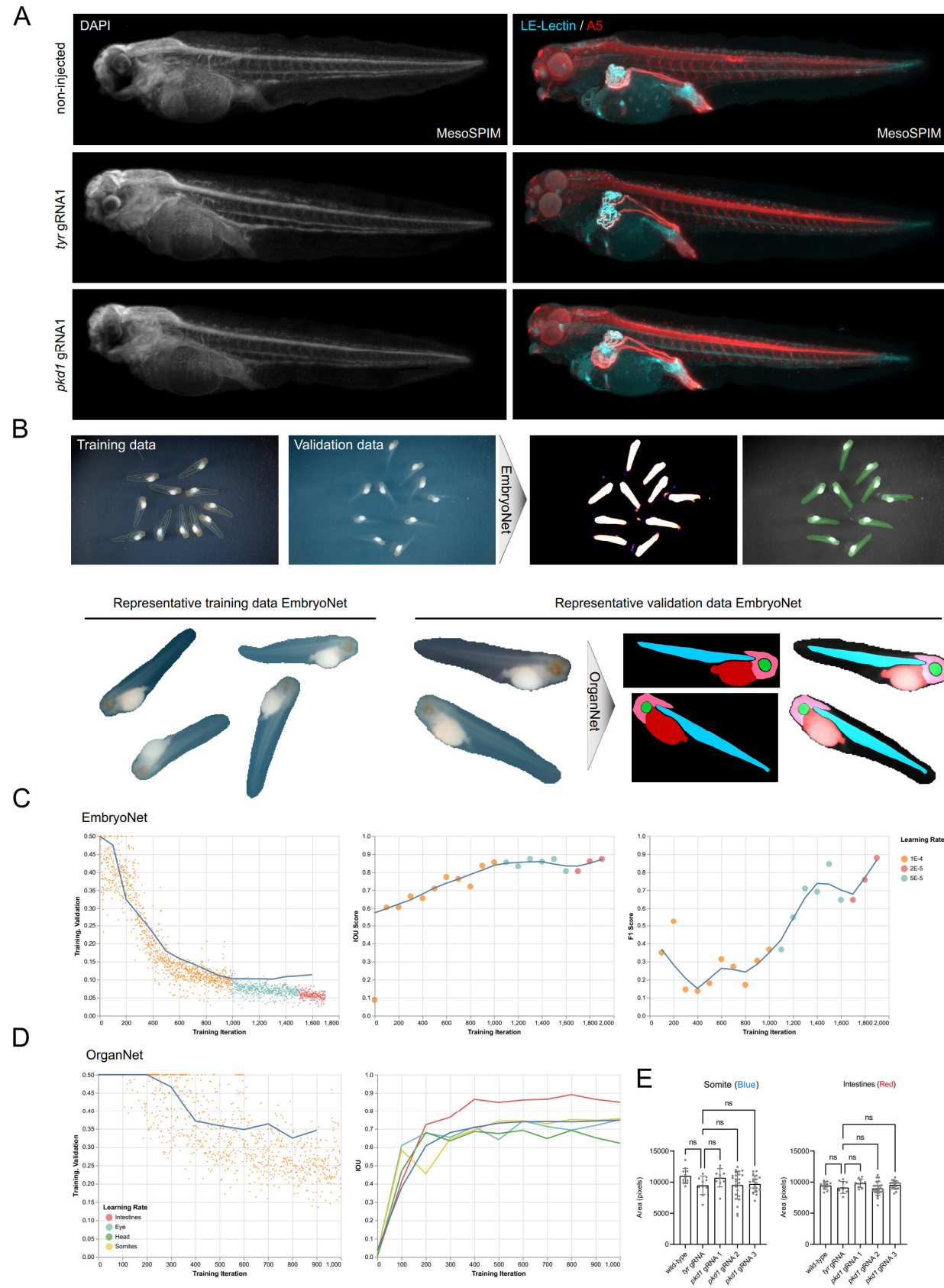
Fig. S4. *pkd1* crispants do not show gross morphological abnormalities. (A) mesoSPIM recordings in the DAPI channel reveal no gross differences in embryos between non-injected, *tyr* crispants and *pkd1* gRNA crispants. Nevertheless, obvious kidney cystogenesis can be observed in the LE/Lectin-A5 channels. **(B)** A chained U-Net approach to investigate possible broad abnormalities in structures originating from the vegetal-ventral blastomere. First, an Embryonet (IOU: 0.87) is used to isolate embryos from low magnification bright-field stereomicroscopy. Isolated single embryos are then processed by OrganNet (IOU: 0.75) to provide area measurements of 4 anatomical regions: The head (pink), the somites (blue), the eye (green) and then intestines (red). **(C-D)** U-Net training logs for EmbryoNet and OrganNet. Blue lines (left to right) are LOESS of validation loss, IOU across classes and F1 score across classes. **(E)** Fully automated measurements using a Fiji macro chaining EmbryoNet and OrganNet allows extraction of somite and intestine area of single embryos from low-magnification stereomicroscopy. This reveals no significant differences in sizes of two anatomical structures, originating from the CRISPR/Cas9-targeted ventral-vegetal lineage, when comparing non-injected, *tyr* injected and *pkd1* injected embryos demonstrating absence of gross abnormalities in *pkd1* crispants.
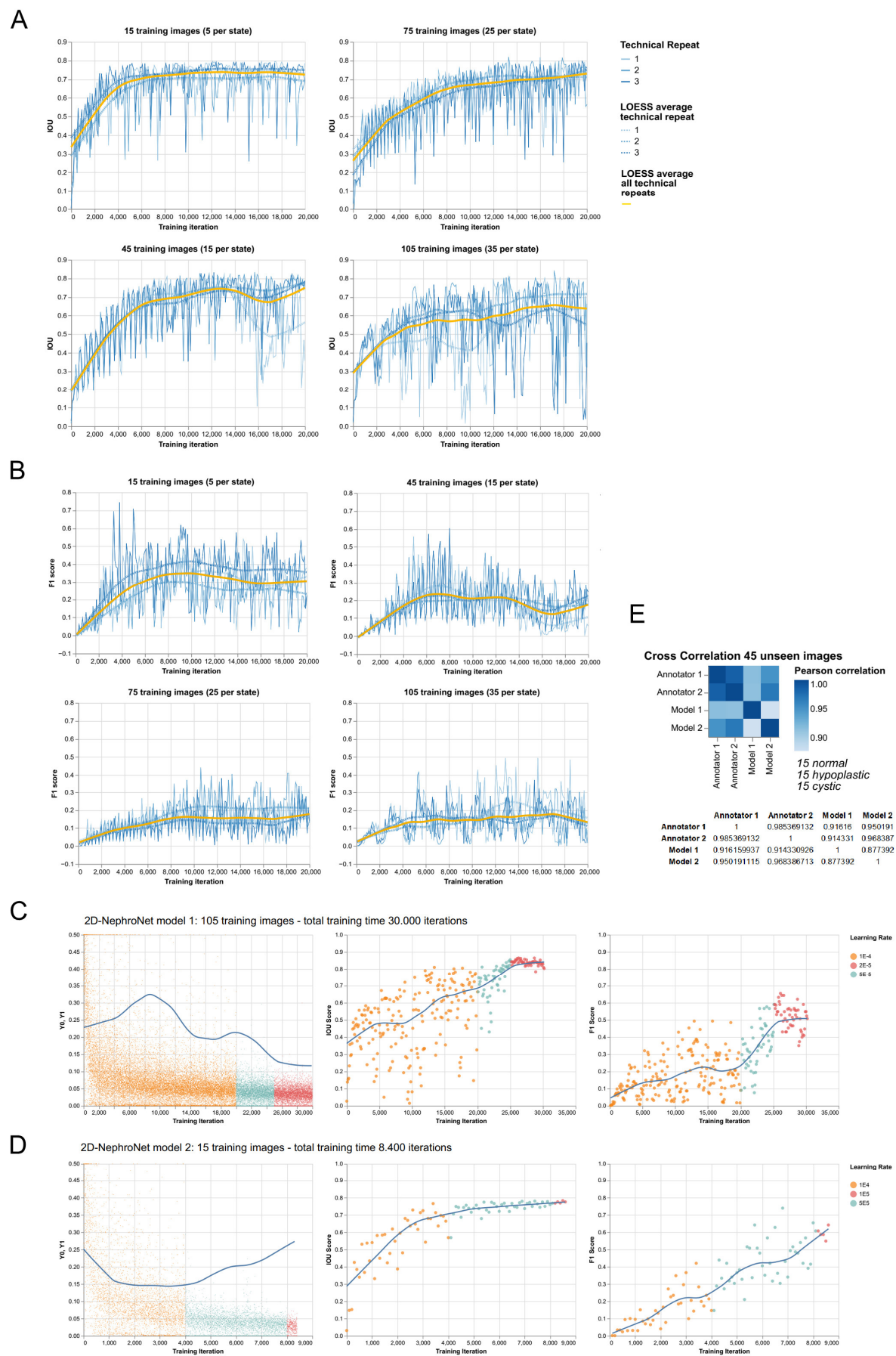
Fig. S5. 2D-NephroNet, a deep learning solution for kidney segmentation in *X. tropicalis* embryos. (A-B) U-Net training logs: IOU and F1 scores across different training dataset sizes (5, 15, 25 and 35 per state). State is defined as either hypoplastic, normal or cystic *X. tropicalis* kidneys. Orange line is the LOESS of the three technical repeats, dashed lines are the LOESS of each technical repeat separately. **(C-D)** U-Net training logs: 2D-NephroNet models trained with a larger training dataset for more iterations and with a smaller dataset for less iterations. **(E)** Cross-correlation of model 1 (*panel C*) and model 2 (*panel D*) to two independent human experts using 45 unseen test images, stratified evenly across the three states.
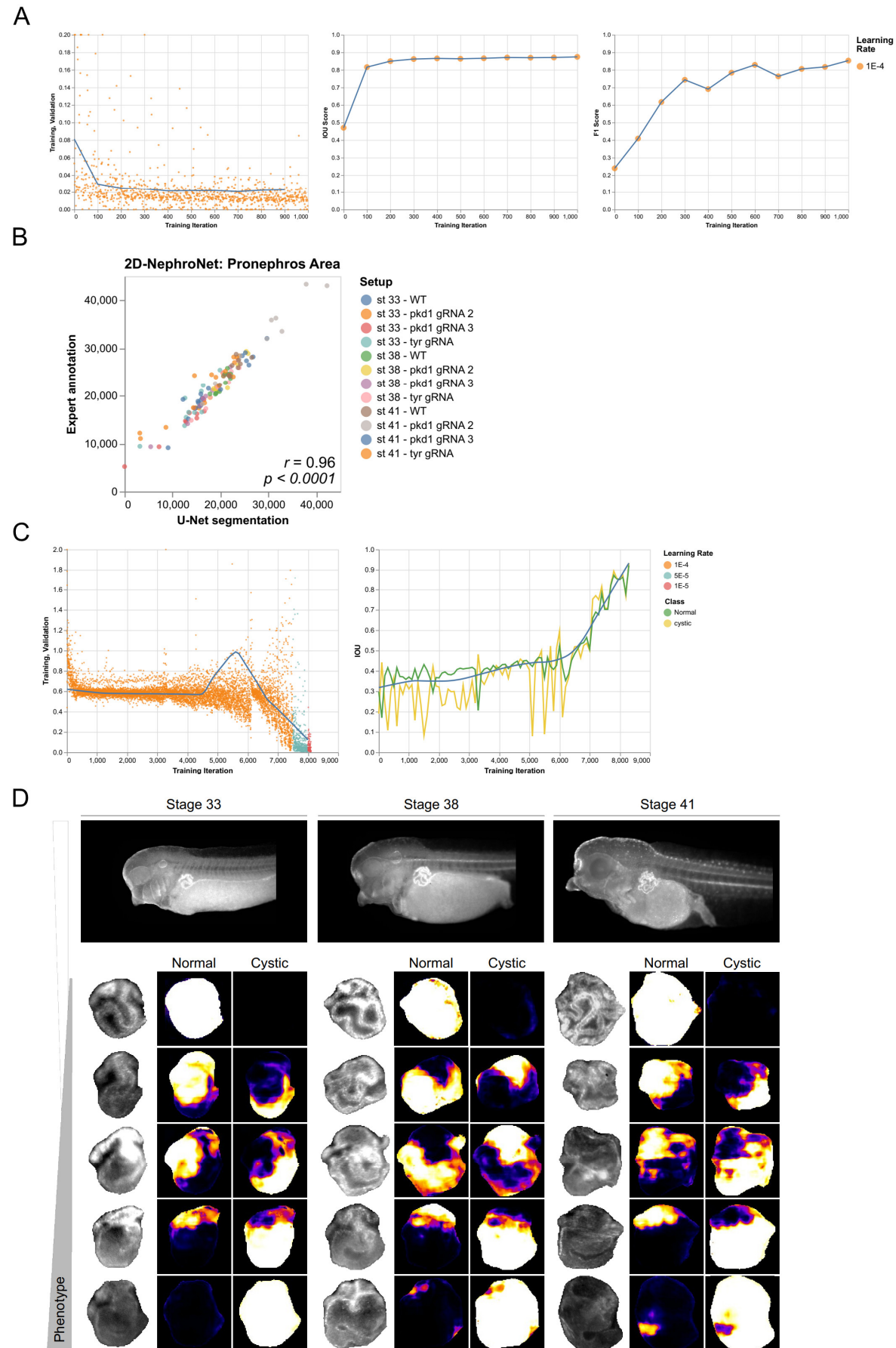
A

B

2D-NephroNet: Pronephros Area

Setup
- st 33 - WT
- st 33 - pkd1 gRNA 2
- st 33 - pkd1 gRNA 3
- st 33 - tyr gRNA
- st 38 - WT
- st 38 - pkd1 gRNA 2
- st 38 - pkd1 gRNA 3
- st 38 - tyr gRNA
- st 41 - WT
- st 41 - pkd1 gRNA 2
- st 41 - pkd1 gRNA 3
- st 41 - tyr gRNA

$r = 0.96$
$p < 0.0001$

C

Learning Rate
- 1E-4
- 5E-5
- 1E-5

Class
- Normal
- cystic

D

Fig. S6. 2D-NephroNet transfer learning and 2D-CystNet. (A) Transfer learning finetuning adapting a pre-trained 2D-NephroNet towards different imaging conditions (different stereomicroscope and different zoom level used). Blue lines (left to right) are LOESS of validation loss, IOU across classes and F1 score across classes **(B)** U-Net training logs 2D-CystNet. **(C)** 2D-CystNet performance across the phenotypic scale and across three developmental stages. **(D)** Correlation of the pronephros area between 2D-NephroNet and expert annotations ($n = 120$) (pearson $r = 0.96$). All data used for this correlation was unseen to the network and the expert annotator was not involved in labeling the training data.
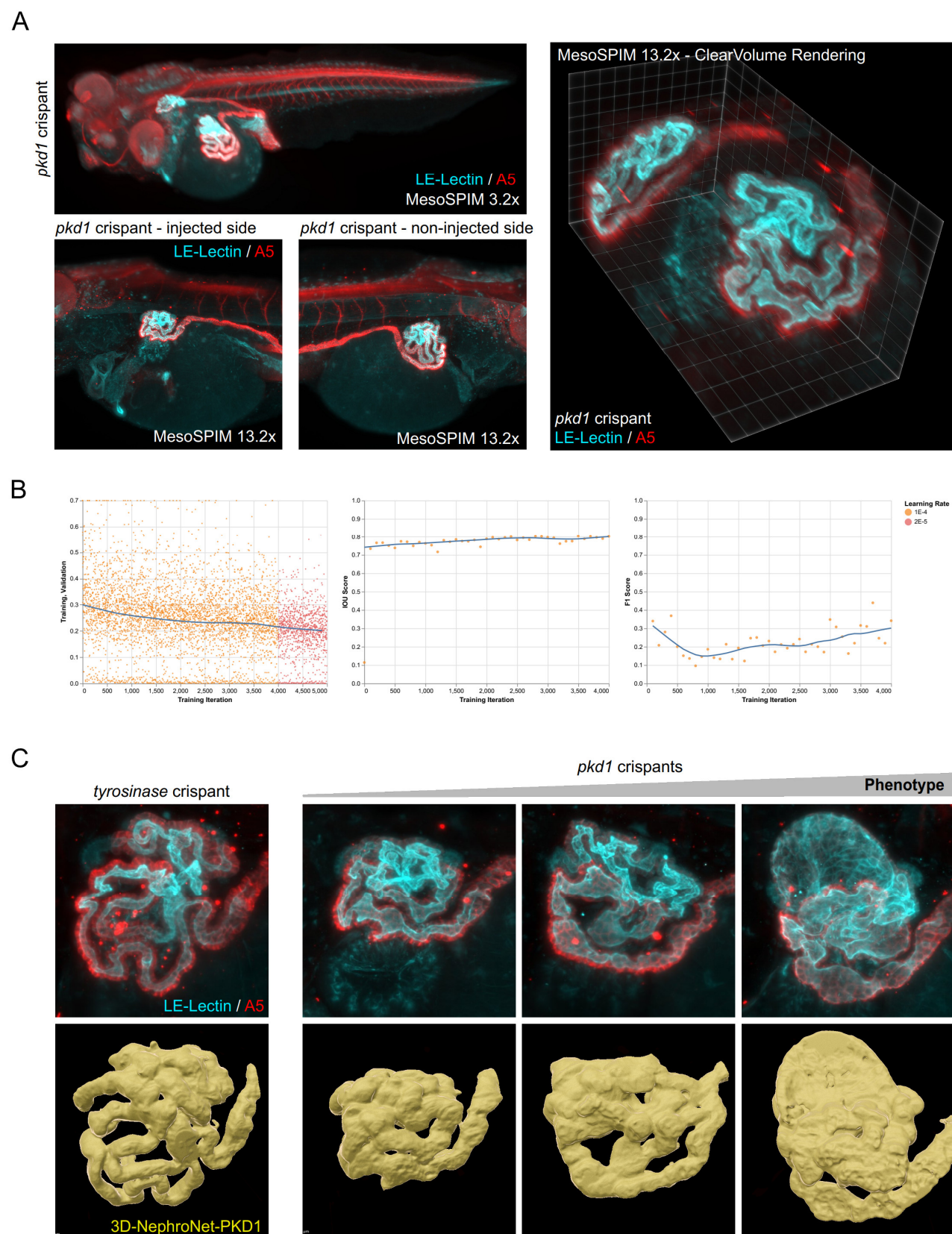
Fig. S7. High-resolution mesoSPIM (using MVPLAPO2XC objective) reveals localized tubular cysts interspersed with undilated epithelia in *pkd1* crispants. (A) mesoSPIM imaging with a 2x objective clearly showcases local cystogenesis in *pkd1* crispants. **(B)** U-Net training logs for 3D-NephroNet-PKD1. Blue lines (left to right) are LOESS of validation loss, IOU and F1 score. **(C)** 3D-NephroNet-PKD1 for 3D reconstruction of kidneys from high-resolution mesoSPIM data (acquired with 2x objective) showcasing the spectrum of phenotypes occurring in *pkd1* crispants.
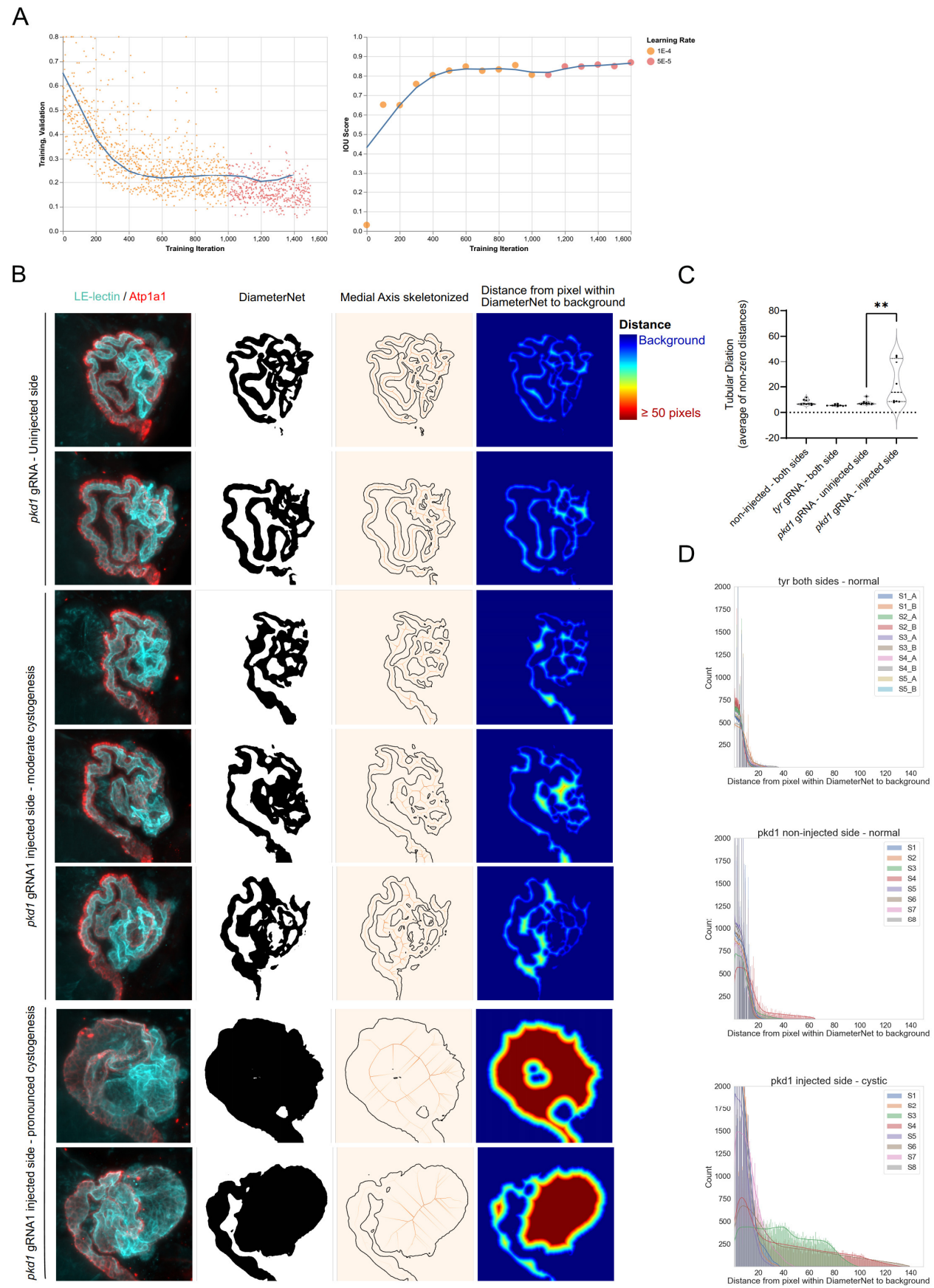
Fig. S8. Cystogenesis in *pkd1* crispants is characterized by a phenotypic spectrum ranging from tubular cysts interspersed with undilated epithelia to fully cystic kidneys, reflecting the mosaic nature of CRISPR/ Cas9 genome editing. (A) U-Net training logs for DiameterNet. Blue lines (left to right) are LOESS of validation loss, IOU across classes and F1 score across classes **(B)** DiameterNet was deployed on maximum projections of single kidneys imaged using high-resolution MesoSPIM. The resulting segmentation map was employed for medial axis skeletonization allowing heatmapping of the distance between each pixel within the DiameterNet mask to background pixels with the value zero **(C)** Significant increase in the average tubular dilation comparing the kidneys on the injected side of *pkd1* crispants to kidneys on the non-injected side. Tubular dilation is an index calculated as the average of each non-zero pixel in the heatmap shown in C. Mann-Whitney test, **$p<0.01$. **(D)** Histogram plots demonstrating the increase in distance from pixels within DiameterNet to background, a measure for tubular dilation around that pixel, when comparing the injected side of *pkd1* crispants to either the non-injected side or both sides of *tyrosinase* control crispants.
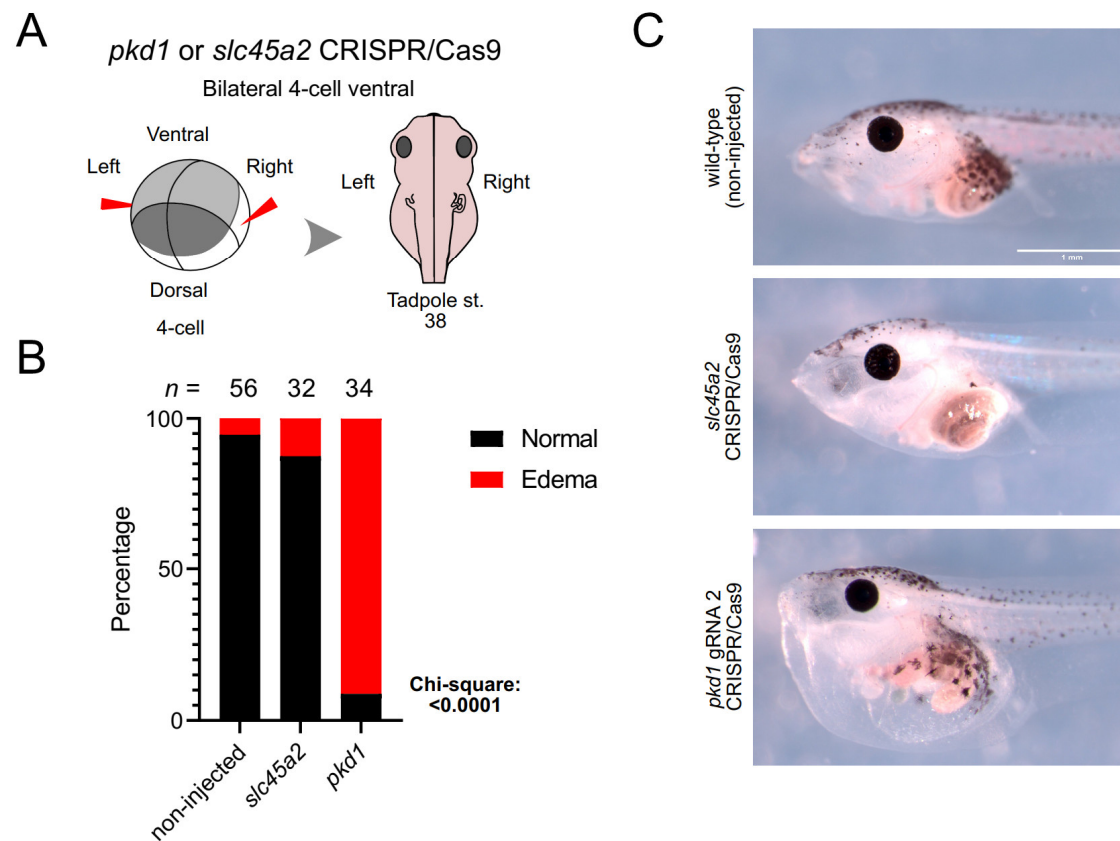
Fig. S9. Generalized edema can be triggered in *pkd1* crispants at stage 45 by targeting both kidneys. (A) Targeting both the left and the right ventral blastomere allows bilateral gene editing using *pkd1* gRNA2. **(B-C)** When both kidneys are targeted pronounced general edema occurs, showcasing a functional consequence of renal malfunction and fluid retention in early development.
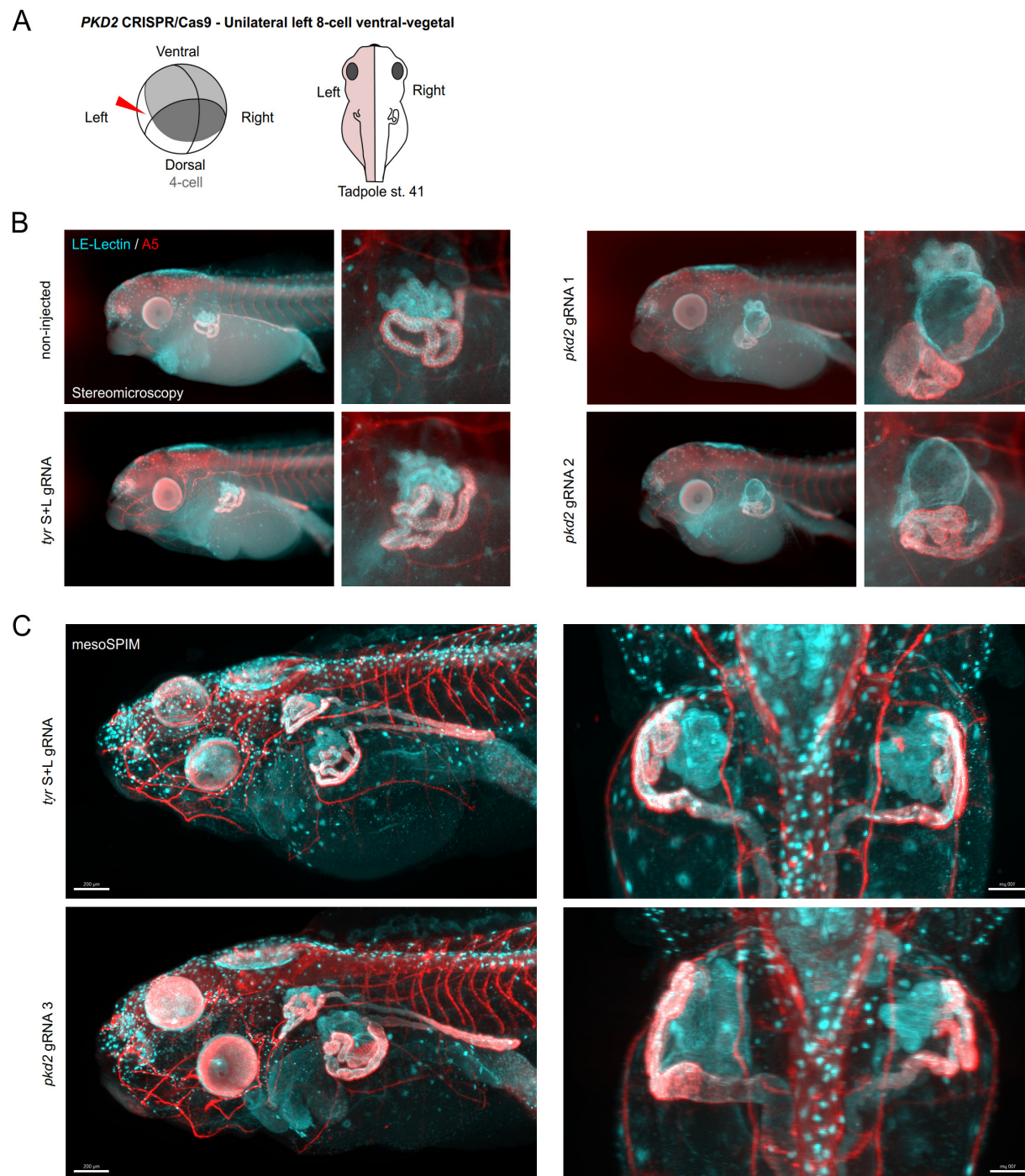
Fig. S10. ***pkd2* crispant model for autosomal dominant polycystic kidney disease (ADPKD). (A)** Schematic of CRISPR/Cas9 injection in the vegetal-ventral blastomere of an 8-cell stage in *X. laevis* embryos. **(B)** Stereomicroscopy of LE-Lectin/A5 stained embryos reveals normal kidney development in non-injected and tyrosinase control embryos. Injections of two independent gRNAs targeting *pkd2*, existing as a non-duplicated gene on the *X. laevis* L. chromosome, leads to localized renal cyst formation. **(C)** mesoSPIM light-sheet microscopy revealing cystogenesis on the injected (left) side of *pkd2* crispants, which is absent on the non-injected (right) side or in *tyr* crispant controls.
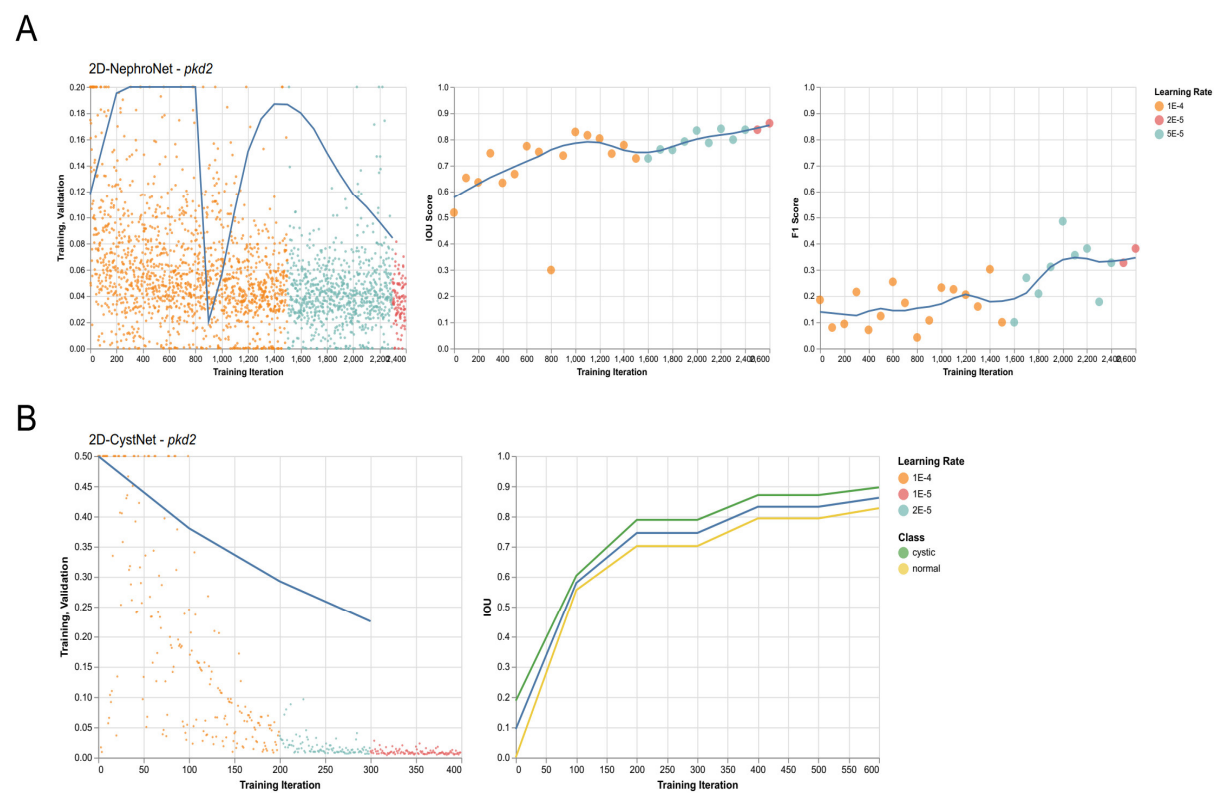
Fig. S11. 2D-NephroNet and 2D-CystNet transfer learning. (A) Transfer learning finetuning adapting a pre-trained 2D-NephroNet towards towards *pkd2 X. laevis* embryos. Blue lines (left to right) are LOESS of validation loss, IOU across classes and F1 score across classes **(B)** Transfer learning finetuning adapting a pre-trained 2D-CystNet towards towards *pkd2 X. laevis* embryos.

A

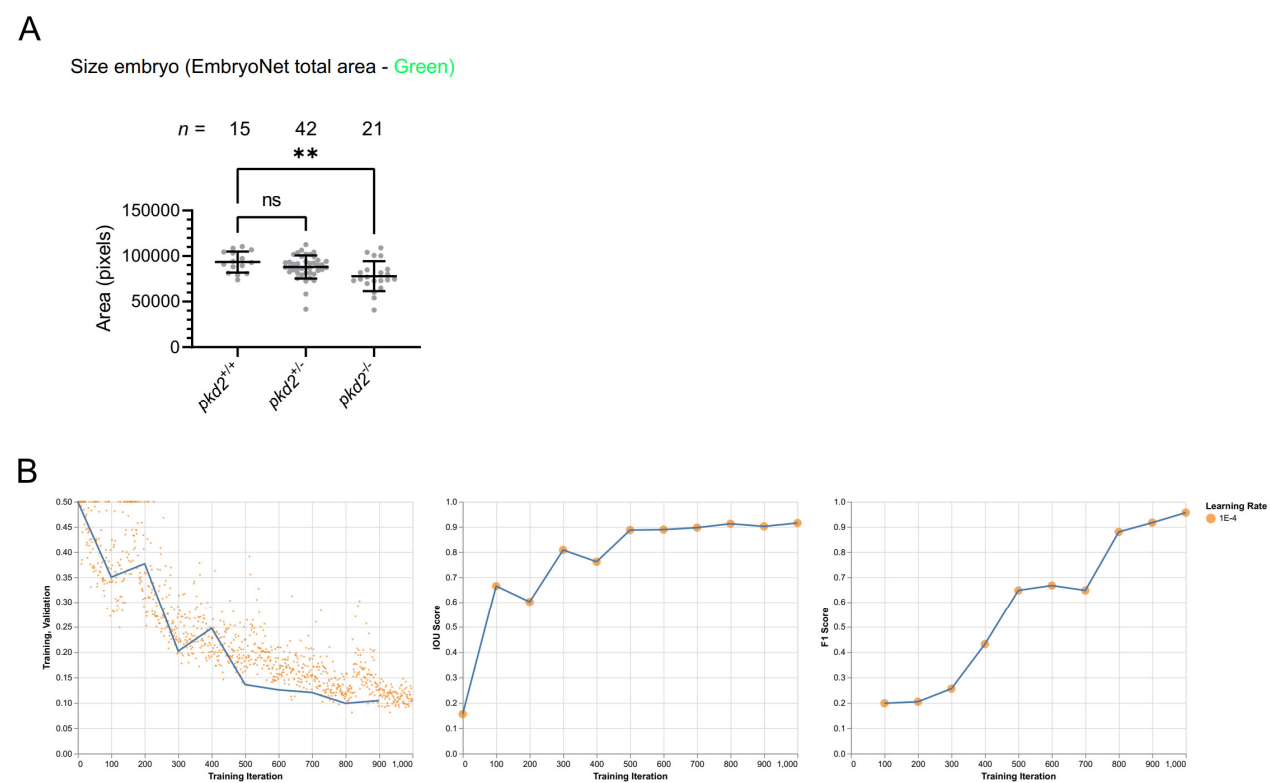Size embryo (EmbryoNet total area - Green)

B

Fig. S12. Analysis of *pkd2* mutants. (A) Fully automated measurements reveal significant differences in embryo size (EmbryoNet total area) (Analysis shown in detail in main figure 3D. (**B**) EmbryoNet-PKD2 training logs. Blue lines (left to right) are LOESS of validation loss, IOU and F1 score.
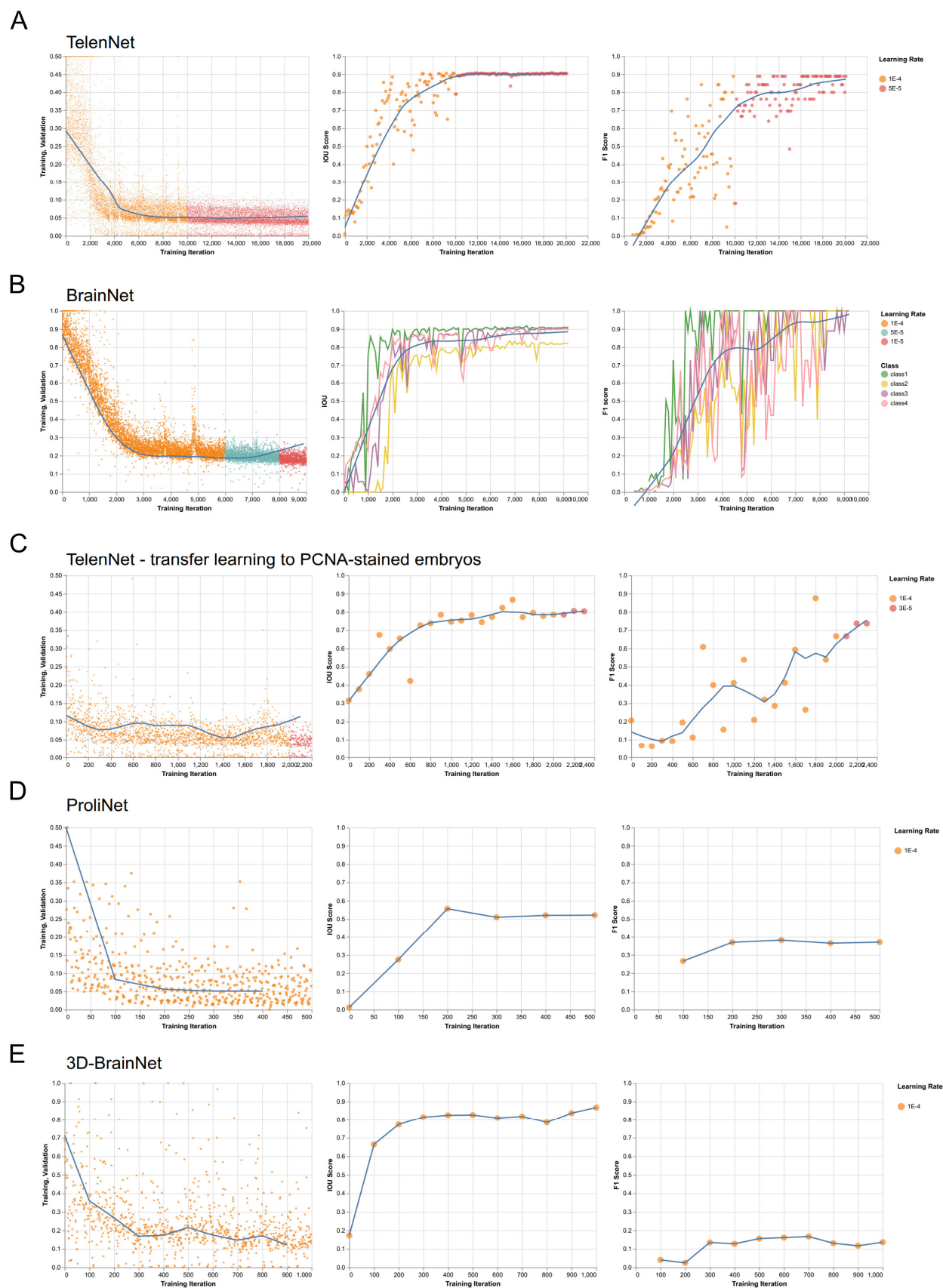
Fig. S13. U-Net deep learning for brain phenotyping. (A) TelenNet training logs. Blue lines (left to right) are LOESS of validation loss, IOU and F1 score. **(B)** BrainNet training logs. Blue lines (left to right) are LOESS of validation loss, IOU across classes and F1 score across classes. **(C)** TelenNet transfer learning to PCNA-stained embryos training logs. Blue lines (left to right) are LOESS of validation loss, IOU and F1 score. **(D)** ProliNet training logs. Blue lines (left to right) are LOESS of validation loss, IOU and F1 score.
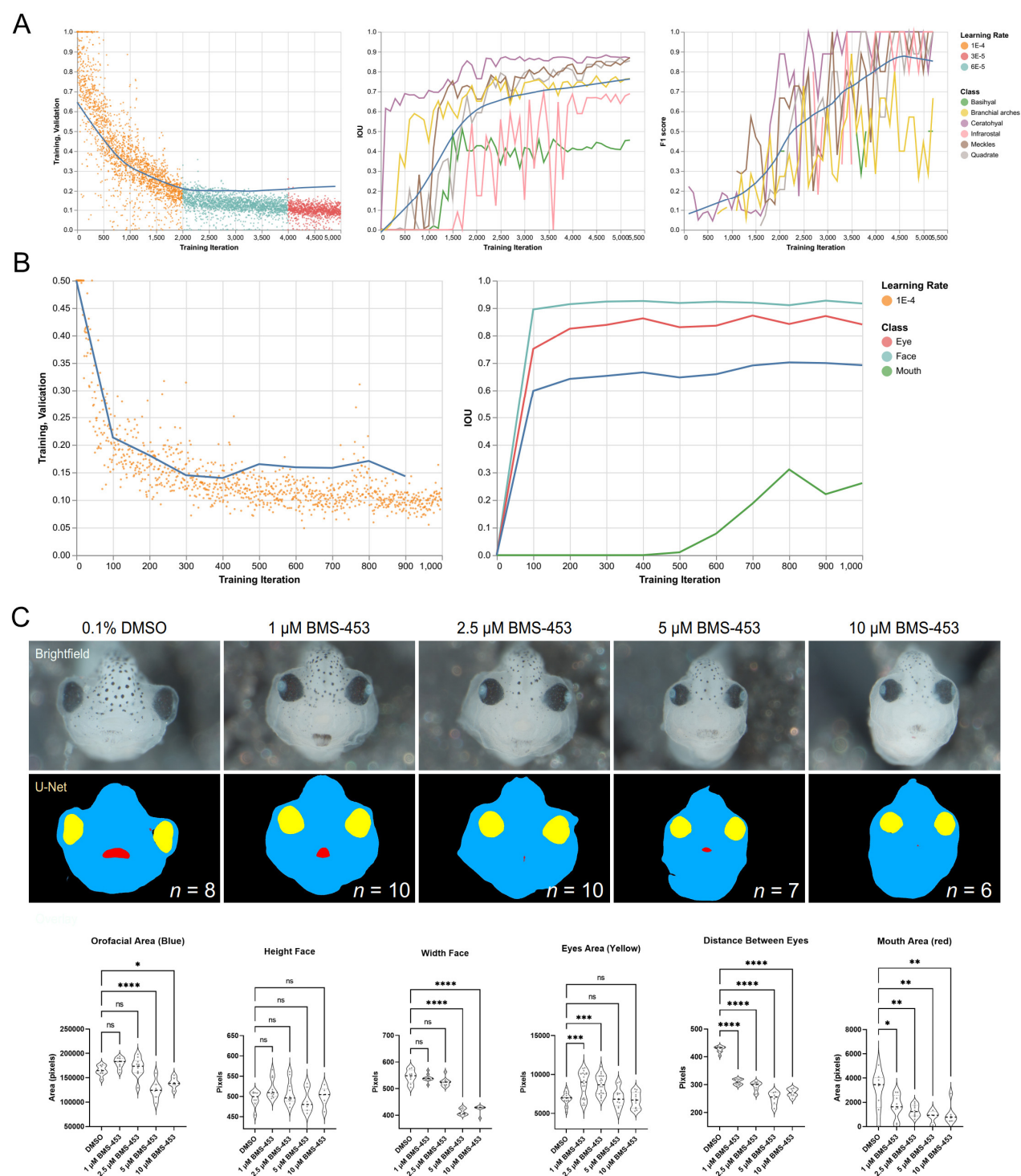
Fig. S14. U-Net deep learning for facial phenotyping. (A) AlcianNet training logs. Blue lines (left to right) are LOESS of validation loss, IOU across classes and F1 score across classes. **(B)** FaceNet training logs. Blue lines (left to right) are LOESS of validation loss and IOU across classes. **(C)** Embryos were subjected to four different concentrations of BMS-453 and a DMSO control and facial photographs were acquired. FaceNet was deployed on this unseen data and the masks were used to quantify orofacial area (blue), face height (blue - bounding box y), face width (blue - bounding box x), eyes (yellow), distance between eyes (bounding box edge yellow left eye to bounding box edge yellow right eye) and mouth area (red).
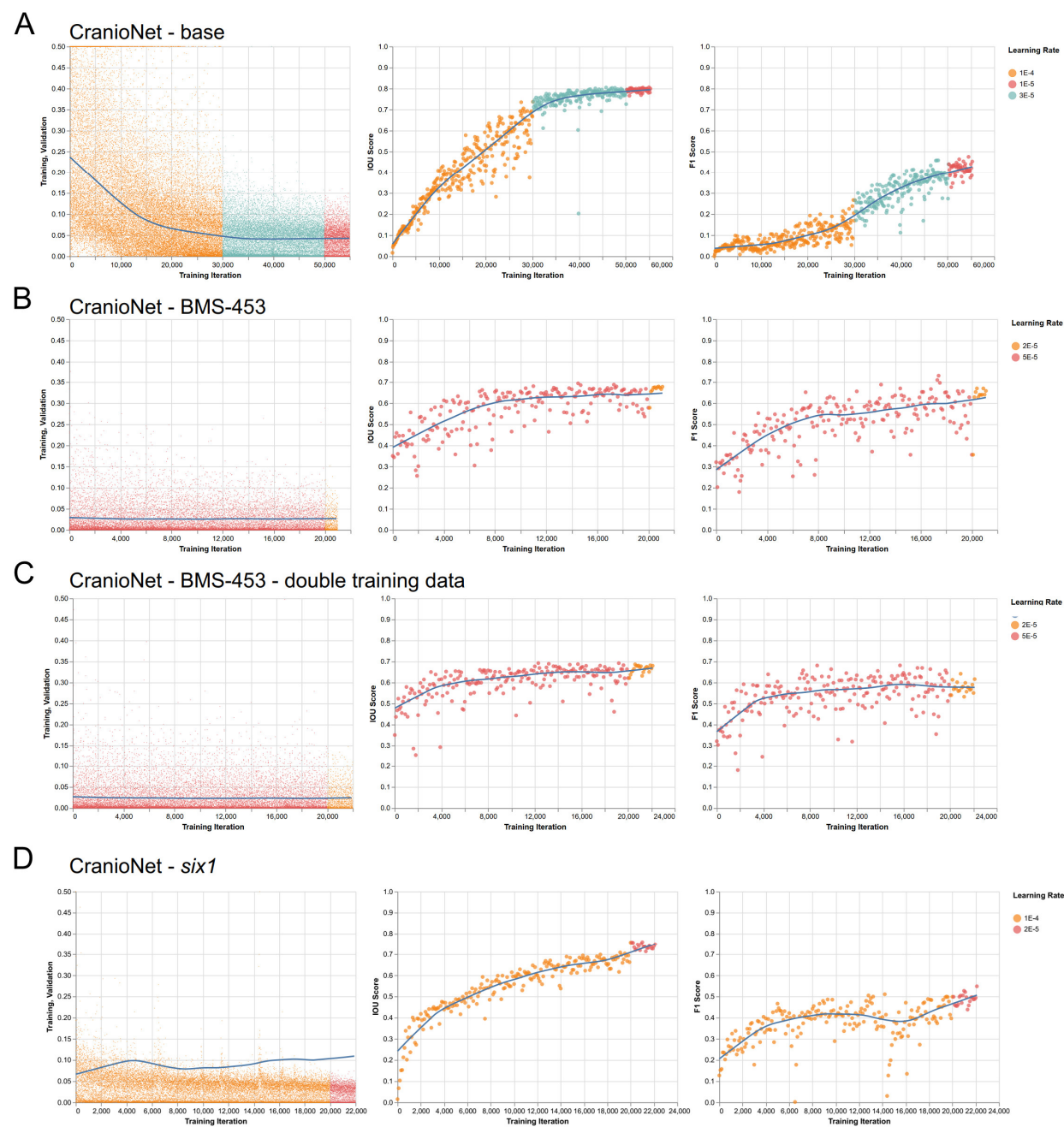
Fig. S15. CranioNet. (A) CranioNet training logs. Blue lines (left to right) are LOESS of validation loss, IOU and F1 score. **(B-C)** Transfer learning finetuning adapting a pre-trained CranioNet towards BMS-453 treated embryos. Blue lines (left to right) are LOESS of validation loss, IOU and F1 score. In panel C double the training data was used as in panel B, using the same validation dataset. **(D)** Transfer learning finetuning adapting a pre-trained CranioNet towards *six1* embryos. Blue lines (left to right) are LOESS of validation loss, IOU and F1 score.
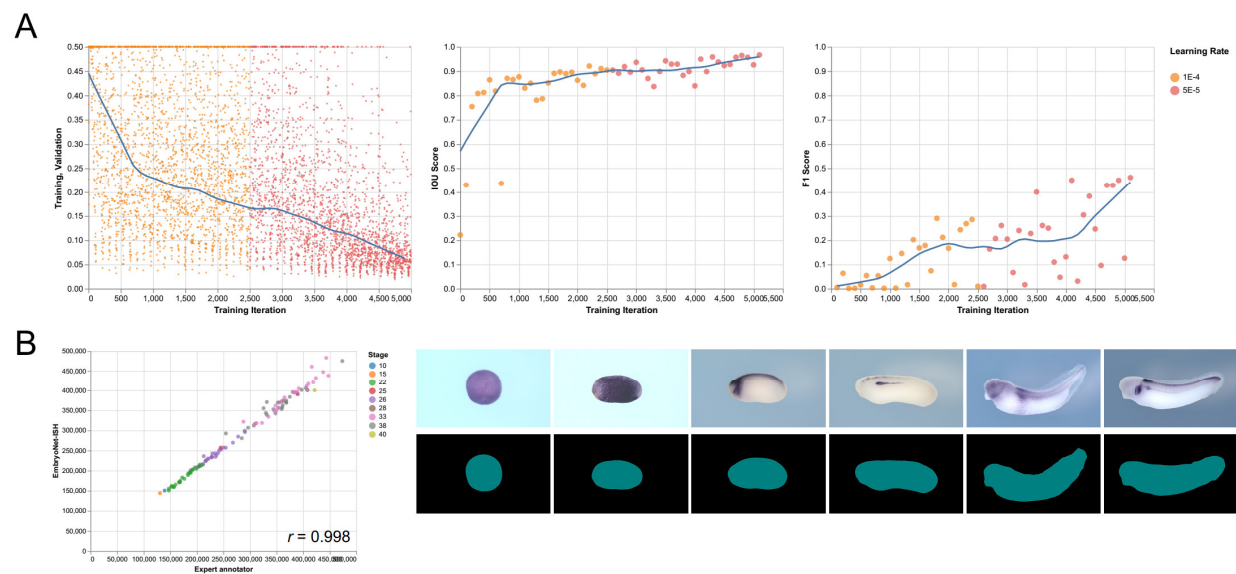
Fig. S16. EmbryoNet-ISH. (A) EmbryoNet-ISH training logs. Blue lines (left to right) are LOESS of validation loss, IOU and F1 score. **(B)** Cross-correlation of EmbryoNet-ISH to a human expert using unseen test images from different stages of *X. tropicalis* development.
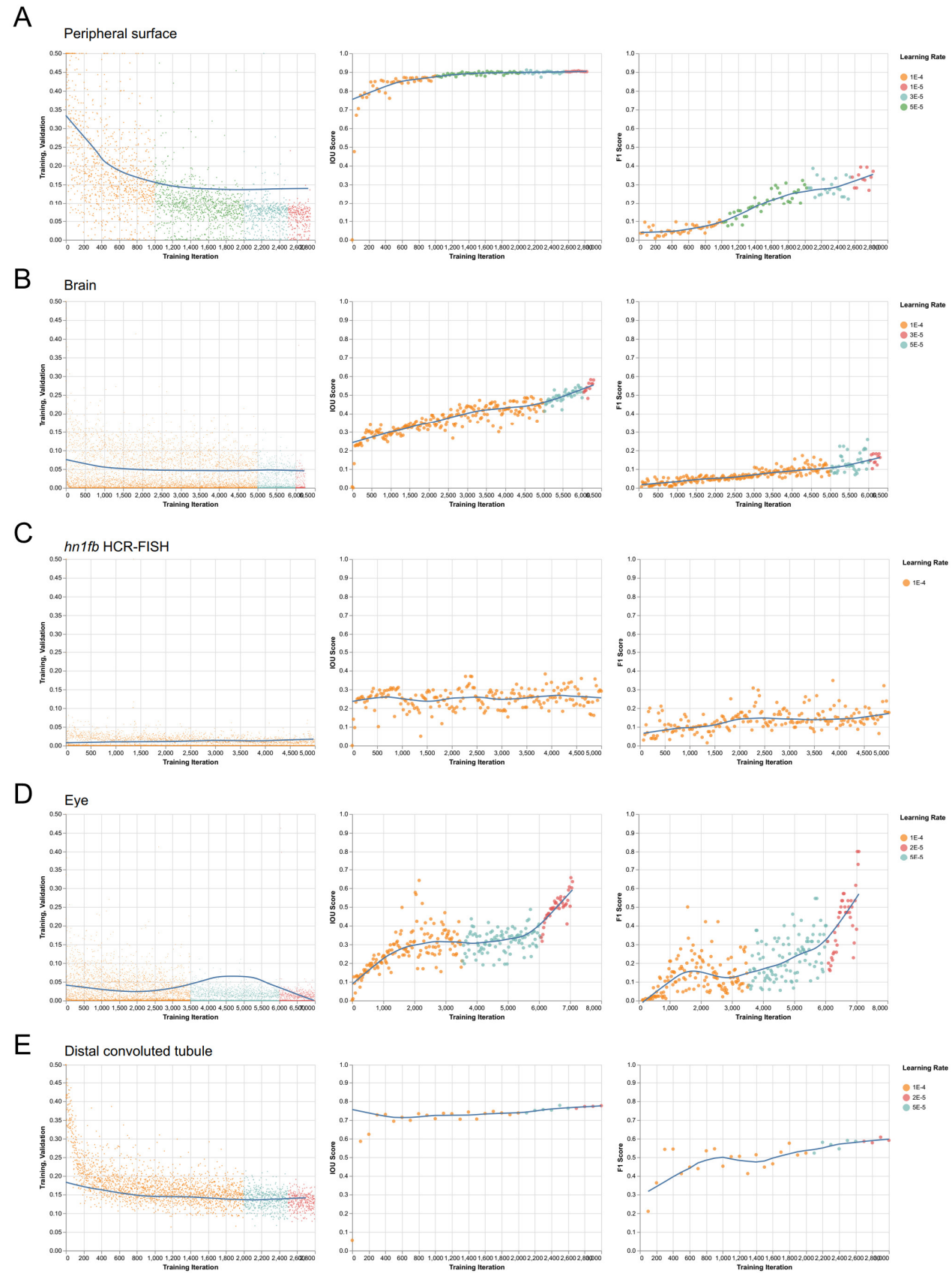
Fig. S17. Part1, U-Net training logs for models used in *X. tropicalis* reconstruction (Fig. 5D-E) and mouse whole kidney imaging (Fig. 5F). (A-E) VoluNet training logs. Blue lines (left to right) are LOESS of validation loss, IOU and F1 score.
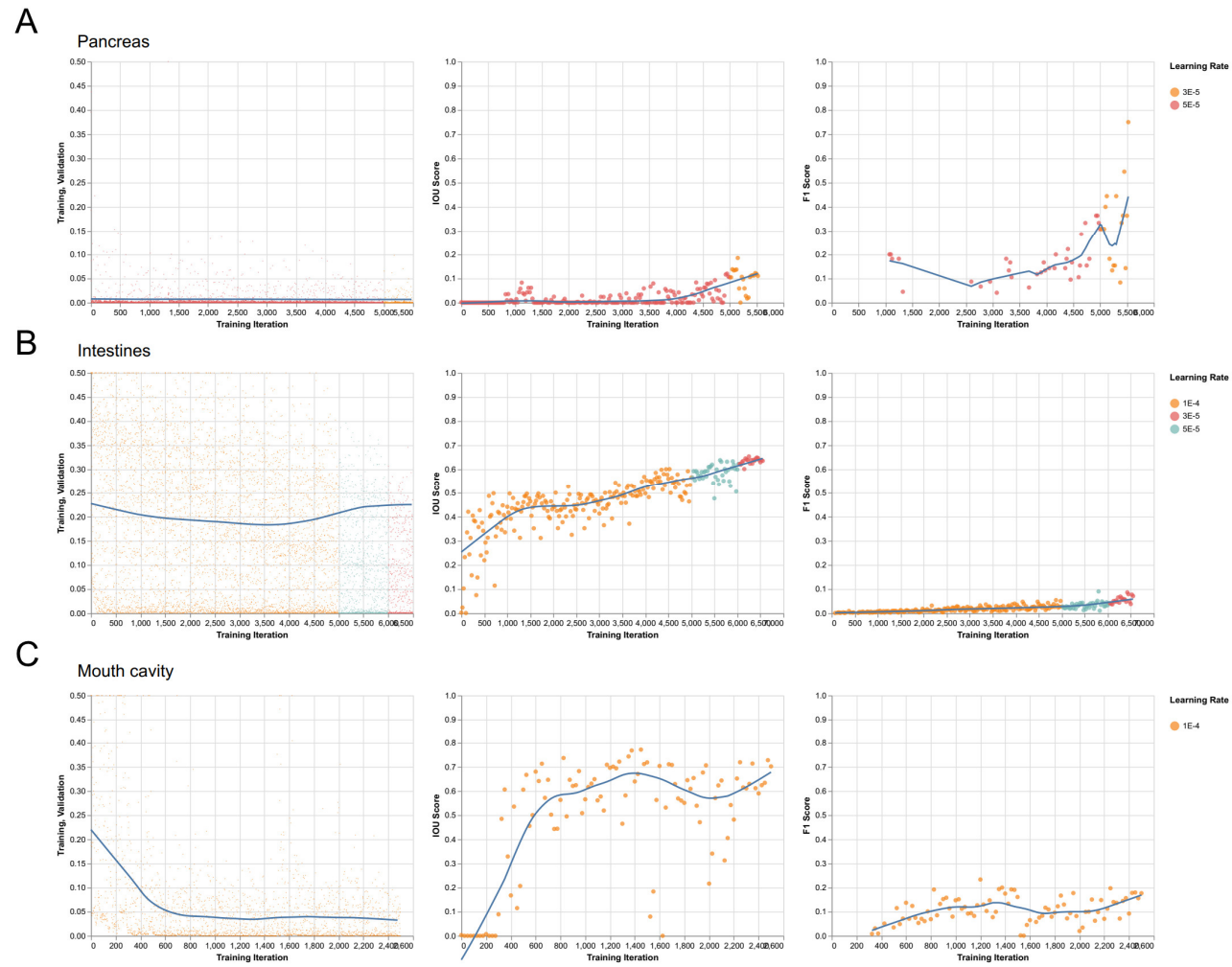
Fig. S18. Part2, U-Net training logs for models used in *X. tropicalis* reconstruction (Fig. 5D-E. (A-E) VoluNet training logs. Blue lines (left to right) are LOESS of validation loss, IOU and F1 score.
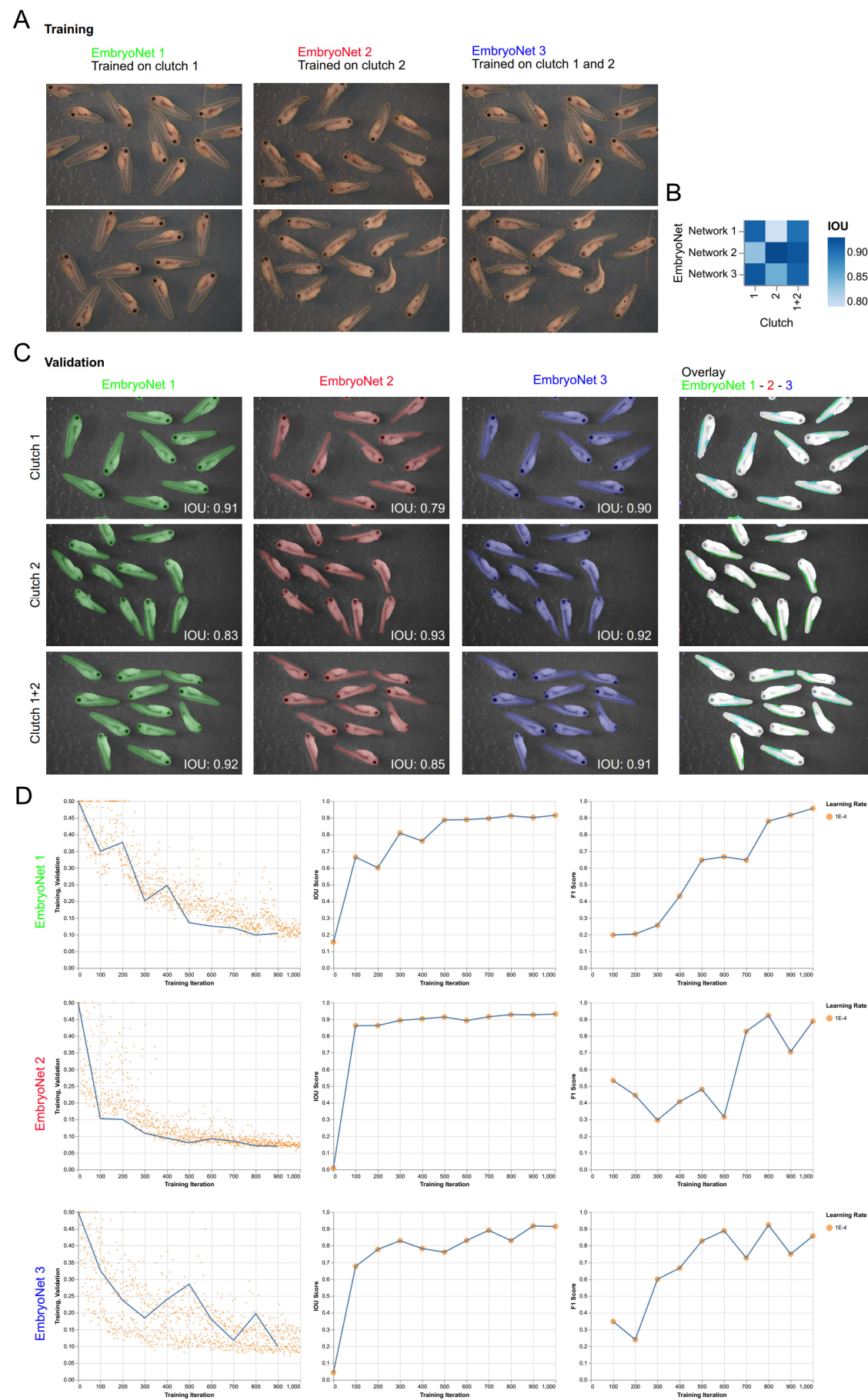
Fig. S19. (A) EmbryoNets were trained on two images shown. EmbryoNet 1 – trained on two images containing embryos from clutch 1, EmbryoNet 2 – trained on two images containing embryos from clutch 1, EmbryoNet 3 – trained one 1 image containing embryos from clutch 1 and one image containing embryos from clutch 2 **(B-C)** All three EmbryoNets were validated on an unseen image containing embryos from either clutch 1, embryos from clutch 2 and embryos from clutch 1 and clutch 2 intermixed 1:1. Shown is the correlation matrix (B) and the results of each EmbryoNet on validation data (C). **(D)** EmbryoNet training logs. Blue lines (left to right) are LOESS of validation loss, IOU and F1 score.

**Table S1. Primer sequences used for PCR amplification, oligo sequences used for gRNA synthesis and concentrations of injected CRISPR/Cas9 ribonucleoprotein complexes. (A)** Oligos employed for generation of template DNA for in vitro gRNA transcription. **(B)** Concentrations of sgRNAs and Cas9 microinjected in *Xenopus* embryos. **(C)** Genotyping primers for CRISPR/Cas9 target sites.

Table S1: Primer sequences used for PCR amplification, oligo sequences used for gRNA synthesis and concentrations of injected CRISPR/Cas9 ribonucleoprotein complexes

(A)

	Oligos employed for generation of template DNA for *in vitro gRNA transcription*	gRNA genomic target site
Xt_pkd1_gRNA1	5`-GAATtaatacgactcactataGGGCCTCTGACCCTCCAAGGgttttagagctagaaATAG-3`	GAGCCTCTGACCCTCCAAGGAGG
Xt_pkd1_gRNA2	5`-GAATtaatacgactcactataGGGTATAACTTCTCGACCAGgttttagagctagaaATAG-3`	GAGTATAACTTCTCGACCAGCGG
Xt_pkd1_gRNA3	5`-GAATtaatacgactcactataGGAAGGCTGTTCCTTGACAGgttttagagctagaaATAG-3`	GCAAGGCTGTTCCTTGACAGAGG
Xl_pkd2_gRNA1	5`-GAATtaatacgactcactataGGGGGGAGCACCGGCTTGGGgttttagagctagaaATAG-3`	GGGGGGAGCACCGGCTTGGG
Xl_pkd2_gRNA2	5`-GAATtaatacgactcactataGGGGATCTGGAGATGGACCGgttttagagctagaaATAG-3`	GAGGATCTGGAGATGGACCG
Xl_tyrS	5`-GAA TTA ATA CGA CTC ACT ATA GGC CCG TAG CAG AGC TGG TGG TTT TAG AGC TAG AAA TAG-3`	10.1186/s13578-015-0006-1
Xl_tyrL	5`-GAA TTA ATA CGA CTC ACT ATA GGG TCG ATG ATA GAG AGG ACG TTT TAG AGC TAG AAA TAG-3`	10.1186/s13578-015-0006-1

(B)

Concentrations of sgRNAs and Cas9 microinjected in Xenopus tropicalis embryos.

Setup	Delivery methodology	gRNA 1 (pg)	gRNA 2 (pg)	Cas9 protein (pg)
Xt pkd1 gRNA 1	2-cell embryo - bilateral - 1nL	200	x	900
Xt pkd1 gRNA 2	2-cell embryo - bilateral - 1nL	200	x	900
Xt pkd1 gRNA 3	2-cell embryo - bilateral - 1nL	200	x	900
Xt pkd1 gRNA 1	8-cell embryo - unilateral - ventrolateral vegetal - 2nL	400	x	1800
Xt pkd1 gRNA 2	8-cell embryo - unilateral - ventrolateral vegetal - 2nL	400	x	1800
Xt pkd1 gRNA 3	8-cell embryo - unilateral - ventrolateral vegetal - 2nL	400	x	1800
Xt tyr gRNA	8-cell embryo - unilateral - animal dorsal - 2nL	400	x	1800
Xl pkd2 gRNA 1	8-cell embryo - unilateral - ventrolateral vegetal - 5nL	1000	x	4500
Xl pkd2 gRNA 2	8-cell embryo - unilateral - ventrolateral vegetal - 5nL	1000	x	4500
Xl tyrS gRNA + *tyrL* gRNA	8-cell embryo - unilateral - ventrolateral vegetal - 5nL	500	500	4500

(C)

Genotyping primers for CRISPR/Cas9 target sites.

Xt_pkd1_gRNA1 - Fw	5`-TGGAGGCTACTTTGGTGGAC-3`
Xt_pkd1_gRNA1 - Rv	5`-CAAACTGTGGGACTGGCTCC-3`
Xt_pkd1_gRNA1 - seq	GTGTAGTCAGTGATGAAACC-3`
Xt_pkd1_gRNA2 - Fw	5`-ACCTTGTACCTGTGACGTGC-3`
Xt_pkd1_gRNA2 - Rv	5`-TCTTCAGCATGGGAGATGGC-3`
Xt_pkd1_gRNA2 - seq	5`-GCTTGGAGCAATTTGTTCC-3`
Xt_pkd1_gRNA3 - Fw	5`-TTTATGCAATGTGCCCAGCC-3`
Xt_pkd1_gRNA3 - Rv	5`-GCACTGCCTCCTCAAGTCAT-3`
Xt_pkd1_gRNA3 - seq	5`-TGAAGCAGAGATTGACCTGC-3`

**Table S2: List of trained U-Net models with metrics**

	Image modality	IOU (averaged in case of multiclass)	F1 Segmentation (averaged in case of multiclass)	Generalizability expected	Training *n*	Validation *n*	Input dimensions (pixels)	Rescaling factor	output dimensions (pixels)
TubuleNet	Fluorescence stereomicroscopy	0.78	N.D.	yes	295	105	320x240	1	320x240
3D-NephroNet	MesoSPIM light-sheet microscopy	0.58	0.37	yes	150 (6 samples - 5% of the slices)	60 (3 samples, 4% of the slices)	2048x580	1.5	1355x386
3D-CystNet	Confocal laser scanning microscopy	0.68	N.D.	N.D.	12 (2 samples - 3% of the slices)	10	2048x2048	2.8	731x731
EmbryoNet (Model related to Fig. S4)	Bright-Field stereomicroscopy	0.87	0.88	yes	1	1	1920x1200	2.1	914x571
OrganNet (Model related to Fig. S4)	Bright-Field stereomicroscopy	0.68	N.D.	yes	11	4	Varies	1.5	Varies
2D-NephroNet (model 1) (high magnification)	Fluorescence stereomicroscopy	0.8	0.5	yes	105	18	1920x1200	2.1	914x571
2D-NephroNet (model 2) (high magnification)	Fluorescence stereomicroscopy	0.78	0.61	yes	15	18	1920x1200	2.1	914x571
2D-NephroNet (pkd1) (low magnification)	Fluorescence stereomicroscopy	0.88	0.85	yes	30	30	1920x1200	2.3	842x635
2D-CystNet	Fluorescence stereomicroscopy	0.93	N.D.	yes	30	12	149x135 -> 189x202	1	149 x 135 -> 189 x 202
2D-NephroNet (pkd2)	Fluorescence stereomicroscopy	0.86	0.38	yes	30	8	1920x1200	2.3	914x571
2D-CystNet (pkd2)	Fluorescence stereomicroscopy	0.87	N.D.	yes	10	4	Varies	2	Varies
3D-NephroNet (PKD1) (Fig. S7)	MesoSPIM light-sheet microscopy	0.82	0.42	yes	35	6	550x550	1	550x550
DiameterNet	MesoSPIM light-sheet microscopy	0.87	0.24	yes	6	3	550x550	1	550x550
TelenNet (beta-tubulin)	Fluorescence stereomicroscopy	0.9	0.89	yes	20	4	2048x2048	2.7	759x759
TelenNet (PCNA)	Fluorescence stereomicroscopy	0.8	0.74	yes	8	4	2048x2048	2.8	731x731
2D-BrainNet	Fluorescence stereomicroscopy	0.88	1	yes	10	2	2048x2048	2.7	759x759
ProliNet	Fluorescence stereomicroscopy	0.52	0.37	yes	13	8	166x210 -> 198x275	1	166x210 -> 198x275
3D-BrainNet	MesoSPIM light-sheet microscopy	0.87	0.14	N.D.	33 (1 sample - 10% of the slices)	6 (1 samples - 1.8% of the slices)	380x912	1	380x912
AlcianNet	Bright-Field stereomicroscopy	0.75	0.89	yes	7	2	1920x1200	2.3	837 x 545
3D-CranioNet (base)	MesoSPIM light-sheet microscopy	0.8	0.45	yes	147 (3 samples - 10% of the slices)	51 (1 sample - 10% of the slices)	2048x2048	2.8	731x731
3D-CranioNet (BMS-453)	MesoSPIM light-sheet microscopy	0.68	0.66	yes	100 (5 samples - 2.5% of the slices)	45 (5 samples - 1.2% of the slices)	2048x2048	2.8	731x731
3D-CranioNet (BMS-453) (double training data)	MesoSPIM light-sheet microscopy	0.68	0.62	yes	192 (10 samples - 2.5% of the slices)	45 (5 samples - 1.2% of the slices)	2048x2048	2.8	731x731
3D-CranioNet (six1)	MesoSPIM light-sheet microscopy	0.75	0.55	yes	78 (3 samples - 2.5% of the slices)	51 (3 samples - 1.2% of the slices)			
FaceNet	Bright-Field stereomicroscopy	0.64	N.D.	yes	10	4	1920x1200	2.1	914x571
EmbryoNet-ISH	Bright-Field stereomicroscopy	0.97	0.46	yes	107	9	1518x920	2.1	723x438
DCT-Net	MesoSPIM light-sheet microscopy	0.78	0.59	N.D.	8	3	860x860	1.2	717x717
VoluNet-Brain	MesoSPIM light-sheet microscopy	0.58	0.16	N.D.	10 (1 sample - 1.35% of the slices)	9 (1 sample - 1.22% of the slices)	2048x2048	2.8	731x731
VoluNet-hnf1b	MesoSPIM light-sheet microscopy	0.29	0.18	N.D.	10 (1 sample - 1.35% of the slices)	9 (1 sample - 1.22% of the slices)	2048x2048	2.8	731x731
VoluNet-Surface	MesoSPIM light-sheet microscopy	0.90	0.37	N.D.	10 (1 sample - 1.35% of the slices)	9 (1 sample - 1.22% of the slices)	2048x2048	2.8	731x731
VoluNet-Eye	MesoSPIM light-sheet microscopy	0.64	0.80	N.D.	11 (1 sample - 1.49% of the slices)	9 (1 sample - 1.22% of the slices)	2048x2048	2.8	731x731
VoluNet-Mouth	MesoSPIM light-sheet microscopy	0.70	0.18	N.D.	10 (1 sample - 1.35% of the slices)	9 (1 sample - 1.22% of the slices)	2048x2048	2.8	731x731
VoluNet-Pancreas	MesoSPIM light-sheet microscopy	0.11	0.75	N.D.	19 (1 sample - 2.57% of the slices)	18 (1 sample - 2.44% of the slices)	2048x2048	2.8	731x731
VoluNet-Intestines	MesoSPIM light-sheet microscopy	0.64	0.07	N.D.	10 (1 sample - 1.35% of the slices)	9 (1 sample - 1.22% of the slices)	2048x2048	2.8	731x731
EmbryoNet (model 1)	Bright-Field stereomicroscopy	0.91	0.96	yes	2	1	1920x1200	2.1	914x571
EmbryoNet (model 2)	Bright-Field stereomicroscopy	0.93	0.89	yes	2	1	1920x1200	2.1	914x571
EmbryoNet (model 3)	Bright-Field stereomicroscopy	0.91	0.86	yes	2	1	1920x1200	2.1	914x571
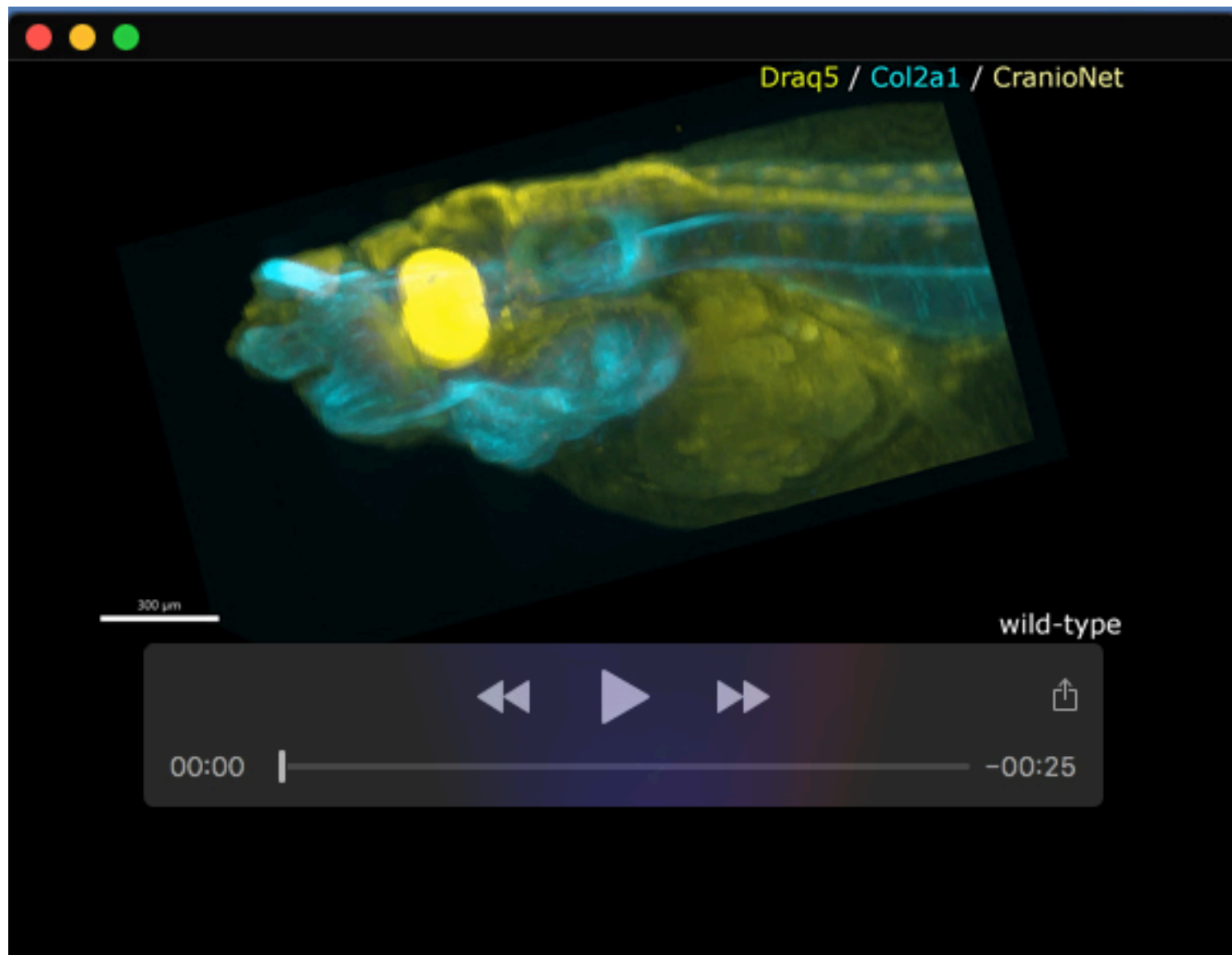
Movie 1. CranioNet 3D reconstruction of craniofacial cartilage from a Col2a1-stained wild-type *X. tropicalis* embryo counterstained with Draq5.
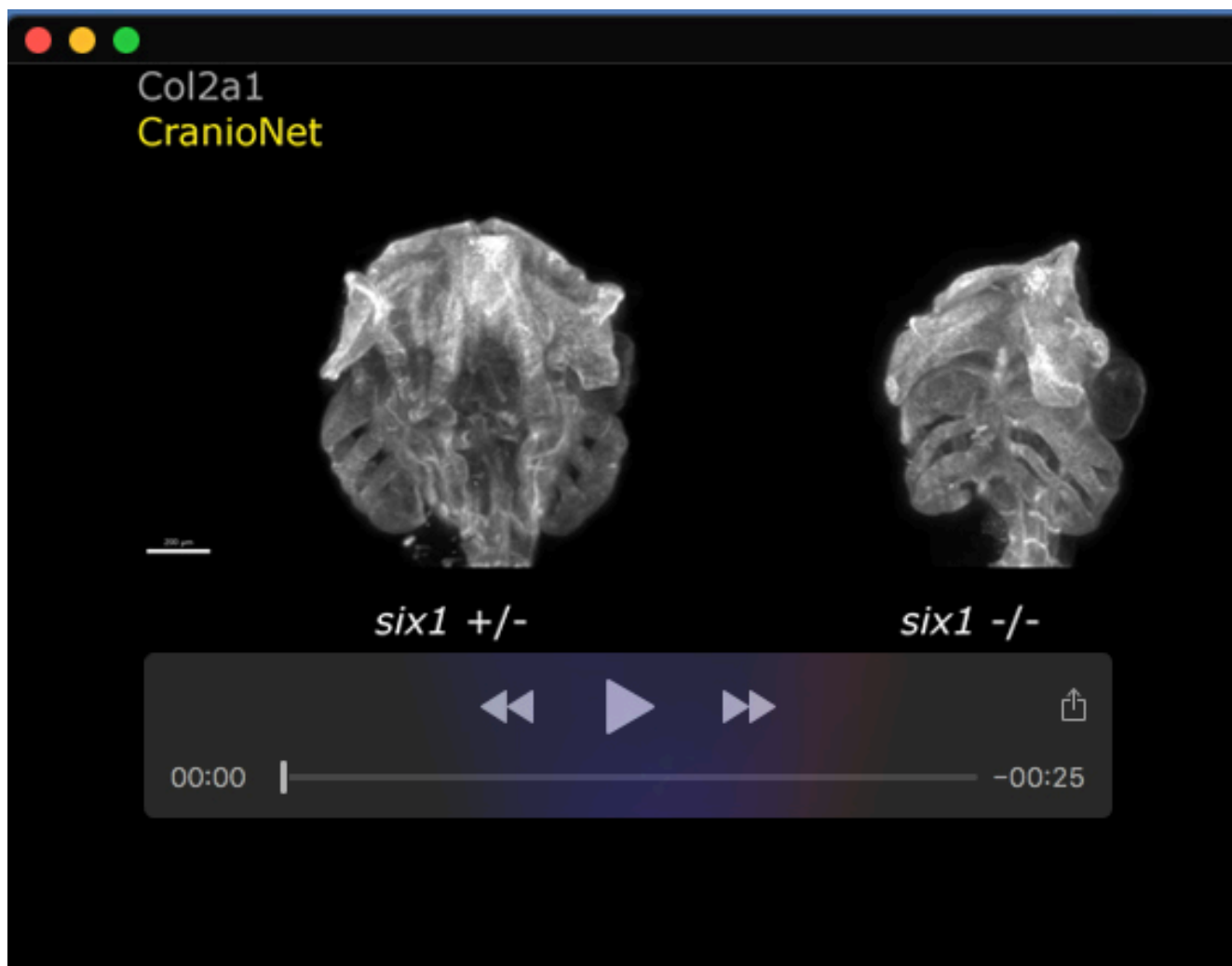
Movie 2. CranioNet 3D reconstruction of craniofacial cartilage from Col2a1-stained *six1⁺ᐟ⁻* and *six1⁻ᐟ⁻* *X. tropicalis* embryos shown side-by-side.
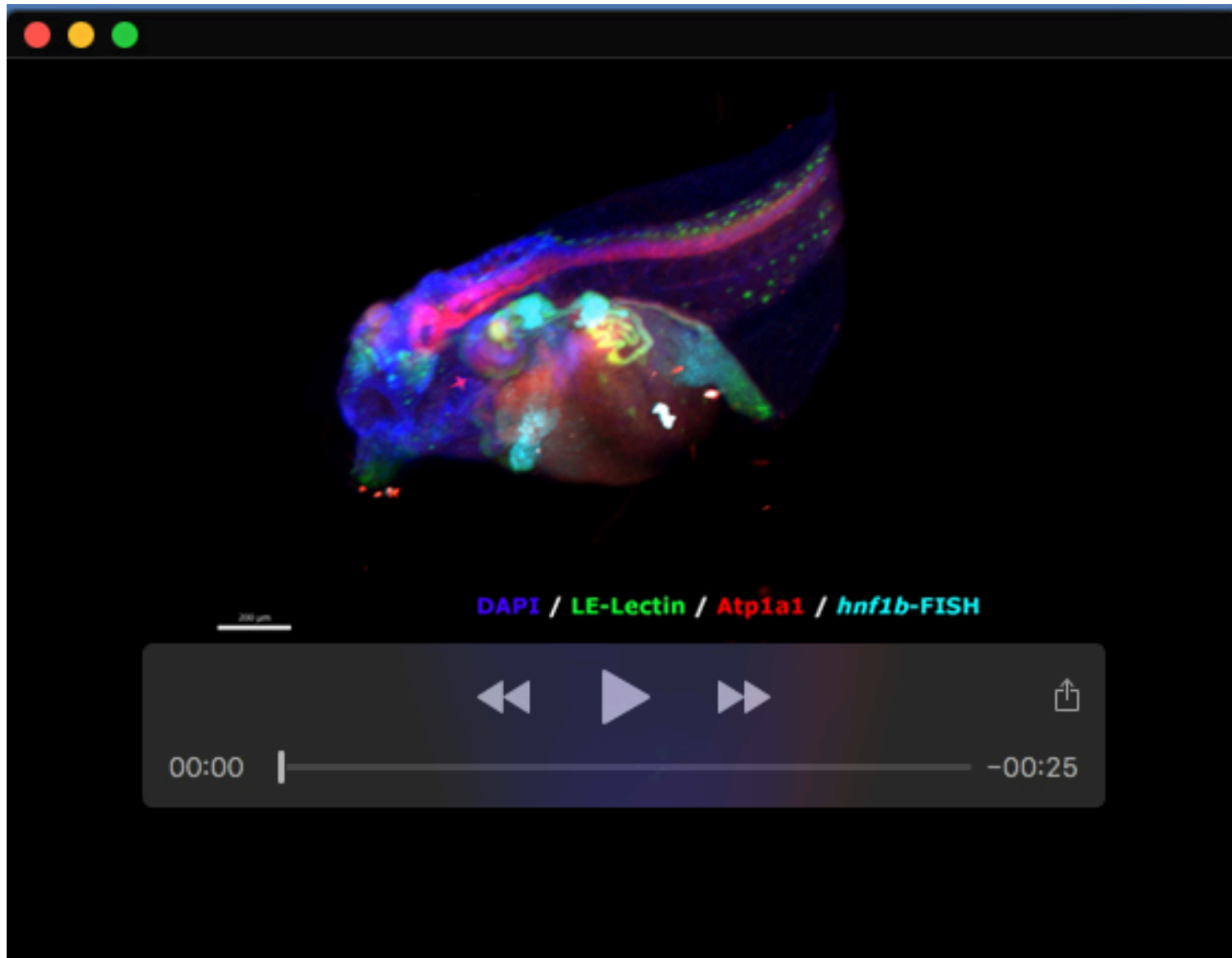
Movie 3. VoluNet 3D reconstructions of several morphological structures in a four-channel recording of an *X. tropicalis* embryo.